

¹ A Search in the Two-Photon Final State for
² Evidence of New Particle Production in pp
³ Collisions at $\sqrt{s} = 7$ TeV

⁴ Rachel P. Yohay
University of Virginia
`rpy3y@virginia.edu`

⁵ June 8, 2012

6 Contents

7	1	The Supersymmetric Extension to the Standard Model	3
8	1.1	Supermultiplet Representation	3
9	1.2	The Unbroken SUSY Lagrangian	4
10	1.3	Soft SUSY Breaking	10
11	1.4	Gauge-Mediated SUSY Breaking	12
12	1.5	Phenomenology of General Gauge Mediation	15
13	1.6	Experimental Status of SUSY	19
14	2	The Large Hadron Collider	23
15	2.1	Design Considerations and Performance Limitations	24
16	2.2	Beam Injection	27
17	2.3	Magnets and Cryogenics	29
18	2.4	Radiofrequency Cavities	32
19	3	The Compact Muon Solenoid Experiment	34
20	3.1	The Detectors and Their Operating Principles	38
21	3.1.1	Tracking System	38
22	3.1.2	Electromagnetic Calorimeter	47
23	3.1.3	Hadronic Calorimeter	52
24	3.1.4	Muon System	56
25	3.2	Triggering, Data Acquisition, and Data Transfer	61

26	3.2.1	Level 1 and High Level Trigger Systems	61
27	3.2.2	Data Acquisition System	65
28	3.2.3	Data Processing and Transfer to Computing Centers	68
29	4	Event Selection	71
30	4.1	Object Reconstruction	72
31	4.1.1	Photons	72
32	4.1.2	Electrons	83
33	4.1.3	Jets and Missing Transverse Energy	83
34	4.2	HLT	89
35	4.3	Event Quality	92
36	4.4	Photon Identification Efficiency	95
37	4.4.1	Tag and Probe Method	96
38	4.4.2	Photon Efficiency Scale Factor $\epsilon_e^{\text{data}}/\epsilon_e^{\text{MC}}$	99
39	5	Data Analysis	104
40	5.1	Modeling the QCD Background	108
41	5.1.1	Outline of the Procedure	108
42	5.1.2	Reweighting	109
43	5.1.3	Normalization	120
44	5.2	Modeling the Electroweak Background	120
45	5.3	Errors on the Background Prediction	126
46	5.4	Results	132
47	6	Interpretation of Results in Terms of GMSB Models	138
48	6.1	Simplified Models	138
49	6.2	Upper Limit Calculation and Model Exclusion	140
50	6.2.1	Signal Acceptance \times Efficiency	140
51	6.2.2	CL_s and the Profile Likelihood Test Statistic	144

52	6.3	Cross Section Upper Limits	151
53	6.4	Exclusion Contours	152
54	A	Monte Carlo Samples	157
55	A.0.1	List of Samples	157
56	A.0.2	Explanation of Naming Conventions	158

⁵⁷ Chapter 1

⁵⁸ The Supersymmetric Extension to ⁵⁹ the Standard Model

⁶⁰ The following introduction to SUSY focuses primarily on the aspects of the formalism that are relevant to phenomenology. In particular, most of the details of SUSY breaking (about which there is little theoretical consensus) are omitted, except where they are relevant to experiment. The notation is similar to that used in refs. [5] and [6], and much of the information presented is culled from those references.

⁶⁵ 1.1 Supermultiplet Representation

⁶⁶ The Standard Model is extended to include supersymmetry by the introduction of a supersymmetry transformation that takes fermionic states to bosonic states and vice versa. The resulting model is called the *minimal supersymmetric Standard Model* (MSSM). In analogy with the known symmetries of the Standard Model, the SUSY transformation has associated generators that obey defining commutation and anti-commutation relations, and a fundamental representation. All SM particles and their superpartners fall into one of two *supermultiplet* representations. Using the property that

$$n_F = n_B, \quad (1.1)$$

⁷⁴ where n_F is the number of fermionic degrees of freedom per supermultiplet and n_B is
⁷⁵ the number of bosonic degrees of freedom, the two types of supermultiplets are

- ⁷⁶ 1. *Chiral supermultiplets*: one Weyl fermion (two helicity states $\Rightarrow n_F = 2$) and
⁷⁷ one complex scalar field (with two real components $\Rightarrow n_B = 2$)
- ⁷⁸ 2. *Gauge supermultiplets*: One spin-1 vector boson (two helicity states $\Rightarrow n_B = 2$)
⁷⁹ and one Weyl fermion (two helicity states $\Rightarrow n_F = 2$)

⁸⁰ In the gauge supermultiplet, the vector boson is assumed massless (i.e. before
⁸¹ EWSB generates a mass for it). Since the superpartners to the SM particles have not
⁸² yet been discovered, they must be significantly heavier than their SM counterparts.
⁸³ Unbroken SUSY predicts that the SM particles and their superpartners must have
⁸⁴ exactly the same mass, so ultimately a mechanism for SUSY breaking must be intro-
⁸⁵ duced to generate masses for the superpartners (see Sec. 1.3). Tables 1.1 and 1.2 show
⁸⁶ the chiral and gauge supermultiplets of the MSSM, respectively. Note that the scalar
⁸⁷ partners to the SM fermions are denoted by placing an “s” in front of their names,
⁸⁸ while the chiral fermion partners to the SM gauge bosons are denoted by appending
⁸⁹ “ino” to their names.

⁹⁰ 1.2 The Unbroken SUSY Lagrangian

⁹¹ The first piece of the full unbroken SUSY Lagrangian density consists of the kinetic
⁹² and interacting terms related to the chiral supermultiplets. As explained in Sec. 1.1,
⁹³ a chiral supermultiplet consists of a Weyl fermion ψ (the ordinary fermion) and a
⁹⁴ complex scalar ϕ (the sfermion). For a collection of such chiral supermultiplets, the
⁹⁵ Lagrangian is

Table 1.1: Chiral supermultiplets of the supersymmetric Standard Model. Adapted from Table 1.1 of ref. [6].

Type of supermultiplet	Notation	Spin-0 component	Spin-1/2 component	Representation under $SU(3)_C \otimes SU(2)_L \otimes U(1)_Y$
Left-handed quark/squark doublet ($\times 3$ families)	Q	$(\tilde{u}_L \tilde{d}_L)$	$(u_L d_L)$	$(\mathbf{3}, \mathbf{2}, \frac{1}{6})$
Right-handed up-type quark/squark singlet ($\times 3$ families)	\bar{u}	\tilde{u}_R^*	u_R^\dagger	$(\bar{\mathbf{3}}, \mathbf{1}, -\frac{2}{3})$
Right-handed down-type quark/squark singlet ($\times 3$ families)	\bar{d}	\tilde{d}_R^*	d_R^\dagger	$(\bar{\mathbf{3}}, \mathbf{1}, \frac{1}{3})$
Left-handed lepton/slepton doublet ($\times 3$ families)	L	$(\tilde{\nu}_{eL} \tilde{e}_L)$	$(\bar{\nu}_{eL} e_L)$	$(\mathbf{1}, \mathbf{2}, -\frac{1}{2})$
Right-handed lepton/slepton singlet ($\times 3$ families)	\bar{e}	\tilde{e}_R^*	e_R^\dagger	$(\bar{\mathbf{1}}, \mathbf{1}, 1)$
Up-type Higgs/Higgsino doublet	H_u	$(H_u^+ H_u^0)$	$(\tilde{H}_u^+ \tilde{H}_u^0)$	$(\mathbf{1}, \mathbf{2}, \frac{1}{2})$
Down-type Higgs/Higgsino doublet	H_d	$(H_d^0 H_d^-)$	$(\tilde{H}_d^0 \tilde{H}_d^-)$	$(\mathbf{1}, \mathbf{2}, -\frac{1}{2})$

Table 1.2: Gauge supermultiplets of the supersymmetric Standard Model. Adapted from Table 1.2 of ref. [6].

Type of supermultiplet	Spin-1/2 component	Spin-1 component	Representation under $SU(3)_C \otimes SU(2)_L \otimes U(1)_Y$
Gluon/gluino	\tilde{g}	g	$(\mathbf{8}, \mathbf{1}, 0)$
W/wino	$\tilde{W}^\pm \tilde{W}^0$	$W^\pm W^0$	$(\mathbf{1}, \mathbf{3}, 0)$
B/bino	\tilde{B}^0	B^0	$(\mathbf{1}, \mathbf{1}, 0)$

$$\begin{aligned}\mathcal{L}_{\text{chiral}} = & -\partial^\mu \phi^{*i} \partial_\mu \phi_i - V_{\text{chiral}}(\phi, \phi^*) - i\psi^{\dagger i} \bar{\sigma}^\mu \partial_\mu \psi_i - \frac{1}{2} M^{ij} \psi_i \psi_j \\ & - \frac{1}{2} M_{ij}^* \psi^{\dagger i} \psi^{\dagger j} - \frac{1}{2} y^{ijk} \phi_i \psi_j \psi_k - \frac{1}{2} y_{ijk}^* \phi^{*i} \psi^{\dagger j} \psi^{\dagger k}\end{aligned}\quad (1.2)$$

where i runs over all supermultiplets in Table 1.1, $\bar{\sigma}^\mu$ are $-1 \times$ the Pauli matrices (except for $\sigma^0 = \bar{\sigma}^0$), M^{ij} is a mass matrix for the fermions, y^{ijk} are the Yukawa couplings between one scalar and two spinor fields, and $V_{\text{chiral}}(\phi, \phi^*)$ is the scalar potential

$$\begin{aligned}V_{\text{chiral}}(\phi, \phi^*) = & M_{ik}^* M^{kj} \phi^{*i} \phi_j + \frac{1}{2} M^{in} y_{jkn}^* \phi_i \phi^{*j} \phi^{*k} \\ & + \frac{1}{2} M_{in}^* y^{jkn} \phi^{*i} \phi_j \phi_k + \frac{1}{4} y^{ijn} y_{klm}^* \phi_i \phi_j \phi^{*k} \phi^{*l}.\end{aligned}\quad (1.3)$$

The Lagrangian can also be written as the kinetic terms plus derivatives of the *superpotential* W :

$$\begin{aligned}\mathcal{L}_{\text{chiral}} = & -\partial^\mu \phi^{*i} \partial_\mu \phi_i - i\psi^{\dagger i} \bar{\sigma}^\mu \partial_\mu \psi_i \\ & - \frac{1}{2} \left(\frac{\delta^2 W}{\delta \phi^i \delta \phi^j} \psi_i \psi_j + \frac{\delta^2 W^*}{\delta \phi_i \delta \phi_j} \psi^{\dagger i} \psi^{\dagger j} \right) - \frac{\delta W}{\delta \phi^i} \frac{\delta W^*}{\delta \phi_i}\end{aligned}\quad (1.4)$$

where

$$W = M^{ij} \phi_i \phi_j + \frac{1}{6} y^{ijk} \phi_i \phi_j \phi_k. \quad (1.5)$$

The second part of the Lagrangian involves the gauge supermultiplets. In terms of the spin-1 ordinary gauge boson A_μ^a and the spin-1/2 Weyl spinor gaugino λ^a of

¹⁰⁵ the gauge supermultiplet, where a runs over the number of generators for the SM
¹⁰⁶ subgroup (i.e. 1-8 for $SU(3)_C$, 1-3 for $SU(2)_L$, and 1 for $U(1)_Y$), this part of the
¹⁰⁷ Lagrangian is

$$\mathcal{L}_{\text{gauge}} = -\frac{1}{4}F_{\mu\nu}^a F^{\mu\nu a} - i\lambda^{\dagger a}\bar{\sigma}^\mu D_\mu \lambda^a + \frac{1}{2}D^a D^a \quad (1.6)$$

¹⁰⁸ where

$$F_{\mu\nu}^a = \partial_\mu A_\nu^a - \partial_\nu A_\mu^a + g f^{abc} A_\mu^b A_\nu^c \quad (1.7)$$

¹⁰⁹ (g is the coupling constant and f^{abc} are the structure constants for the particular SM
¹¹⁰ gauge group),

$$D_\mu \lambda^a = \partial_\mu \lambda^a + g f^{abc} A_\mu^b \lambda^c, \quad (1.8)$$

¹¹¹ and D^a is an auxiliary field that does not propagate (in the literature, it is used as a
¹¹² bookkeeping tool and can be removed via its algebraic equation of motion).

¹¹³ To build a fully supersymmetric and gauge-invariant Lagrangian, the ordinary
¹¹⁴ derivatives in $\mathcal{L}_{\text{chiral}}$ (Eq. 1.2) must be replaced by covariant derivatives

$$D_\mu \phi_i = \partial_\mu \phi_i - ig A_\mu^a (T^a \phi)_i \quad (1.9)$$

$$D_\mu \phi^{*i} = \partial_\mu \phi^{*i} + ig A_\mu^a (\phi^* T^a)^i \quad (1.10)$$

$$D_\mu \psi_i = \partial_\mu \psi_i - ig A_\mu^a (T^a \psi)_i. \quad (1.11)$$

¹¹⁵ This leads to the full Lagrangian

$$\begin{aligned}
\mathcal{L} &= \mathcal{L}_{\text{chiral}} + \mathcal{L}_{\text{gauge}} \\
&\quad - \sqrt{2}g(\phi^{*i}T^a\psi_i)\lambda^a - \sqrt{2}g\lambda^{\dagger a}(\psi^{\dagger i}T^a\phi_i) + g(\phi^{*i}T^a\phi_i)D^a \\
&= -\partial^\mu\phi^{*i}\partial_\mu\phi_i - i\psi^{\dagger i}\bar{\sigma}^\mu\partial_\mu\psi_i + ig\partial^\mu\phi^{*i}A_\mu^a(T^a\phi)_i - ig\partial_\mu\phi_iA^{\mu a}(\phi^*T^a)^i \\
&\quad - g^2A^{\mu a}(\phi^*T^a)^iA_\mu^a(T^a\phi)_i - g\psi^{\dagger i}\bar{\sigma}^\mu A_\mu^a(T^a\psi)_i - V_{\text{chiral}}(\phi, \phi^*) \\
&\quad - \frac{1}{2}M^{ij}\psi_i\psi_j - \frac{1}{2}M_{ij}^*\psi^{\dagger i}\psi^{\dagger j} - \frac{1}{2}y^{ijk}\phi_i\psi_j\psi_k - \frac{1}{2}y_{ijk}^*\phi^{*i}\psi^{\dagger j}\psi^{\dagger k} \\
&\quad - \frac{1}{4}F_{\mu\nu}^aF^{\mu\nu a} - i\lambda^{\dagger a}\bar{\sigma}^\mu\partial_\mu\lambda^a - ig\lambda^{\dagger a}\bar{\sigma}^\mu f^{abc}A_\mu^b\lambda^c + \frac{1}{2}D^aD^a \\
&\quad - \sqrt{2}g(\phi^{*i}T^a\psi_i)\lambda^a - \sqrt{2}g\lambda^{\dagger a}(\psi^{\dagger i}T^a\phi_i) + g(\phi^{*i}T^a\phi_i)D^a. \tag{1.12}
\end{aligned}$$

¹¹⁶ Writing out $F_{\mu\nu}^a$ and $V_{\text{chiral}}(\phi, \phi^*)$ explicitly combining the D^a terms using the equation

¹¹⁷ of motion $D^a = -g\phi^{*i}T^a\phi_i$, and rearranging some terms, the final unbroken SUSY

¹¹⁸ Lagrangian is

$$\begin{aligned}
\mathcal{L} = & -\partial^\mu \phi^{*i} \partial_\mu \phi_i - i\psi^{\dagger i} \bar{\sigma}^\mu \partial_\mu \psi_i \\
& - \frac{1}{4} (\partial_\mu A_\nu^a - \partial_\nu A_\mu^a) (\partial^\mu A^{\nu a} - \partial^\nu A^{\mu a}) - i\lambda^{\dagger a} \bar{\sigma}^\mu \partial_\mu \lambda^a \\
& - M_{ik}^* M^{kj} \phi^{*i} \phi_j - \frac{1}{2} M^{ij} \psi_i \psi_j - \frac{1}{2} M_{ij}^* \psi^{\dagger i} \psi^{\dagger j} \\
& + ig \partial^\mu \phi^{*i} A_\mu^a (T^a \phi)_i - ig \partial_\mu \phi_i A^{\mu a} (\phi^* T^a)^i - g \psi^{\dagger i} \bar{\sigma}^\mu A_\mu^a (T^a \psi)_i \\
& - ig \lambda^{\dagger a} \bar{\sigma}^\mu f^{abc} A_\mu^b \lambda^c \\
& - \frac{1}{4} g f^{abc} [(\partial_\mu A_\nu^a - \partial_\nu A_\mu^a) A^{\mu b} A^{\nu c} + A_\mu^b A_\nu^c (\partial^\mu A^{\nu a} - \partial^\nu A^{\mu a})] \\
& - \frac{1}{2} M_{in}^* y^{jkn} \phi^{*i} \phi_j \phi_k - \frac{1}{2} M^{in} y_{jkn}^* \phi_i \phi^{*j} \phi^{*k} \\
& - \frac{1}{2} y^{ijk} \phi_i \psi_j \psi_k - \frac{1}{2} y_{ijk}^* \phi^{*i} \psi^{\dagger j} \psi^{\dagger k} \\
& - \sqrt{2} g (\phi^{*i} T^a \psi_i) \lambda^a - \sqrt{2} g \lambda^{\dagger a} (\psi^{\dagger i} T^a \phi_i) \\
& - g^2 A^{\mu a} (\phi^* T^a)^i A_\mu^a (T^a \phi)_i - \frac{1}{4} g^2 f^{abc} A_\mu^b A_\nu^c f^{abc} A^{\mu b} A^{\nu c} \\
& - \frac{1}{4} y^{ijn} y_{kln}^* \phi_i \phi_j \phi^{*k} \phi^{*l} - \frac{1}{2} g^2 (\phi^{*i} T^a \phi_i)^2.
\end{aligned} \tag{1.13}$$

¹¹⁹ The above Lagrangian applies to chiral supermultiplets interacting with one kind
¹²⁰ of gauge supermultiplet (i.e. one SM gauge group). In the general case, there are
¹²¹ additional terms corresponding to interactions with all three SM gauge groups.

¹²² The following list gives a description of the terms in Eq. 1.13:

- ¹²³ • First two lines: kinetic terms for the four types of fields ϕ_i , ψ_i , A_μ^a , and λ^a
- ¹²⁴ • Third line: mass terms for the ϕ_i and ψ_i (see Figs. 1.1(a) and 1.1(b))
- ¹²⁵ • Fourth and fifth lines: cubic couplings in which ϕ_i , ψ_i , or λ^a radiates an A_μ^a (see
¹²⁶ Figs. 1.1(c), 1.1(d), and 1.1(e))
- ¹²⁷ • Sixth line: triple gauge boson couplings (see Fig. 1.1(f))
- ¹²⁸ • Seventh line: triple sfermion couplings (see Fig. 1.1(g))

- ¹²⁹ • Eighth line: cubic couplings in which ψ_i radiates a ϕ_i (see Fig. 1.1(h))
- ¹³⁰ • Ninth line: ϕ_i - ψ_i - λ^a vertices (see Fig. 1.1(i))
- ¹³¹ • 10th line: A_μ^a - A_μ^a - ϕ_i - ϕ_i and quadruple gauge boson couplings (see Figs. 1.1(j)
¹³² and 1.1(k))
- ¹³³ • 11th line: ϕ_i^4 vertices (see Figs. 1.1(l) and 1.1(m))

¹³⁴ 1.3 Soft SUSY Breaking

¹³⁵ Since quadratic divergences in sfermion masses vanish to all orders in perturbation
¹³⁶ theory in plain unbroken SUSY [6] due to the presence of gauge and Yukawa interac-
¹³⁷ tions with the necessary relationships between coupling constants, it is desirable that
¹³⁸ the terms that break SUSY not disturb this property. In addition, SUSY should be
¹³⁹ broken spontaneously, as electroweak symmetry is broken in the Standard Model, so
¹⁴⁰ that it is only made manifest at high energies. To satisfy these constraints, SUSY-
¹⁴¹ breaking terms are simply added to the unbroken SUSY Lagrangian in Eq. 1.13 such
¹⁴² that $\mathcal{L}_{\text{total}} = \mathcal{L}_{\text{unbroken}} + \mathcal{L}_{\text{breaking}}$. The coefficients of terms in $\mathcal{L}_{\text{breaking}}$ must have
¹⁴³ positive mass dimension in order not to contribute quadratically divergent loop cor-
¹⁴⁴ rections to the scalar masses (like the Higgs mass).¹ This form of SUSY breaking is
¹⁴⁵ called *soft*, and all coefficients of soft SUSY breaking terms are expected to be of
¹⁴⁶ order m_{soft} or m_{soft}^2 .

¹This point can be argued via dimensional analysis. Radiative corrections take the form Δm_S^2 , where m_S is the mass of the scalar particle in question. The dimensions of Δm_S^2 are mass². Δm_S^2 is proportional to some coupling constant or mass coefficient k multiplied by a function of Λ_{UV} , the high energy cutoff scale. The function of Λ_{UV} is determined by a loop integral, and thus typically takes the form Λ_{UV}^2 (quadratically divergent) or $\ln \frac{\Lambda_{\text{UV}}}{m_{\text{low}}}$ (logarithmically divergent, where m_{low} is some other lower-mass scale in the problem). Now, if k already contributes at least one power of mass to Δm_S^2 , then the high-energy behavior—the function of Λ_{UV} —can only contribute at most one power of the dimensionful parameter Λ_{UV} . However, there are typically no loop integrals that diverge linearly in Λ_{UV} , so by forcing k to have positive mass dimension, the form of the radiative corrections contributed by SUSY-breaking terms is limited to $\Delta m_S^2 \sim m_{\text{low}}^2 \ln \frac{\Lambda_{\text{UV}}}{m_{\text{low}}}$. In effect, the possibility of dangerous corrections proportional to Λ_{UV}^2 is excluded by dimensional analysis if the requirement that k contribute at least one power of mass is enforced.

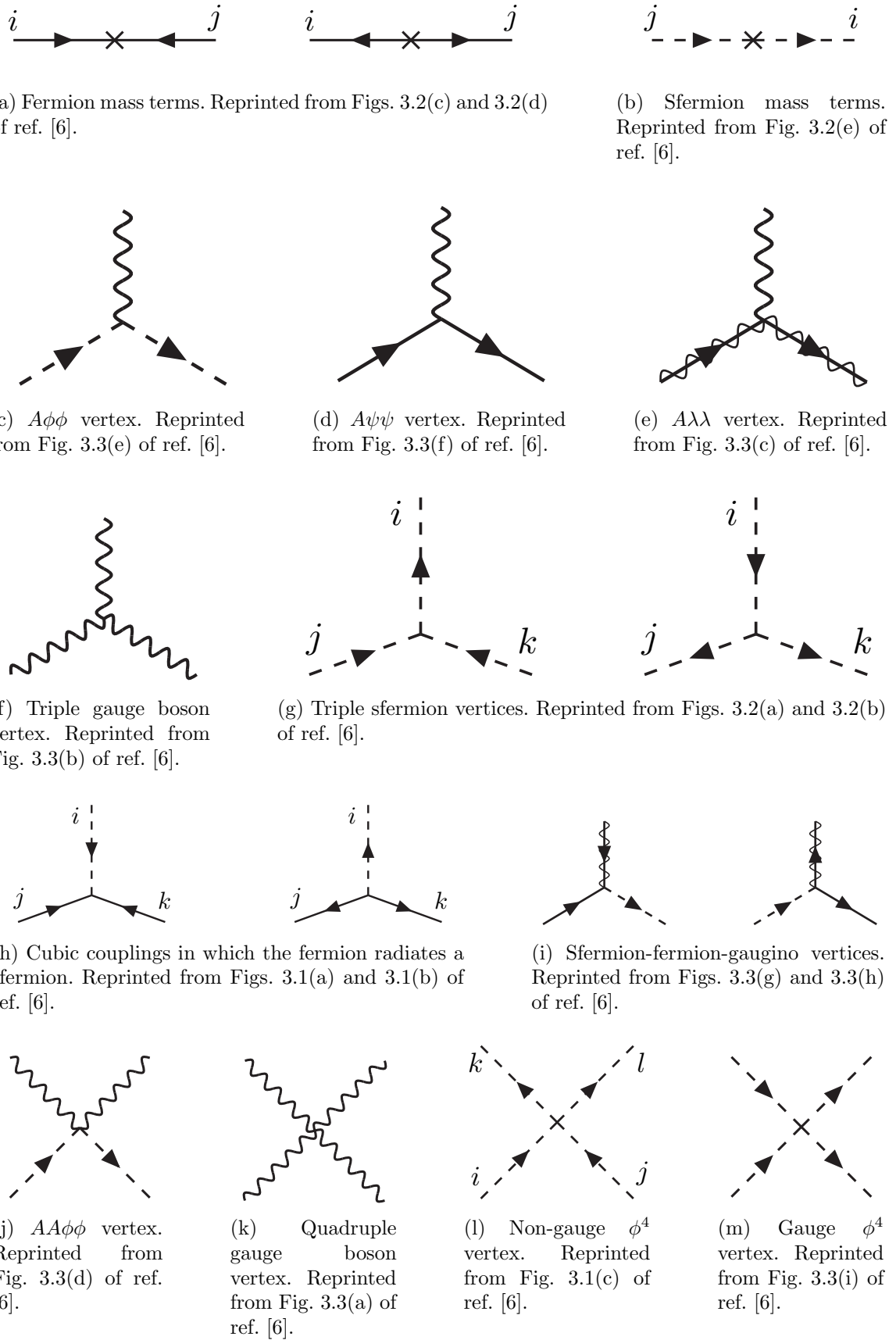


Figure 1.1: Interactions in the unbroken SUSY Lagrangian.

¹⁴⁷ Soft SUSY breaking terms give masses to the sfermions and gauginos and introduce
¹⁴⁸ a cubic sfermion vertex. The soft terms are given by

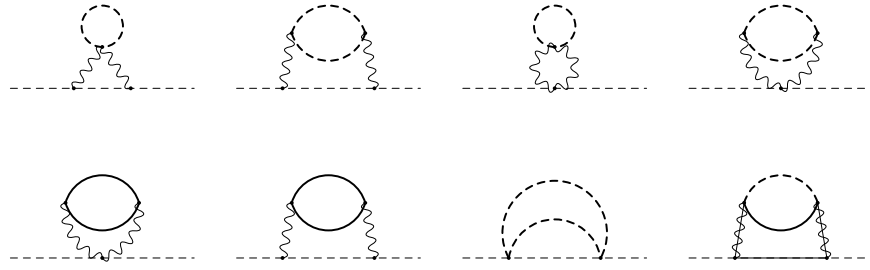
$$\begin{aligned}
 \mathcal{L}_{\text{soft}} = & -\frac{1}{2}(M_3\tilde{g}^a\tilde{g}^a + M_2\tilde{W}^a\tilde{W}^a + M_1\tilde{B}\tilde{B} + \text{h.c.}) \\
 & - (a_u^{ij}\tilde{u}_{Ri}^*\tilde{Q}_j H_u - a_d^{ij}\tilde{d}_{Ri}^*\tilde{Q}_j H_d - a_e^{ij}\tilde{e}_{Ri}^*\tilde{L}_j H_d + \text{h.c.}) \\
 & - m_{\tilde{Q}_{ij}}^2 \tilde{Q}_i^\dagger \tilde{Q}_j - m_{\tilde{L}_{ij}}^2 \tilde{L}_i^\dagger \tilde{L}_j \\
 & - m_{\tilde{u}_{ij}}^2 \tilde{u}_{Ri} \tilde{u}_{Rj}^* - m_{\tilde{d}_{ij}}^2 \tilde{d}_{Ri} \tilde{d}_{Rj}^* - m_{\tilde{e}_{ij}}^2 \tilde{e}_{Ri} \tilde{e}_{Rj}^* \\
 & - m_{H_u}^2 H_u^* H_u - m_{H_d}^2 H_d^* H_d - (b H_u H_d + \text{h.c.})
 \end{aligned} \tag{1.14}$$

¹⁴⁹ where a runs from 1-8 for \tilde{g}^a and from 1-3 for \tilde{W}^a , and i, j run over the three families.
¹⁵⁰ The color indices are not shown. The first line of Eq. 1.14 contains the gaugino mass
¹⁵¹ terms. The second line contains cubic scalar couplings that contribute to mixing
¹⁵² between the left- and right-handed third generation sfermions (it is assumed in the
¹⁵³ supersymmetric Standard Model that the a_u^{ij} , a_d^{ij} , and a_e^{ij} are negligible unless $i =$
¹⁵⁴ $j = 3$). The third and fourth lines of Eq. 1.14 contain squark and slepton mass terms,
¹⁵⁵ and finally the last line contains the Higgs mass terms.

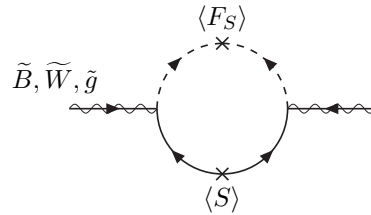
¹⁵⁶ Many viable models of achieving soft SUSY breaking have been studied over the
¹⁵⁷ last 30 years. For an overview, see Sec. 6 of ref. [6]. However, this thesis will only cover
¹⁵⁸ *gauge-mediated SUSY breaking* (GMSB), because the two-photon search performed
¹⁵⁹ is far more sensitive to this model than to other models of SUSY breaking.

¹⁶⁰ 1.4 Gauge-Mediated SUSY Breaking

¹⁶¹ In gauge-mediated models [7], “hidden” fields spontaneously break the supersymme-
¹⁶² try of very heavy chiral *messenger* supermultiplets. There are a number of compet-
¹⁶³ ing models (see ref. [7]) that explain the precise mechanism of spontaneous SUSY



(a) Sfermion mass terms. Heavy dashed lines denote messenger sfermions; solid lines denote messenger fermions. Reprinted from Fig. 6.4 of ref. [6].



(b) Gaugino mass term. The $\langle S \rangle$ part of the loop is a messenger fermion contribution; the $\langle F_S \rangle$ part is a messenger sfermion contribution. Reprinted from Fig. 6.3 of ref. [6].

Figure 1.2: Contributions to sfermion and gaugino masses from loop interactions with messenger particles in the GMSB framework.

164 breaking, but fortunately the details of those models mostly decouple from the phe-
 165 nomenology of GMSB. The messengers then communicate the SUSY breaking to the
 166 sparticles via loop diagrams of gauge interaction strength (i.e. via vertices like those
 167 shown in Figs. 1.1(c), 1.1(d), 1.1(i), 1.1(j), and 1.1(m), which are proportional to
 168 the SM gauge couplings constants). Feynman diagrams corresponding to gaugino and
 169 sfermion mass terms are shown in Figure 1.2.

170 Historically, GMSB and gravity-mediated SUSY breaking, or mSUGRA [8], have
 171 been the two most thoroughly experimentally studied scenarios of SUSY breaking.
 172 One advantage of GMSB over mSUGRA is that it naturally suppresses flavor vio-
 173 lation, a generic prediction of supersymmetry. Flavor violation is introduced in the
 174 scalar³ couplings and sfermion mass terms of $\mathcal{L}_{\text{soft}}$ (second, third, and fourth lines of

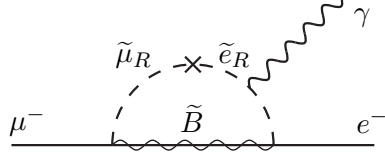


Figure 1.3: Possible contribution to $\mu \rightarrow e\gamma$ from $m_{\tilde{e}ij}$ soft term. Reprinted from Fig. 5.6(a) of ref. [6].

Eq. 1.14). Since a_u^{ij} , a_d^{ij} , a_e^{ij} , $m_{\tilde{Q}ij}$, $m_{\tilde{L}ij}$, $m_{\tilde{u}ij}$, $m_{\tilde{d}ij}$, and $m_{\tilde{e}ij}$ are matrices in family space, any nonzero off-diagonal elements will lead to mixing between sfermions of different families. This can lead, for example, to contributions to the diagram $\mu \rightarrow e\gamma$ (Figure 1.3) exceeding the experimental bounds. To avoid this disaster, *universality* conditions are assumed:

$$\mathbf{m}_{\tilde{\mathbf{Q}}}^2 = m_{\tilde{Q}}^2 \mathbf{1}, \mathbf{m}_{\tilde{\mathbf{L}}}^2 = m_{\tilde{L}}^2 \mathbf{1}, \mathbf{m}_{\tilde{\mathbf{u}}}^2 = m_{\tilde{u}}^2 \mathbf{1}, \mathbf{m}_{\tilde{\mathbf{d}}}^2 = m_{\tilde{d}}^2 \mathbf{1}, \mathbf{m}_{\tilde{\mathbf{e}}}^2 = m_{\tilde{e}}^2 \mathbf{1} \quad (1.15)$$

i.e. all sfermion mass matrices arising from the soft terms are assumed to be proportional to the unit matrix $\mathbf{1}$, such that there can be no flavor mixing from these terms and contributions to flavor-changing processes are drastically reduced.² In mSUGRA models, universality is assumed from the beginning, while in GMSB it is a natural consequence of the fact that the sparticle-messenger vertices are flavor-blind.

In minimal GMSB (mGMSB), there are four messenger supermultiplets q, \bar{q}, l, \bar{l} providing the messenger (s)quarks and (s)leptons. There is one breaking scale Λ . The gaugino masses computed from diagrams like Fig. 1.2(b) are given by

$$M_a = \frac{\alpha_a}{4\pi} \Lambda \quad (1.16)$$

²Universality also includes some assumptions about the form of a_{uij} , a_{dij} , and a_{eij} and the stipulation that the soft terms not introduce any CP-violating phases.

¹⁸⁸ where a runs from 1-3 and the α_a are the SM gauge coupling constants. The sfermion
¹⁸⁹ masses computed from diagrams like Fig. 1.2(a) are given by

$$m_{\phi_i}^2 = 2\Lambda^2 \sum_{a=1}^3 \left(\frac{\alpha_a}{4\pi}\right)^2 C_a(i) \quad (1.17)$$

¹⁹⁰ where $C_a(i)$ are group theory factors that are identical for all particles residing in
¹⁹¹ the same type of supermultiplet (e.g. for all left-handed (s)quarks or left-handed
¹⁹² (s)leptons). As explained in the previous paragraph, the gaugino and sfermion masses
¹⁹³ do not depend on fermion family.

¹⁹⁴ In recent years, much theoretical progress has been made in unifying models of
¹⁹⁵ gauge mediation and developing less restrictive models than mGMSB. *General gauge*
¹⁹⁶ *mediation* (GGM) [9] retains the essential features of mGMSB, such as flavor de-
¹⁹⁷ generacy and communication of SUSY breaking via messengers, but does not make
¹⁹⁸ assumptions about the specific messenger sector or SUSY breaking scale. Many dif-
¹⁹⁹ ferent collider final states can be interpreted in terms of GGM, and conversely, GGM
²⁰⁰ implies a wealth of signatures, only a small fraction of which have been searched for
²⁰¹ at colliders [10, 11, 12]. The following section discusses the aspects of GGM collider
²⁰² phenomenology relevant to this thesis.

²⁰³ 1.5 Phenomenology of General Gauge Mediation

²⁰⁴ The main distinguishing feature of all GMSB phenomenology is that the gravitino \tilde{G} is
²⁰⁵ very light (eV-keV). In general, the gravitino mass is proportional to $\langle F \rangle / M_P$, where
²⁰⁶ $\langle F \rangle$ is the vacuum expectation value (VEV) of a field F that spontaneously breaks
²⁰⁷ SUSY in the vacuum state and M_P is the Planck mass. In GGM models, $\langle F \rangle \sim 10^8$
²⁰⁸ GeV, leading to a very light gravitino. In contrast, mSUGRA predicts $\langle F \rangle \sim 10^{20}$
²⁰⁹ GeV. The fact that the gravitino is so much lighter than any other particles in the

²¹⁰ supersymmetric Standard Model, and that it interacts only gravitationally (and thus
²¹¹ extremely feebly), leads to two important phenomenological consequences:

- ²¹² 1. All sparticle decay chains end with the production of a gravitino.
- ²¹³ 2. The gravitino escapes 4π , hermetic collider detectors without interacting, leav-
²¹⁴ ing a signature of “missing” momentum transverse to the beam direction.

²¹⁵ Even if the gravitino were lighter than any other sparticle, but heavier than an
²¹⁶ ordinary SM particle, it still could not decay to the SM particle due to *R-parity*. R-
²¹⁷ parity is a conserved quantity of the supersymmetric Standard Model that enforces
²¹⁸ baryon and lepton number conservation, which would otherwise be generically allowed
²¹⁹ at levels in conflict with experiment (e.g. the non-observation of baryon- and lepton-
²²⁰ number-violating proton decay). All sparticles have R-parity -1, while all ordinary SM
²²¹ particles have R-parity +1, and R-parity conservation dictates that at any vertex, the
²²² product of the R-parities of each leg must be +1. This leads to two more important
²²³ consequences:

- ²²⁴ 1. Since conservation of energy only allows it to decay to ordinary SM particles,
²²⁵ but R-parity prevents a sparticle-particle-particle vertex, the *lightest supersym-
²²⁶ metric particle* (LSP) must be absolutely stable. All sparticle decays proceed
²²⁷ through the *next-to-lightest supersymmetric particle* (NLSP), which in turn de-
²²⁸ cays to the LSP. The fact that it is stable and only gravitationally interacting
²²⁹ makes the gravitino a candidate dark matter particle (see Sec. 1.6).
- ²³⁰ 2. In colliders, sparticles are produced in pairs (particle + particle \rightarrow sparticle +
²³¹ sparticle).

²³² In GMSB, then, the gravitino is the LSP. If the NLSP is a gaugino,³ then the
²³³ possible decays depend on mixing among the gauginos. Due to the effects of EWSB,

³In principle, the NLSP could be anything, but in most popular GGM models, it is either a gaugino or a stau. The stau NLSP search is not the subject of this thesis, so it will not be considered in this section.

²³⁴ the four neutral gauginos \tilde{H}_u^0 , \tilde{H}_d^0 , \tilde{B} , \tilde{W}^0 mix into four *neutralino* mass eigenstates
²³⁵ $\tilde{\chi}_1^0, \tilde{\chi}_2^0, \tilde{\chi}_3^0, \tilde{\chi}_4^0$, and the four charged gauginos $\tilde{H}_u^+, \tilde{H}_d^-, \tilde{W}^+, \tilde{W}^-$ mix into two *chargino*
²³⁶ mass eigenstates $\tilde{\chi}_1^\pm, \tilde{\chi}_2^\pm$ (two mass eigenstates each with two possible charges = four
²³⁷ particles). In the limit that EWSB effects are small, the neutralino and chargino
²³⁸ masses can be written as the gauge eigenstate masses plus a small perturbation:

$$m_{\tilde{\chi}_1^0} = M_1 - \frac{m_Z^2 \sin^2 \theta_W (M_1 + \mu \sin 2\beta)}{\mu^2 - M_1^2} + \dots \quad (1.18)$$

$$m_{\tilde{\chi}_2^0} = M_2 - \frac{m_W^2 (M_2 + \mu \sin 2\beta)}{\mu^2 - M_2^2} + \dots \quad (1.19)$$

$$m_{\tilde{\chi}_3^0} = |\mu| + \frac{m_Z^2 (\text{sgn}(\mu) - \sin 2\beta)(\mu + M_1 \cos^2 \theta_W + M_2 \sin^2 \theta_W)}{2(\mu + M_1)(\mu + M_2)} + \dots \quad (1.20)$$

$$m_{\tilde{\chi}_4^0} = |\mu| + \frac{m_Z^2 (\text{sgn}(\mu) + \sin 2\beta)(\mu - M_1 \cos^2 \theta_W - M_2 \sin^2 \theta_W)}{2(\mu - M_1)(\mu - M_2)} + \dots \quad (1.21)$$

$$m_{\tilde{\chi}_1^\pm} = M_2 - \frac{m_W^2 (M_2 + \mu \sin 2\beta)}{\mu^2 - M_2^2} + \dots \quad (1.22)$$

$$m_{\tilde{\chi}_2^\pm} = |\mu| + \frac{m_W^2 \text{sgn}(\mu)(\mu + M_2 \sin 2\beta)}{\mu^2 - M_2^2} + \dots \quad (1.23)$$

²³⁹ where $\tan \beta = \langle H_u^0 \rangle / \langle H_d^0 \rangle$.

²⁴⁰ The two scenarios studied in ref. [12] are the following:

²⁴¹ • **Bino NLSP:** $M_1 \sim$ few hundred GeV, $M_2, |\mu| \gg M_1$. All but the lightest
²⁴² neutralino are effectively inaccessible at the LHC due to their large masses. The
²⁴³ NLSP can always decay to $\gamma + \tilde{G}$, and if it is heavy enough, to $Z + \tilde{G}$ or $H + \tilde{G}$.

²⁴⁴ • **Wino NLSP:** $M_2 \sim$ few hundred GeV, $M_1, |\mu| \gg M_2$. The lightest neutralino
²⁴⁵ and the lightest chargino are nearly degenerate in mass, and are the only two
²⁴⁶ particles to play a role at the LHC. The decays described in the previous bullet
²⁴⁷ point can happen, as well as chargino decays to $W + \tilde{G}$.

²⁴⁸ The subject of this thesis is the classic bino NLSP decay $\gamma + \tilde{G}$.

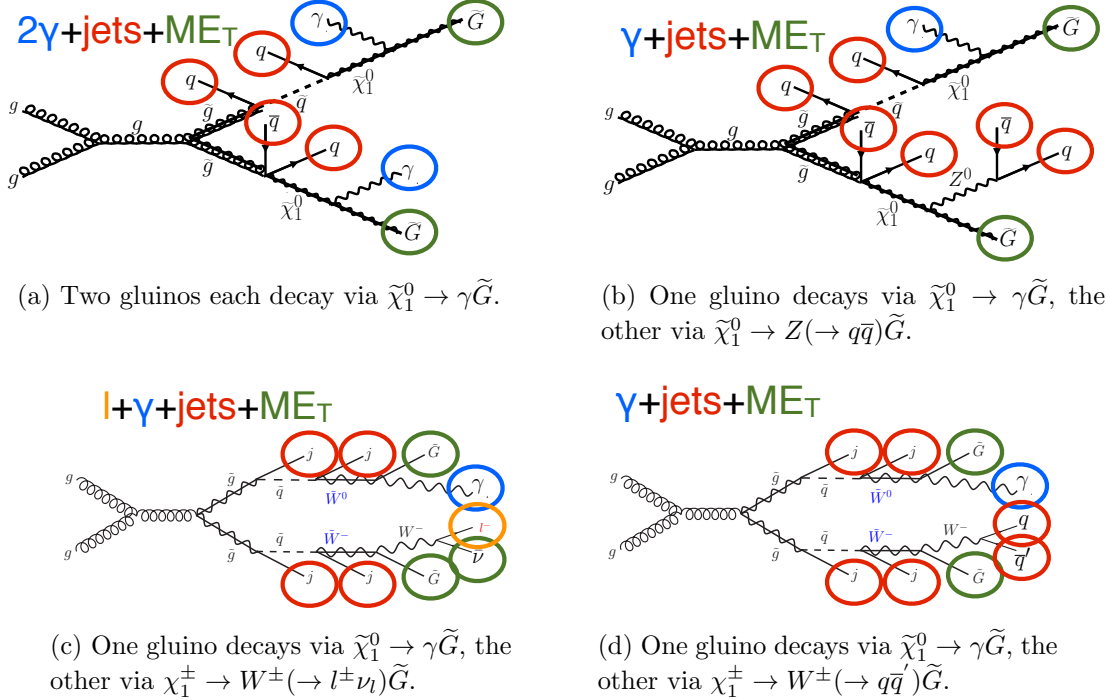


Figure 1.4: Typical LHC signatures of the bino and wino NLSP scenarios.

249 Since strong production of SUSY particles dominates over electroweak production
 250 at the LHC due to the enhanced gg parton luminosity over the $q\bar{q}$ parton luminosity,
 251 early LHC searches are particularly sensitive to light squarks and gluinos. General
 252 gauge mediation makes no a priori restrictions on the mass splitting between the
 253 strongly interacting sparticles and the weakly interacting sparticles, so models with
 254 light squarks and gluinos are viable. In fact, such models could not be probed as
 255 well at the Tevatron⁴ as they are at the LHC due to the aforementioned parton
 256 luminosities.

257 Typical LHC signatures of the bino and wino NLSP scenarios are shown in Fig-
 258 ure 1.4.

⁴Located on the Fermilab site in Batavia, Illinois, the Tevatron was a proton-antiproton collider operating at 1.96 TeV center-of-mass energy. The Tevatron ran from 1987 to 2011 [13].

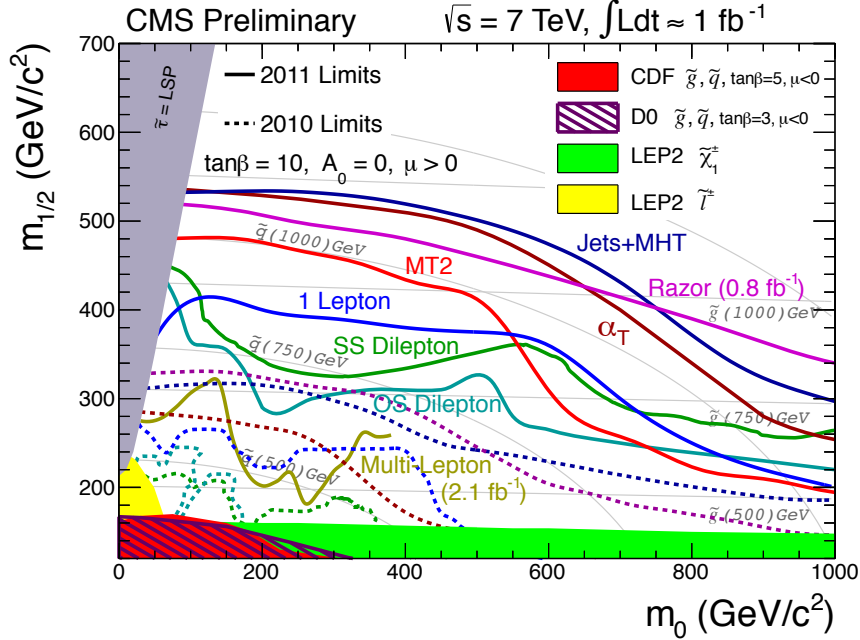


Figure 1.5: CMS limits on mSUGRA with $\tan \beta = 10$. The limits set by individual searches are shown as separate colored lines. Solid lines refer to 2011 searches (i.e. using an integrated luminosity of ~ 1 fb $^{-1}$), while dashed lines refer to 2010 searches (~ 36 pb $^{-1}$). Reprinted from ref. [16].

259 1.6 Experimental Status of SUSY

260 Collider searches for evidence of supersymmetry began in earnest in the 1980s [14]
 261 and continue to this day. Most recently, the LHC and Tevatron experiments have set
 262 the strictest limits on a variety of SUSY breaking scenarios, including GMSB and
 263 mSUGRA.

264 Figure 1.5 shows the current limits set by the CMS experiment on the mSUGRA
 265 model (with $\tan \beta = 10$) in the m_0 - $m_{1/2}$ plane. (Note that although the plot is trun-
 266 cated at $m_0 = 1000$ GeV/c 2 , some searches are sensitive out to $m_0 \sim 2000$ GeV/c 2 .)
 267 Although the LHC has pushed m_0 above ~ 1 TeV/c 2 for $m_{1/2}$ up to ~ 400 GeV/c 2 ,
 268 casting some doubt onto the theory's prospects for solving the hierarchy problem,
 269 there is still a sizable chunk of mSUGRA parameter space that is not ruled out by
 270 collider experiments. Furthermore, parts of the CMS unexplored regions overlap with
 271 areas allowed by astrophysics experiments [15].

Removed

CMS

Moriond

result

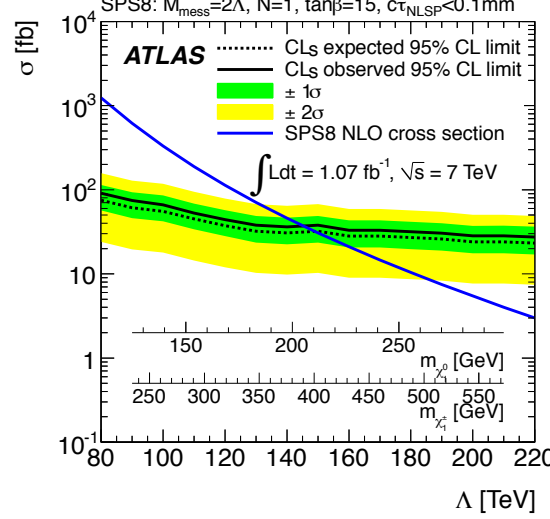


Figure 1.6: ATLAS cross section upper limit on the SPS8 [18] model of mGMSB as a function of SUSY breaking scale Λ , lightest neutralino mass $m_{\tilde{\chi}_1^0}$, or lightest chargino mass $m_{\tilde{\chi}_1^\pm}$. Values of Λ , $m_{\tilde{\chi}_1^0}$, or $m_{\tilde{\chi}_1^\pm}$ below the intersection point between the blue (predicted SPS8 cross section) and black (observed cross section upper limit) curves are excluded. The model parameters listed above the plot are defined in Secs. 1.4 and 1.5, except for τ_{NLSP} , which is the neutralino lifetime. Reprinted from ref. [10].

272 Figure 1.6 shows the most up-to-date limit (using 1 fb^{-1} of integrated luminosity
 273 collected by the ATLAS experiment [17] at the LHC) on the Snowmass Points
 274 and Slopes (SPS) model of mGMSB, dubbed SPS8 [18]. In general, the lifetime of
 275 the lightest neutralino in GMSB models can take on any value between hundreds of
 276 nanometers to a few kilometers depending on the mass of the lightest neutralino and
 277 the SUSY breaking scale [6]. The search published in ref. [10] (from which Figs. 1.6
 278 and ?? are culled) considers only *prompt* neutralino variants, i.e. with neutralino life-
 279 time short enough that the distance traveled by the neutralino before decay cannot be
 280 resolved by the detector. The most recent limits on non-prompt SPS8-style neutralino
 281 models were set by the Collider Detector at Fermilab (CDF) collaboration with 570
 282 pb^{-1} , and are shown in Figure 1.7 [11].

283 Finally, if the gravitino is to make up some or all of the dark matter, constraints
 284 on the form of gauge mediation must come from cosmological considerations and
 285 astronomical observations. The gravitino in gauge mediation models is usually very

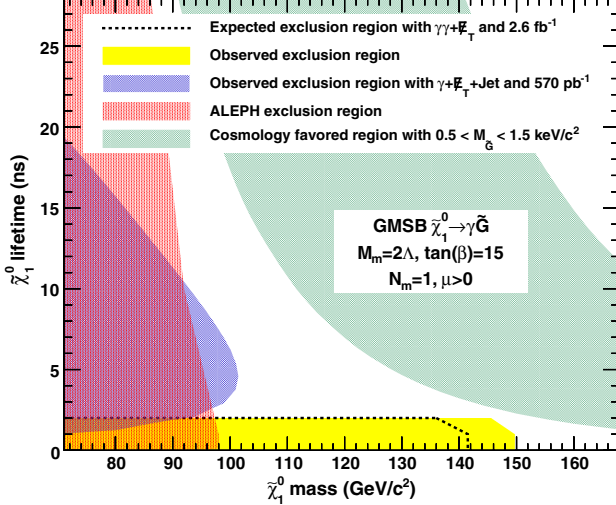


Figure 1.7: CDF exclusion contour in the $\tau_{\tilde{\chi}_1^0}$ - $m_{\tilde{\chi}_1^0}$ plane, where $\tau_{\tilde{\chi}_1^0}$ is the lifetime of the neutralino. Reprinted from ref. [11].

286 light ($\mathcal{O}(\text{eV-MeV})$) because it is proportional to the SUSY breaking scale divided by
 287 the Planck mass, and in GMSB the breaking scale is typically only of order a few
 288 hundred TeV ([6] and Sec. 1.5). A light, highly relativistic dark matter particle might
 289 have been produced, for instance, in the early, radiation-dominated period of the
 290 universe [20]. This *warm dark matter* (WDM) may be responsible for all of the dark
 291 matter needed to account for galactic structure, or it may share the duties with *cold*
 292 *dark matter* (CDM, weakly interacting particles with masses in the GeV range). In
 293 any viable model, the predicted relic density of the dark matter species must match
 294 the observed value of $\Omega h^2 \sim 0.1$ [21]. For many GMSB models, this measurement
 295 constrains the gravitino mass to the keV range [22]. This constraint, however, does
 296 not translate into a very strong bound on the lifetime of the lightest neutralino. Using
 297 the following equation (taken from [22]):

$$\tau_{\tilde{\chi}_1^0} \sim 130 \left(\frac{100 \text{ GeV}}{m_{\tilde{\chi}_1^0}} \right)^5 \left(\frac{\sqrt{\langle F \rangle}}{100 \text{ TeV}} \right)^4 \mu\text{m} \quad (1.24)$$

298 and applying the gravitino mass constraint $\sqrt{\langle F \rangle} \lesssim 3000 \text{ TeV}$ (cf. the first paragraph
 299 of Sec. 1.5 with $m_{\tilde{G}} \sim \text{keV}$) and $m_{\tilde{\chi}_1^0} = 100 \text{ GeV}$, the upper bound on the neutralino

300 lifetime is 100 meters. For $\sqrt{\langle F \rangle} \sim 100$ TeV, the neutralino lifetime is detectable on
301 collider time scales.

302 Recently, a lower bound on the WDM particle mass in either pure warm or mixed
303 warm and cold dark matter scenarios was set using observations of the Lyman- α for-
304 est. For pure WDM, $m_{\text{WDM}} > 8$ keV, while for some mixed WDM-CDM scenarios,
305 $m_{\text{WDM}} > 1.1\text{-}1.5$ keV [20, 23]. These bounds and others have motivated the develop-
306 ment of more complicated gauge mediation models [23]. However, rather than focus
307 on a specific GMSB model, of which there are many, the search detailed here is in-
308 terpreted in a minimally model dependent way. With this approach, the results can
309 be applied to many competing models. The remainder of this thesis is devoted to the
310 experimental details of the search, analysis strategy, and presentation of the results.
311 The work described in this thesis forms the basis for the CMS public result “Search
312 for Supersymmetry in Events with Photons and Missing Energy” [19], published in
313 April 2012.

³¹⁴ **Chapter 2**

³¹⁵ **The Large Hadron Collider**

³¹⁶ At a 2010-2011 energy of 3.5 TeV/beam (7 TeV/beam design [24]) and maximum
³¹⁷ instantaneous luminosity of $3.55 \times 10^{33} \text{ cm}^{-2} \text{ s}^{-1}$ [25] ($10^{34} \text{ cm}^{-2} \text{ s}^{-1}$ design [24]),
³¹⁸ the Large Hadron Collider (LHC) is the highest energy and highest intensity proton-
³¹⁹ proton collider ever built. Its purpose is to allow the four LHC experiments to explore
³²⁰ TeV scale physics. For CMS and ATLAS, this implies examining the origins of EWSB
³²¹ via searches for the SM Higgs boson and physical phenomena not predicted by the
³²² SM that may explain the mass hierarchy in the SM. It also includes searches for
³²³ possible dark matter candidates that are often proposed to have masses at the weak
³²⁴ scale. The LHC needs to provide high energy proton collisions because the masses
³²⁵ of the sought-after particles are higher than those already incorporated into the SM.
³²⁶ It must also provide an unprecedented collision rate because signatures of the Higgs
³²⁷ boson and physics beyond the SM are very rare compared to SM processes.

³²⁸ The rest of this chapter is devoted to an overview of the LHC machine. Sec-
³²⁹ tion 2.1 gives the overall layout of the machine and design choices made in light of
³³⁰ energy and luminosity demands. Section 2.2 describes the LHC injection scheme. The
³³¹ different types of magnets and their functions is illustrated in Section 2.3, and finally
³³² the radiofrequency cavities are covered in Section 2.4. Unless otherwise noted, all

³³³ information in this chapter comes from ref. [24].

³³⁴ 2.1 Design Considerations and Performance Lim- ³³⁵ itations

³³⁶ The layout of the 26.7-km long [26] LHC ring, located \sim 100 m underground on the
³³⁷ border between France and Switzerland northwest of Geneva, is shown in Figure 2.1.
³³⁸ The two circulating beams of protons travel in opposite directions, colliding only at
³³⁹ the experimental points. There are eight straight sections, each \sim 528 m long, and
³⁴⁰ eight arcs, each made of 23 106.9-m long arc cells. Beam crossings occur in four of
³⁴¹ the straight sections. The arcs contain six 14.3-m long dipole magnets, the cryogenics
³⁴² to cool the magnets, and short straight sections (SSS) with focusing and corrector
³⁴³ magnets. The high luminosity experiments CMS and ATLAS are located diametrically
³⁴⁴ opposite each other on the ring, ensuring that in principle each should receive the
³⁴⁵ same integrated luminosity from the LHC.

³⁴⁶ To achieve a maximum energy per beam of 7 TeV, the peak magnetic field pro-
³⁴⁷ duced by the dipole magnets must be 8.33 T, demanding the use of superconducting
³⁴⁸ technology. Due to the like charges of the two beams, two separate magnet systems
³⁴⁹ and evacuated beam pipes must be used to accelerate the protons in opposite direc-
³⁵⁰ tions. Space limitations in the LHC tunnel, which was previously used for the LEP
³⁵¹ collider, prevent the installation of two separate rings of magnets, so each dipole in-
³⁵² stead contains two beam pipe bores and two sets of superconducting coils to produce
³⁵³ two fields in opposite directions. In order to safely operate the magnets at 8.33 T,
³⁵⁴ the cryogenic bath temperature is chosen to be 1.9 K, colder than any other acceler-
³⁵⁵ ator cryogen and well below the critical temperature of the niobium-titanium (NbTi)
³⁵⁶ superconducting wires of 9.2 K [29]. The extremely low bath temperature leads to
³⁵⁷ a lessened heat capacity in the wires and consequently a lower energy threshold for

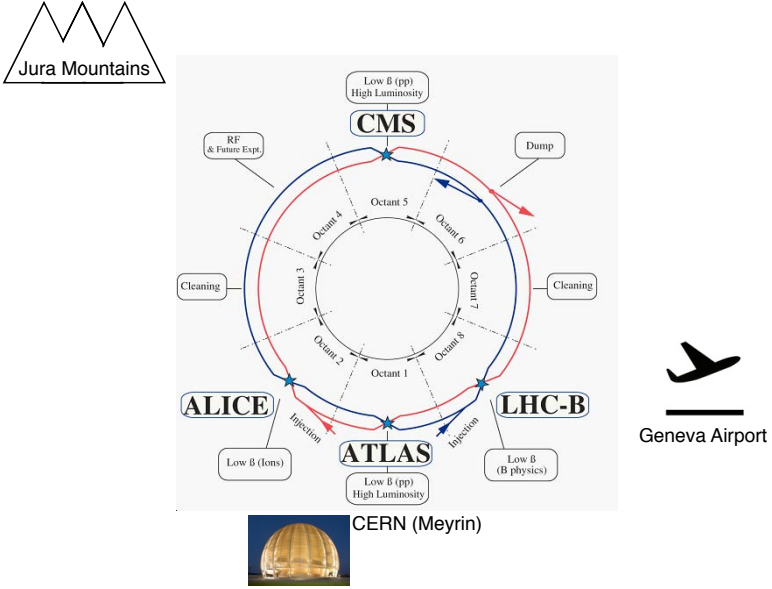


Figure 2.1: Bird's-eye view of the LHC ring, showing the locations of the experiments and local landmarks. Arrows show the beam direction. The ring figure is reprinted from Fig. 2.1 of ref. [24]. The CERN Globe of Innovation photo comes from ref. [27] and the airplane cartoon comes from ref. [28].

358 triggering a quench, so movements and heat dissipation within the cables must be
 359 controlled more tightly than in previous accelerators.

360 The LHC beams are arranged in bunches of protons, with each bunch separated
 361 by an integer multiple of the 25 ns minimum bunch spacing. The machine luminosity
 362 L is given by

$$L = \frac{N_b^2 n_b f_{\text{rev}} \gamma_r}{4\pi \epsilon_n \beta^*} F \quad (2.1)$$

363 where N_b is the number of protons per bunch (squared for the two beams), n_b is
 364 the number of bunches per beam, f_{rev} is the bunch revolution frequency, γ_r is the
 365 relativistic γ of the protons, ϵ_n is the normalized transverse beam emittance, β^* is
 366 the value of the β function at the collision point, and F is a geometrical factor less
 367 than one related to the *crossing angle* of the bunches with respect to the horizontal

368 (ATLAS) or vertical (CMS) planes and the beam size. The normalized transverse
 369 beam emittance is a measure of the RMS spread of the beam in the plane transverse
 370 to its direction of motion, irrespective of its energy. A smaller emittance implies that
 371 particles are squeezed into a smaller area in phase space, leading to larger luminosity.
 372 The β function is defined as the square of the transverse beam size divided by the
 373 emittance. It describes the oscillations of the transverse beam size as a function of
 374 position in the ring. To achieve high luminosity, β^* is the minimum of the β function,
 375 and it is related to the focusing strength of the triplet magnets near the interaction
 376 points. In accelerating sections of the ring, the β function gets large so that the proton
 377 momenta may be more uniform. Each piece of the luminosity is limited by safety or
 378 design considerations.

379 Above some saturated bunch intensity, nonlinear beam-beam interactions experi-
 380 enced by the protons during collisions cause the luminosity to scale as N_b , not N_b^2
 381 [30]. The scale of these interactions is set by N_b/ϵ_n , and the size of the beam pipe and
 382 maximum β function limit ϵ_n to $3.75 \mu\text{m}$. Instabilities are also introduced through
 383 interactions between the protons and the wall of the beam pipe that scale with the
 384 beam current. Last but not least, the beam dump and magnet safety systems limit the
 385 total stored energy in the ring. For these reasons, the maximum number of bunches
 386 is limited to 1.15×10^{11} . In bunches of this proton multiplicity, the average num-
 387 ber of proton-proton collisions per bunch crossing, or *pileup*, in CMS and ATLAS is
 388 approximately 20. This unprecedented level of pileup poses unique triggering, event
 389 reconstruction, and analysis challenges for the experiments.

390 n_b can range from zero to 2808 and had a maximum of ~ 1400 in 2011, corre-
 391 sponding to 50 ns bunch spacing. f_{rev} is set by the circumference of the ring to 11.2
 392 kHz [31]. γ_r is set by the beam energy, which was 3.5 TeV in 2011.

393 The mechanical aperture of the triplet assemblies of quadrupole magnets limit
 394 the minimum β^* to 0.55 [31] and maximum crossing angle to $285 \mu\text{rad}$ [31] at the

The LHC injection complex

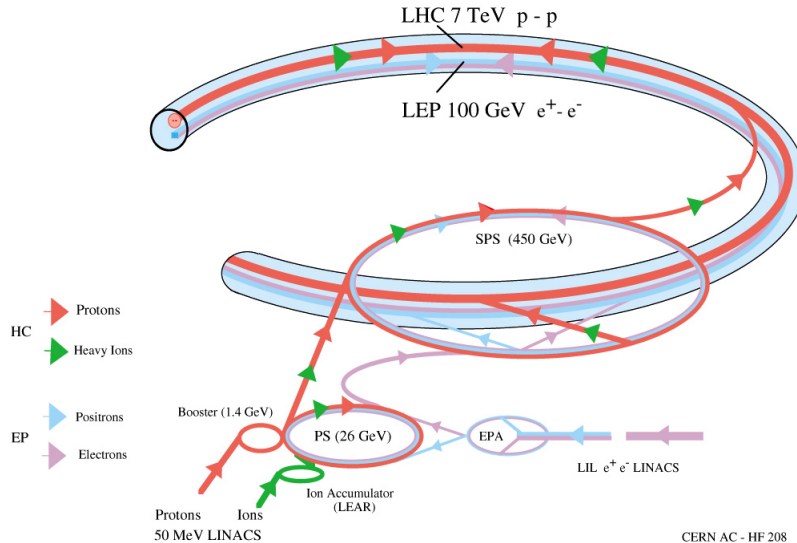


Figure 2.2: Overview of the LHC injector complex at CERN [32].

395 interaction points. The purpose of the crossing angle is to prevent parasitic collisions
 396 in the 23-m length of shared beam pipe upstream and downstream of the interaction
 397 points.

398 2.2 Beam Injection

399 The ultimate source of protons for the LHC is a bottle of hydrogen connected to the
 400 CERN Linac2 linear accelerator, which accelerates the protons up to 50 MeV. From
 401 there they enter the Proton Synchrotron Booster (PSB), which accelerates them to
 402 1.4 GeV, and then the Proton Synchrotron (PS) itself, which brings them to 25 GeV.
 403 The Super Proton Synchrotron (SPS) is the next stage, accelerating the protons to
 404 an energy of 450 GeV. Finally, they leave the SPS and enter the LHC, where they are
 405 accelerated to the desired beam energy (3.5 TeV in 2011). An overview of the LHC
 406 injector complex is shown in Figure 2.2.

407 The 25-ns spaced bunches (or 50 ns for 2011 operation) are produced in trains
 408 of 72 in the PS via a process of splitting six initial bunches into 12 smaller bunches

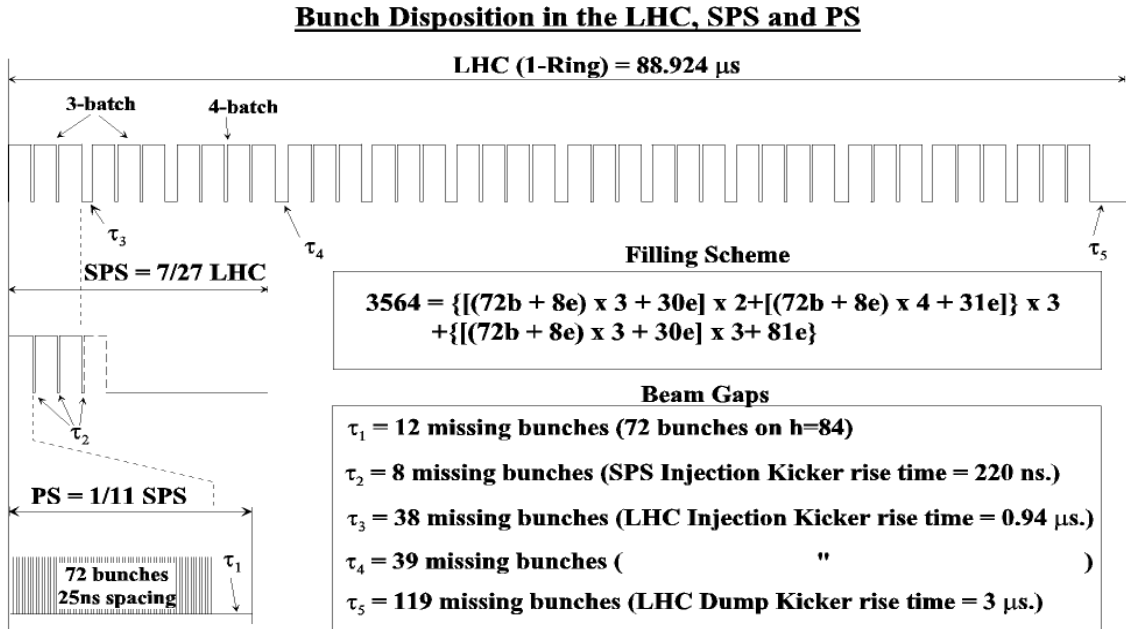


Figure 2.3: LHC injection scheme. Reprinted from Fig. 12.2 of ref. [24].

409 at specified points along the ring. At the end of each train is a 300 ns (12 bunch)
 410 gap, which is an artifact of the splitting process. The SPS is limited by its maximum
 411 allowed bunch intensity to storing three or four PS trains at a time. There is an 220
 412 ns (8 bunch) gap at the end of each train due to the SPS injection kicker rise time.
 413 The LHC is filled three or four trains at a time from the SPS. At the end of each
 414 three-train and four-train group is a gap of 0.94 μ s (38 or 39 bunches) due to the
 415 LHC injection kicker rise time. Finally, at the end of an entire 88.924- μ s long LHC
 416 orbit is a gap of 3 μ s (119 bunches), known as the *abort gap*, to allow for the LHC
 417 dump kicker rise time. The injection scheme is shown in Figure 2.3.

418 LHC injection occurs at points 2 and 8. At the intersection of the SPS-LHC
 419 transfer line and the LHC beam pipe are five septum magnets that deflect the bunches
 420 12 mrad horizontally into orbit. The septum magnets have a gap into which the
 421 beam is injected as well as two separate holes for the circulating beams, as shown in
 422 Figure 2.4. Four kicker magnets then deflect the bunches 0.85 mrad vertically into
 423 orbit. The kicker magnets supply a pulsed magnetic field with a 0.94 μ s rise time

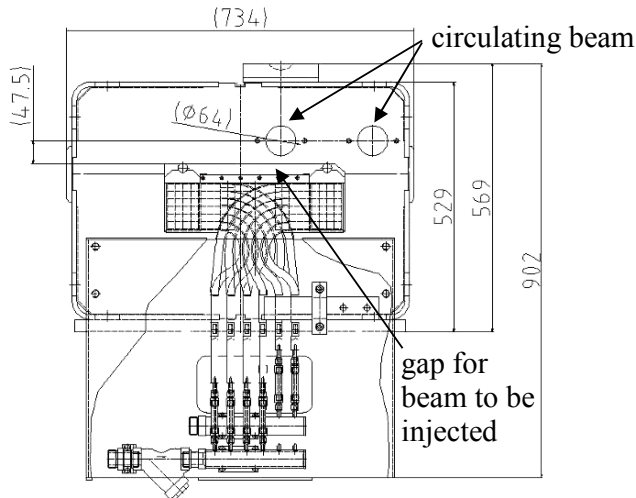


Figure 2.4: Cross-sectional view of septum magnet (beam direction is into or out of the page) showing the holes for the circulating beams and the separate gap for injected particles. Reprinted from Fig. 11.2 of ref. [24].

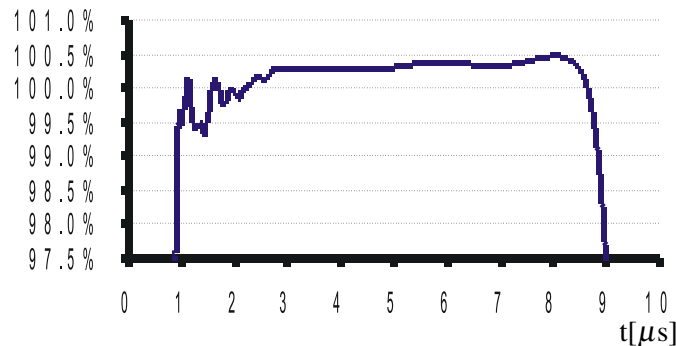


Figure 2.5: LHC injection kicker pulse shape. The *y*-axis measures percentage of maximum current. Reprinted from Fig. 11.7 of ref. [24].

424 (see Fig. 2.3) and a 5.84(7.86) μs flat top for three-train(four-train) injection (see
 425 Figure 2.5). To limit emittance growth at injection due to over- or under-kicking the
 426 injected bunches such that they miss the core of the LHC orbit, the kicker current is
 427 limited to $< 0.5\%$ flat top ripple in any direction.

428 2.3 Magnets and Cryogenics

429 There are 1232 twin-bore dipole magnets along the LHC ring used for establishing
 430 the circular orbit of the protons. They consist of two evacuated beam pipes, each

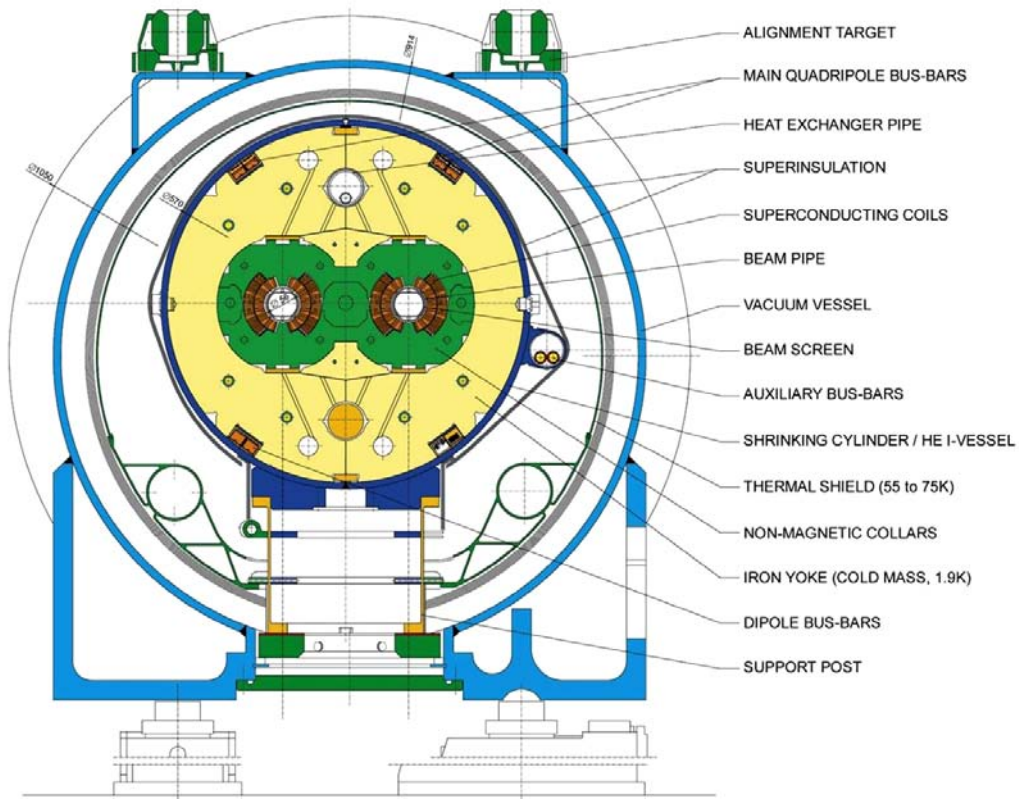


Figure 2.6: Cross-sectional view of LHC dipole + cryostat. Reprinted from Fig. 3.3 of ref. [24].

431 flanked by its own set of superconducting coils, inside an iron yoke which serves as
 432 the 1.9 K cold mass. The entire assembly sits inside a helium vessel, which is itself
 433 surrounded by a vacuum chamber thermally insulating the cold mass from the room
 434 temperature LHC cavern. The entire dipole + cryostat device is ~ 16.5 m long and
 435 weighs about 27.5 t. A cross-sectional view of the dipole is given in Figure 2.6.

436 To provide a centripetal Lorentz force on the protons, the dipole field points
 437 vertically up or down, depending on the sense of the beam. The magnetic field lines for
 438 a single beam pipe are shown in Figure 2.7. Figure 2.8 shows the coil windings in two
 439 bores. To provide the correct field direction, the coils are wound around blocks that
 440 are ~ 14 m long (the length of the dipole), so that each winding has a circumference
 441 of ~ 28 m.

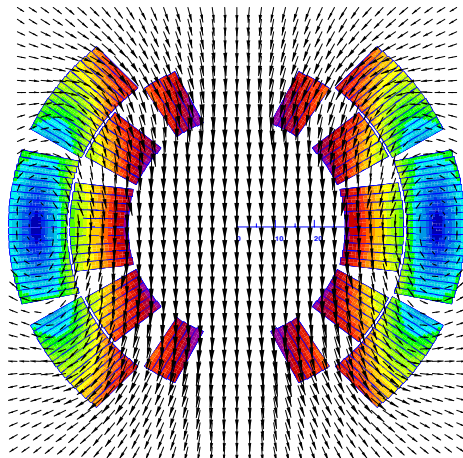


Figure 2.7: Magnetic field lines of the dipole field. The beam direction is into the page. Reprinted from Fig. 4 of ref. [33].

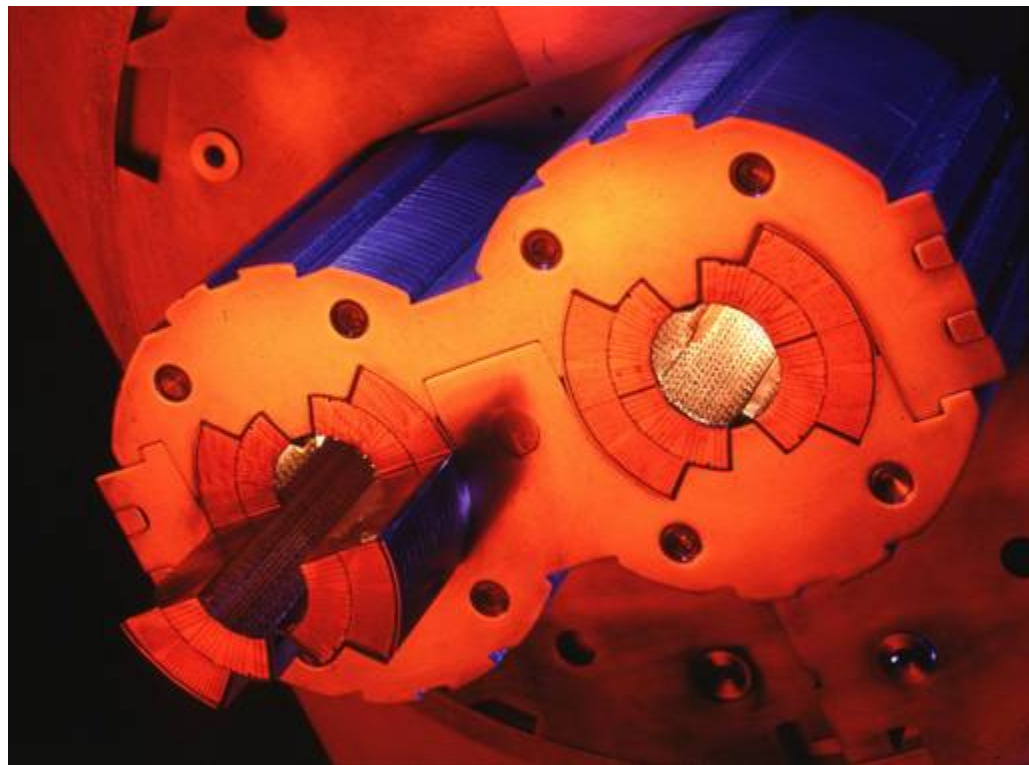


Figure 2.8: Superconducting coils in a twin-bore dipole [34].

442 In addition to the dipoles, a number of different types of orbit corrector magnets
 443 are installed throughout the ring. The main quadrupole magnets, as well as higher
 444 order field corrector magnets, are located in the arcs and short straight sections. The
 445 function of these magnets is to provide fine grained control over the magnetic field
 446 in order to keep the bunches in the proper orbit and control the emittance and β
 447 functions.

448 In the straight sections, there are four specialized types of magnets related to SPS
 449 extraction and bringing the beams into collision. Matching section quadrupoles near
 450 the transfer lines help to match the injected bunch orbit to the circulating bunch orbit.
 451 Dispersion suppressors, consisting of dipoles and quadrupoles, help to reduce beam
 452 dispersion near the collision points due to off-momentum protons. Matching section
 453 separation dipoles control the separation between the two beams near the collision
 454 points. The magnets that perform the final squeeze of the beams before collision,
 455 called the low- β inner triplets, must provide a very high field gradient of 215 T/m,
 456 withstand a high radiation dose, and sustain high heat loads in the superconducting
 457 coils.

458 The superfluid helium cryogen is delivered to the magnets via a distribution line
 459 from the main refrigerator. A cross section of the LHC tunnel, showing the cryogen
 460 delivery apparatus for a dipole, is shown in Figure 2.9.

461 2.4 Radiofrequency Cavities

462 LHC bunches are captured and accelerated in 400 MHz superconducting radiofre-
 463 quency (RF) cavities. 400 MHz defines the bunch length of $\lesssim 2$ ns. As bunches pass
 464 through the cavities, the oscillating electric field is at its peak and accelerates the
 465 protons through a potential difference of 2 MV per cavity (16 MV per turn). The
 466 finite bunch length is due to particles that arrive out of phase with the electric field

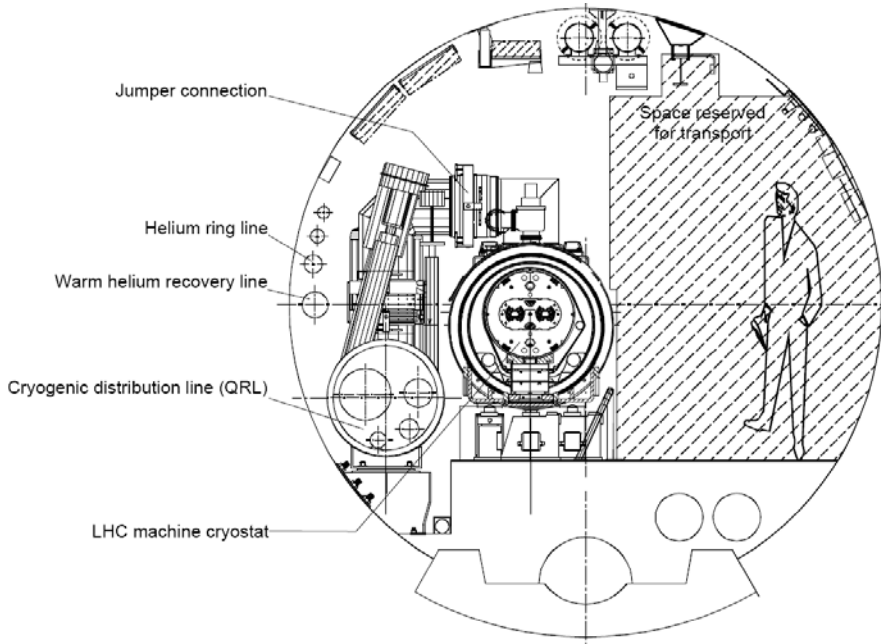


Figure 2.9: Cross section of the LHC tunnel, showing the cryogen delivery apparatus for a dipole. Reprinted from Fig. 7.1 of ref. [24].

467 due to deviations in their momenta from the nominal. During a ramp of the beam
 468 energy from 450 GeV to 3.5 or 7 TeV, bunches repeatedly travel around the ring, re-
 469 ceiving an energy kick each time, until the desired energy is reached. Feedback from
 470 the RF accelerating system causes an increase in magnet current to keep the bunches
 471 in a fixed orbit.

472 Superconducting material (niobium) coats the cylindrical walls of the cavity. RF
 473 power is coupled to the cavity via a klystron. The RF electric field standing wave is set
 474 up across the cavity in the beam direction. The transverse magnetic field dissipates
 475 some energy into the walls, but much less than in a normal conducting cavity.

476 **Chapter 3**

477 **The Compact Muon Solenoid**
478 **Experiment**

479 The Compact Muon Solenoid (CMS) detector sits at point 5 of the LHC ring, diamet-
480 rically opposite the ATLAS detector at point 1. It is a 4π hermetic general purpose
481 detector, meaning that it has the capability to detect charged and neutral hadrons,
482 photons, electrons, muons, taus, neutrinos, and non-Standard-Model particles pre-
483 dicted to escape the detector with good efficiency over a large range of rapidity.
484 Its main distinguishing feature is a superconducting solenoid that provides a 3.8T
485 magnetic field parallel to the beam line. This strong magnetic field allows precise de-
486 termination of the momentum and charge of muons and electrons up to a momentum
487 of ~ 1 TeV.

488 The origin of the CMS coordinate system is at the nominal interaction point. The
489 y -axis points skyward, the x -axis points towards the center of the LHC ring, and
490 the z -axis points counterclockwise along the LHC ring. r denotes radial distances
491 from the beam line, ϕ is the azimuthal angle measured with respect to the positive
492 x -axis, and θ is the polar angle measured with respect to the positive z -axis. The
493 *pseudorapidity* η is defined as $\eta = -\ln \tan(\theta/2)$, and is a good approximation to

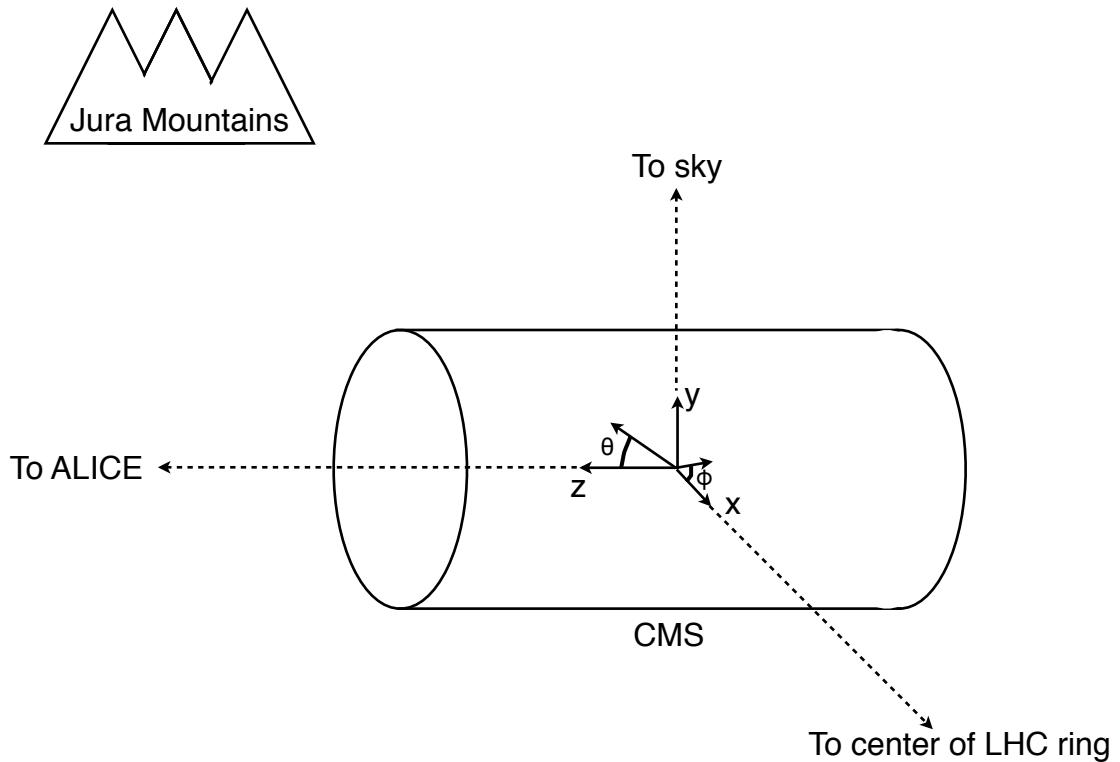


Figure 3.1: CMS coordinate system.

494 rapidity $y = (1/2) \ln((E + p_z c)/(E - p_z c))$ for relativistic particles. The transverse
 495 momentum and energy (p_T and E_T) of a particle are defined as $p_T = p \cos \phi$ and
 496 $E_T = E \cos \phi$, where p and E are the magnitude of the particle's momentum vector
 497 and the particle's total energy, respectively. A depiction of the CMS coordinate system
 498 is shown in Figure 3.1.

499 The CMS sub-detectors are arranged in concentric cylindrical layers, plus “end-
 500 caps,” around the beam line, as shown in Figure 3.2. Closest to the beam line are
 501 three layers of silicon pixel detectors, with the innermost at radius 4.4 cm and out-
 502 ermost at radius 10.2 cm [35]. Including the pixel endcaps, the total pixel coverage

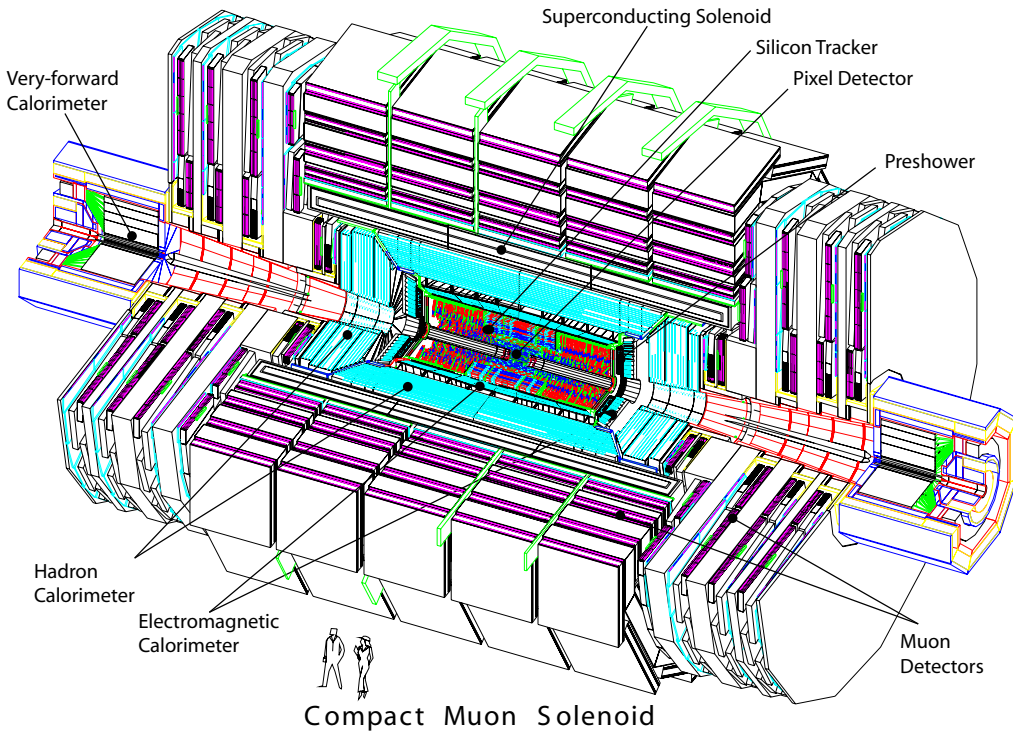


Figure 3.2: Cutaway view of CMS. Reprinted from Fig. 1.1 of ref. [35].

503 extends to $\eta = 2.5$ [35]. The pixel detector plays an important role in determining the
 504 proton-proton interaction position (*beam spot*) and the impact parameters of charged
 505 particle trajectories, and is critical for the measurement of decay positions some dis-
 506 tance from the beam spot (*displaced vertices*), such as those due to the showering and
 507 hadronization of a b quark.

508 The 10 next layers of CMS are comprised of silicon microstrip detectors, with the
 509 outermost layer at a radius of 1.3 m from the beam line [35]. As for the pixel detectors,
 510 the silicon strip endcap extended tracking coverage to $\eta = 2.5$. The silicon microstrip
 511 layers are the workhorse of the CMS tracking system, and provide excellent charged
 512 particle momentum resolution and track finding efficiency.

513 Outside the tracking detectors are the calorimeters, starting with the single-layer
 514 lead tungstate crystal electromagnetic calorimeter at a radius of 1.3 m from the beam
 515 line (location of crystal front faces) [35]. Each crystal is 23 cm long, corresponding

516 to 25.8 radiation lengths (X_0) [35]. The crystal dimensions are such that most of one
 517 electromagnetic shower, and no more, can be contained in a single crystal, leading to
 518 excellent energy resolution for photons and electrons. The electromagnetic calorime-
 519 ter radial and endcap layers cover a pseudorapidity range up to 3.0. A lead/silicon
 520 sampling calorimeter sits in front of the crystal endcaps to provide better rejection
 521 of neutral pions.

522 The last layer of calorimetry inside the solenoid is the brass/scintillator sampling
 523 hadronic calorimeter, which has a radial extent from 1.77-2.95 m [35]. The hadronic
 524 barrel and endcap calorimeters cover up to $|\eta| = 3.0$, while the iron/quartz-fiber for-
 525 ward hadronic calorimeter covers the region $3.0 \leq |\eta| \leq 5.2$.¹ There is one more
 526 layer of hadronic calorimetry outside the solenoid in $|\eta| < 1.3$ which, together with
 527 the layers inside the solenoid, provides approximately 12 hadronic interaction lengths
 528 of instrumented absorber. Because of its large $|\eta|$ coverage and depth, the hadronic
 529 calorimeter provides good missing transverse energy resolution and accurate measure-
 530 ments of high energy jets.

531 The iron return yoke of the solenoidal magnetic field is interleaved with muon
 532 detectors from 4.1-7.4 m in r and 6.6-10.6 m in z , providing muon detection up to
 533 $|\eta| = 2.4$ [35]. In the barrel region of $|\eta| < 1.2$, drift tubes are used to read out the
 534 muon tracks, while in the endcaps cathode strip chambers are used. Due to their
 535 speed, resistive plate chambers are used throughout the muon system to provide
 536 an independent trigger and timing measurement. Combining the tracker and muon
 537 system hits, the momenta and charge of muons up to $p_T = 1$ TeV can be precisely
 538 reconstructed.

539 A longitudinal quarter cross-sectional view of CMS is shown in Figure 3.3. The
 540 remainder of this chapter is devoted to explaining the CMS subdetectors and readout

¹The Centauro and Strange Object Research (CASTOR) and Zero Degree Calorimeter (ZDC) detectors provide additional calorimetry beyond $|\eta| = 5.2$. However, they are mainly used in the heavy ion and diffractive physics programs of CMS, and play no role in the detection of heavy SUSY particles. Therefore, they will not be discussed here.

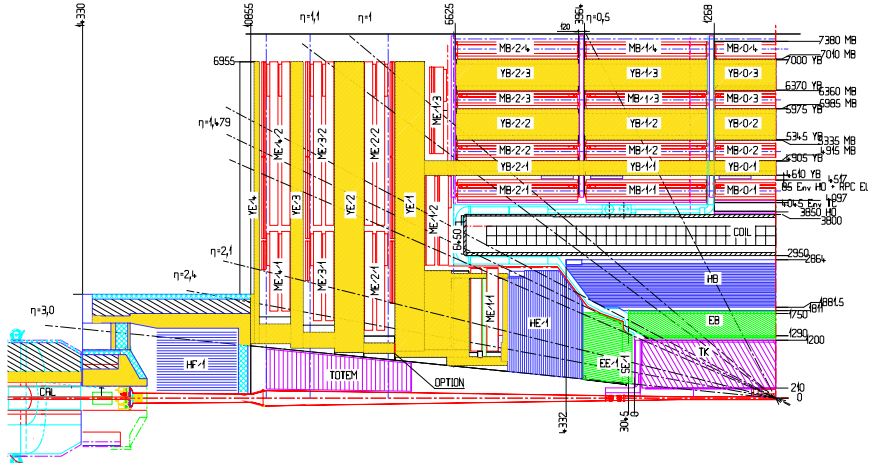


Figure 3.3: Longitudinal quarter cross-sectional view of CMS. The nominal interaction point is at the lower right-hand corner of the drawing. The tracker is shown in purple diagonal hashing, the electromagnetic calorimeter in green, the hadronic calorimeter in blue, and the muon stations in red. The solenoid is shown in black and white and labeled COIL, and the magnet return yoke is shown in yellow. Radial and longitudinal distances are measured in millimeters. Reprinted from Fig. CP 1 of ref. [36].

systems. Section 3.1 describes the subdetector technologies and performance benchmarks, while Section 3.2 details the CMS trigger and data acquisition systems and framework for promptly reconstructing and transferring data worldwide. For a thorough description of CMS, see ref. [35]. Unless otherwise noted, all information in this chapter comes from ref. [35].

3.1 The Detectors and Their Operating Principles

3.1.1 Tracking System

Given the LHC design instantaneous luminosity, efficient reconstruction of charged particle tracks from transverse momenta of 1 GeV up to 1 TeV can only be achieved with a low occupancy tracker. For $r < 10$ cm, the hit rate density is highest, leading to the choice of $100 \mu\text{m} \times 150 \mu\text{m}$ silicon pixel sensors for hit detection. For $20 \text{ cm} < r < 110 \text{ cm}$, the lower hit rate allows the use of silicon strips, with length along z of

order centimeters and length along the $r \cdot \phi$ curve of order hundreds of microns. This design leads to a pixel hit occupancy of $\sim 10^{-4}$ /pixel/BX and a strip hit occupancy of $\sim 10^{-2}$ /pixel/BX, where BX refers to 1 LHC bunch crossing.

As radiation dose from hadrons accumulates over the lifetime of the tracker, silicon leakage current through the semiconductor junctions increases, heating up the sensors. Since the leakage current itself depends on temperature, this can lead to *thermal runaway* that damages the detector. To avoid this, the tracker must be cooled to approximately -10°C . Operating at this temperature, the signal:noise ratio in the silicon sensors is 10:1, and should remain at that level over the 10-year lifetime of the tracker.

At its thickest ($|\eta| \sim 1.5$), the tracker depth (including services) is $\sim 1.8X_0$, and the depth falls off to $\sim 1X_0$ in thinner areas. Unfortunately, the large mass of the tracker degrades somewhat the performance of the electromagnetic calorimeter behind it, as $\sim 50\%$ of photons will convert to e^+e^- pairs in the tracker.

Pixel Detector

A longitudinal quarter view of the three barrel pixel (BPix) layers and two forward pixel (FPix) disks is shown in Figure 3.4. There are 768 BPix modules in total. Each BPix layer is divided into 32 ϕ -wedges, with eight modules per wedge arranged end-to-end in z . The ϕ -wedges operate nearly independently in terms of clock and readout. Each FPix disk consists of 24 ϕ -wedges, with pie-shaped modules attached to the front and back of the disk, for a total of 192 modules. The front- and back-side modules of the FPix disks are constructed of different sized *plaquettes*, or multi-pixel sensor chips, such that the gaps in the front-side module are covered by plaquette area in the back-side module and vice versa. An illustration of the BPix and FPix mechanical layouts is given in Figure 3.5.

Since the electric field in the depletion region of the BPix sensors is perpendicular

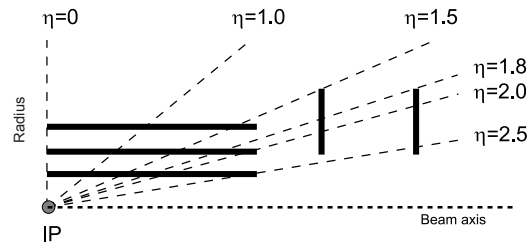
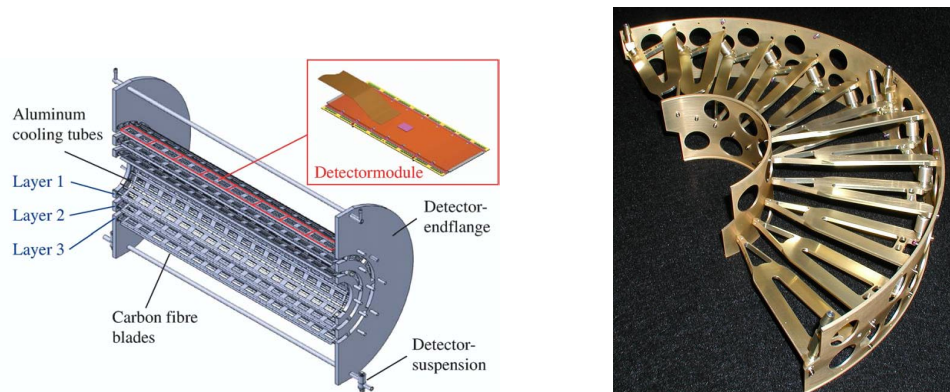


Figure 3.4: Longitudinal quarter view of the pixel detector. Reprinted from Fig. 3.6 of ref. [35].



(a) Cutaway view of the barrel pixel layers, showing the three layers and the eight end-to-end modules along z . Reprinted from Fig. 3.11 of ref. [35].

(b) Half-disk of the forward pixel detector, showing the 12 pie-shaped module mounts. Reprinted from Fig. 3.15 of ref. [35].

Figure 3.5: BPix and FPix mechanical structures.

579 (i.e. pointing along r) to the magnetic field of CMS (i.e. pointing along z), the charge
 580 carriers in the silicon experience a Lorentz drift along ϕ . The multi-pixel sensor pitch
 581 is such that this causes the charge from one particle hit to be shared among multiple
 582 pixels. Particle hits are reconstructed reading out the analog pixel signal and inter-
 583 polating between signals in multiple pixels. This method achieves a $15\text{-}20 \mu\text{m}$ spatial
 584 resolution, which is comparable to the sensor pitch. To induce this effect in FPix,
 585 the sensor wedges are tilted by the approximate BPix Lorentz angle of 20° [37] with
 586 respect to the y -axis.

587 Each multi-pixel sensor consists of an array of 52×80 n-type pixels implanted onto
 588 an n-type substrate with $320 \mu\text{m}$ thickness. The other face of the substrate is covered
 589 with a thin layer of p-type semiconductor. Except for the outer edges, which are held
 590 at ground potential to prevent sparking between the sensor edges and the connected
 591 readout chip [38], the p-side is reverse biased at 150 V (BPix) or 300 V (FPix). The
 592 pixels are held at ground potential. A particle entering through the p-side will cause
 593 a burst of current to flow across the p-n junction. The charge will be collected by the
 594 pixels, which are bump-bonded to the readout. The BPix and FPix sensors employ
 595 slightly different technologies for electrically isolating the individual pixels, but both
 596 rely on the idea of surrounding the pixels with a p-type material to provide a p-n
 597 junction that acts as a barrier to current flow.

598 Each 52×80 pixel sensor is bump bonded to a readout chip (ROC). The ROCs
 599 provide zero suppression and amplify, buffer, and communicate the signals from the
 600 sensors. A single token bit manager (TBM) controls ~ 16 ROCs in the barrel or ~ 24
 601 ROCs in the endcaps. Its purpose is to distribute the clock and trigger to the ROCs
 602 (the latter initiates a transmission of the signal further upstream to be assembled
 603 into the full event readout of CMS). The clock and trigger are supplied by the pixel
 604 front end controller (pFEC), which interfaces to the central clock and data acquisition
 605 systems. Analog signals that are collected from the pixel front ends are digitized by

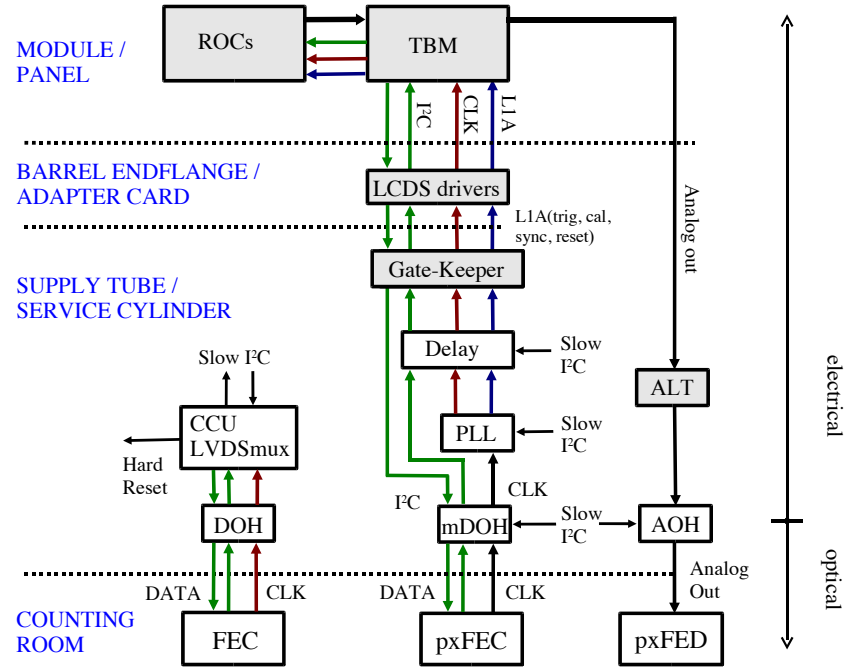


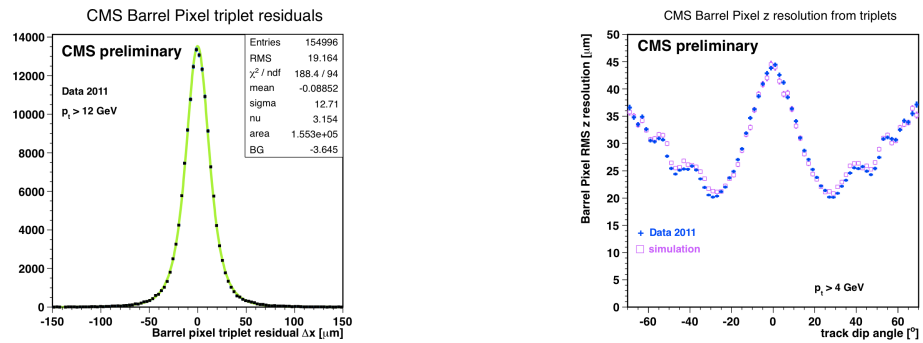
Figure 3.6: Pixel control and readout system. Reprinted from Fig. 3.9 of ref. [35].

606 the pixel front end digitizer (pxFED). A diagram of the readout system is shown in
 607 Figure 3.6.

608 Figure 3.7 shows some results highlighting the performance of the pixel detector.

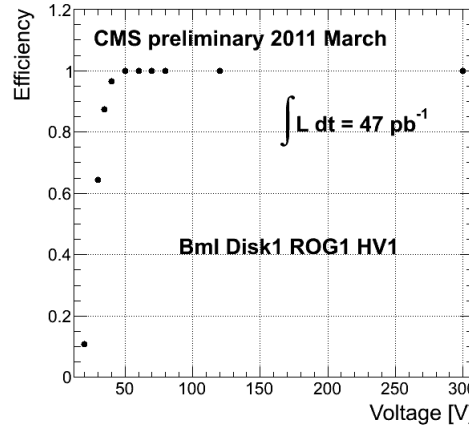
609 Silicon Strip Tracker

610 The silicon strip tracker is divided into four parts: the inner barrel (TIB) and inner
 611 disks (TID), covering the radial extent $20 \text{ cm} < r < 55 \text{ cm}$ and z extent $80 \text{ cm} <$
 612 $|z| < 90 \text{ cm}$; and the outer barrel (TOB) and endcap (TEC), covering the radial
 613 extent $61 \text{ cm} < r < 108 \text{ cm}$ and z extent $124 \text{ cm} < |z| < 282 \text{ cm}$. A number of the
 614 tracker layers and endcaps hold double-sided strip modules (shown as double lines
 615 in Figure 3.8), with the rear module tilted at an angle of 100 mrad with respect to
 616 the front module, to provide a measurement in two coordinates. There are a total of
 617 15,148 modules in the tracker, arranged as shown in the longitudinal cross-sectional
 618 view of Fig. 3.8. For the TIB and TOB, the modules are arranged in straight rows



(a) BPix hit resolution in the $r \cdot \phi$ coordinate [39].

(b) BPix hit resolution in the z coordinate vs. track dip angle, showing the effect of charge sharing on resolution [40].



(c) Pixel reconstruction efficiency vs. bias voltage for a group of three wedges in FPix [41].

Figure 3.7: Pixel detector performance highlights.

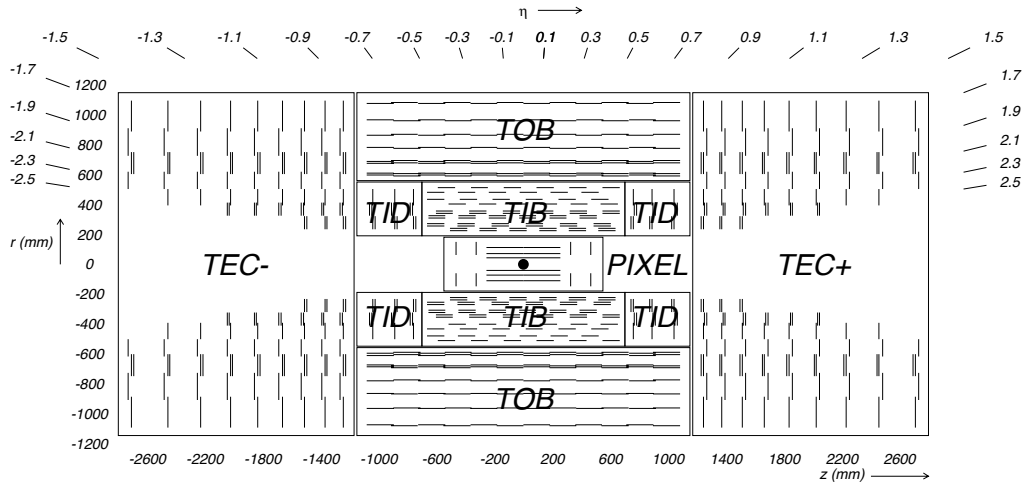


Figure 3.8: Longitudinal cross section of the silicon strip detector. Reprinted from Fig. 3.1 of ref. [35].

619 end-to-end along z , with repeating rows covering the full 2π extent in ϕ . In each of the
 620 TID disks, the modules are arranged into three concentric circular rings of increasing
 621 r . In the TEC, the modules are affixed to ϕ -wedges called *petals*. One side of the TEC
 622 and its petal structure is shown in Figure 3.9.

623 Like the pixels, the strip sensors generate a signal when current flows across a
 624 p-n junction in response to interaction with a charged particle. Whereas the pixels
 625 are n-type implants on an n-type substrate, with a solid p-type rear layer to which
 626 the high voltage is connected, the strips are p-type implants on an n-type substrate,
 627 with a solid n-type rear layer connecting to the high voltage. The p-n junction in the
 628 strip sensors is at the strip-substrate boundary, whereas in the pixel sensors it is at
 629 the boundary between the rear layer and the substrate. Each sensor has either 512
 630 or 768 electrically isolated strips, with pitch varying from 80-205 μm depending on
 631 location. Strip lengths in z range from ~ 10 to ~ 25 cm. Thin (320 μm) sensors are
 632 used in the TIB, TID, and inner four rings of the TEC, while thick (500 μm) sensors
 633 are used in the TOB and the outer rings of the TEC. The thicker sensors compensate
 634 for the increased strip capacitance (and hence electronics noise) of the longer strips
 635 in the outer layers/disk of the tracker such that strip signal:noise is maintained above

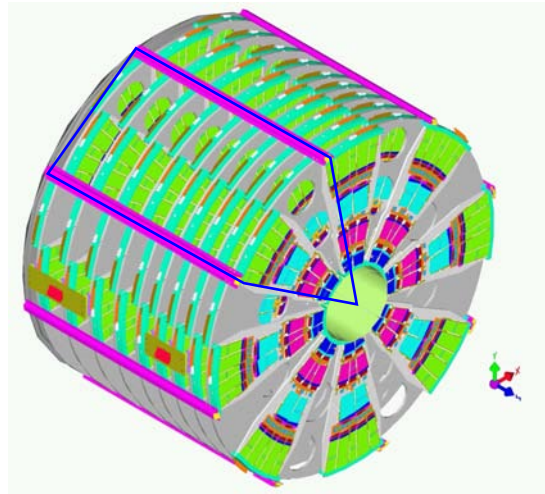


Figure 3.9: View of one tracker endcap, with the outline of a petal shown in blue. There are nine petals per wedge-shaped sector (one per TEC disk). Reprinted from Fig. 3.30 of ref. [35].

636 10 everywhere.

637 The strips are wire bonded to a front end readout chip called the APV25. The
 638 APV25 amplifies and shapes the strip signals before sending the full analog pulse
 639 information to an APVMUX, which multiplexes the output of two APV25s. Then,
 640 the electrical signal from the APVMUX is sent differentially a few centimeters to an
 641 optical driver, where it is converted to an optical signal and sent to one of the 450
 642 front end drivers (FEDs). The FEDs convert the signal back to an electrical pulse
 643 and digitize it for use in the global event assembly. As for the pixels, analog readout
 644 is used on detector so that hit reconstruction may benefit from charge sharing.

645 Clock, trigger, and control signals are sent from the front end controllers (FECs)
 646 to phase locked loop (PLL) chips on the front ends. The FECs interface to the global
 647 clock and trigger system. Four or six APV25s, an APVMUX, and a PLL chip all sit on
 648 a *hybrid*, two which one thin or two thick sensors are also affixed. The sensor-hybrid
 649 combination and its frame form a module. Figure 3.10 shows a diagram of a module,
 650 while Figure 3.11 shows a block diagram of the strip readout architecture.

651 As an example of the strip capabilities, strip hit resolution and signal:noise mea-

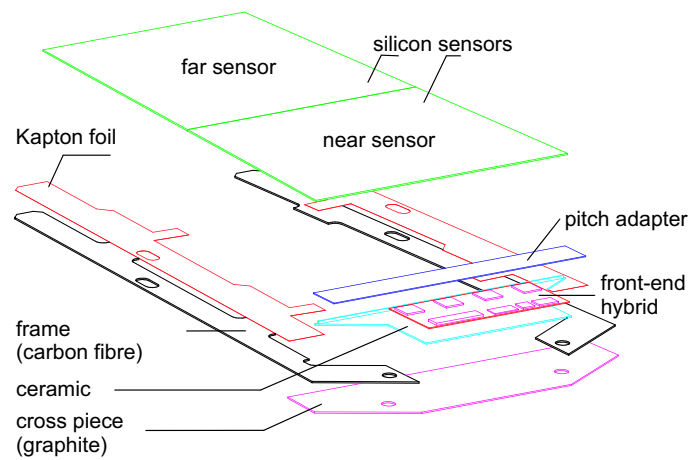


Figure 3.10: Exploded view of a strip module with two sensors. Reprinted from Fig. 3.22 of ref. [35].

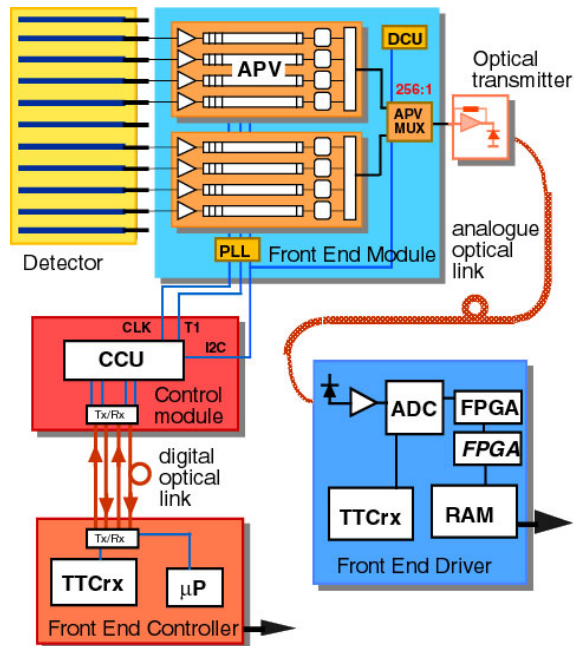


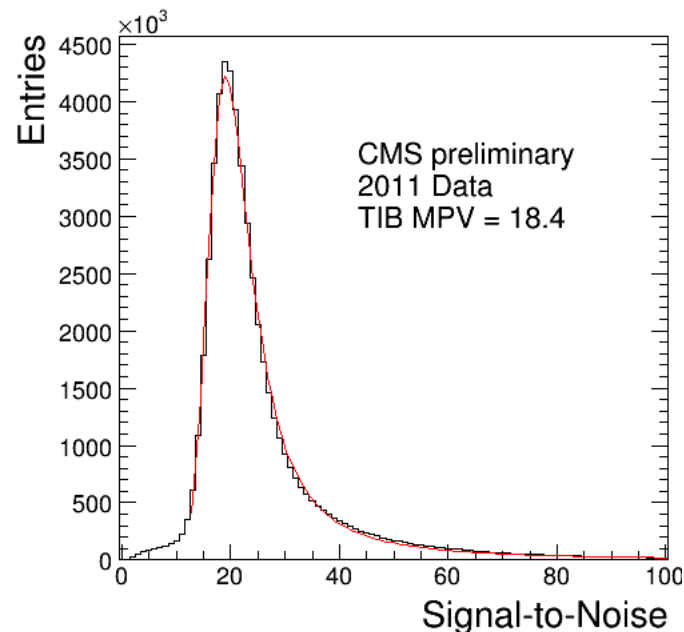
Figure 3.11: Block diagram of the strip readout architecture. Reprinted from Fig. 3.20 of ref. [35].

surements are shown in Figure 3.12. The entire pixel + strip tracker has been used successfully in the reconstruction of primary and secondary vertices, electrons, muons, tau decays, and charm and bottom hadron decays. In addition, the superior performance of the tracker over the hadronic calorimeter for low energy charged hadrons has been exploited in the the particle flow jet and \cancel{E}_T reconstruction technique (see Sec. 4.1.3). The CMS silicon strips, as well as the pixels, are well aligned and operating at close to design performance.

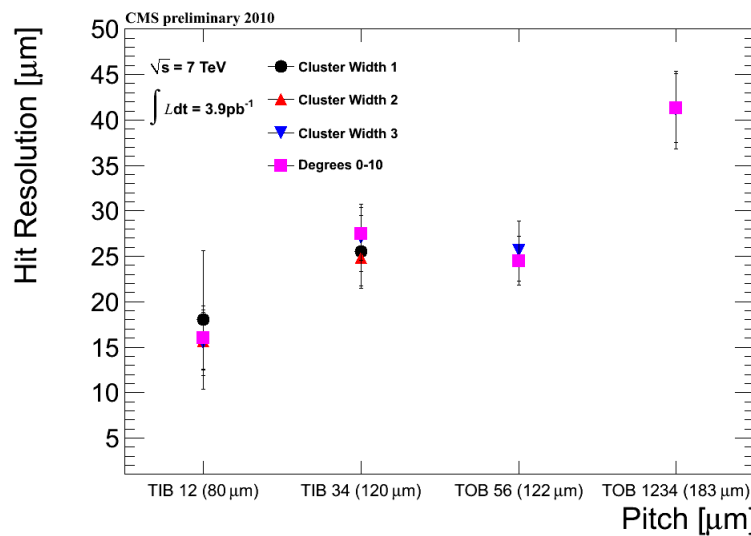
3.1.2 Electromagnetic Calorimeter

The electromagnetic calorimeter (ECAL) is composed of 68,524 lead tungstate (PbWO_4) crystals, divided into one barrel (EB) layer and two endcap (EE) disks. In EB, there are 1700 crystals per *supermodule* (SM), arranged in a 20×85 grid in $\phi \times \eta$. Two SMs are laid out end-to-end to form one row at fixed ϕ , with a total of 18 rows needed to cover the entire 2π extent in ϕ . The SMs may be operated independently. In EE, the independent unit is a wedge-shaped sector, with nine sectors covering each endcap side. The 7,324 EE crystals are divided approximately evenly between the 18 EE sectors. A two-layer preshower detector is placed in front of the EE disks, each layer consisting of a lead absorber followed by 1.9 mm pitch silicon strip detectors (the strips in the first layer are rotated 90° with respect to the second layer). The ECAL layout is shown in Figure 3.13.

The electromagnetic energy resolution can be parametrized as $(\sigma/E)^2 = (S/\sqrt{E})^2 + (N/E)^2 + (C)^2$, where S characterizes the size of photostatistical fluctuations, N characterizes the contribution from electronics noise, and C is a constant accounting for imperfect intercalibration between crystals, non-uniformity of crystal performance, and incomplete shower containment within one crystal. The design goal of the ECAL is to achieve $C = 0.5\%$. Therefore, fast, dense, and relatively radiation hard PbWO_4 was chosen as the crystal material. When a photon or electron strikes the crystal, it



(a) TIB signal:noise [42].



(b) TIB and TOB hit resolution as a function of strip pitch [43].

Figure 3.12: Strip detector performance highlights.

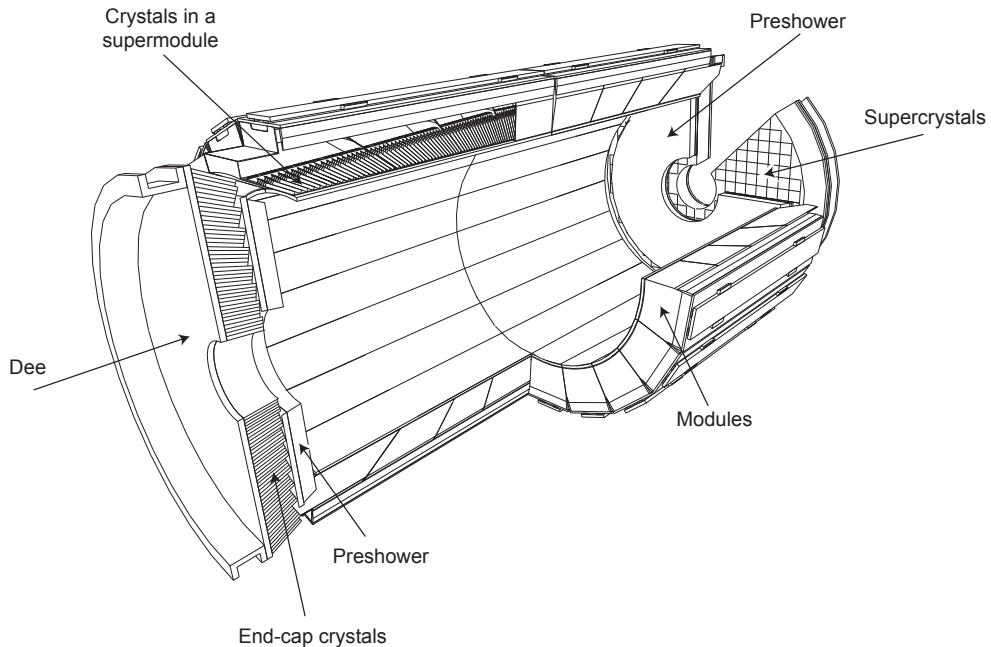


Figure 3.13: Layout of the ECAL detector. Reprinted from Fig. 4.5 of ref. [35].

678 initiates an electromagnetic (EM) shower. Due to the density, short radiation length,
 679 and small Molière radius of PbWO_4 , nearly the entirety of an EM shower can be
 680 contained in a single 23-cm long crystal with front face dimensions $2.2 \text{ cm} \times 2.2 \text{ cm}$.
 681 The crystals scintillate in the blue-green part of the spectrum, emitting $\sim 80\%$ of the
 682 scintillation light within 25 ns. Light is transmitted along the length of the crystals
 683 and collected at the rear with avalanche photodiodes (semiconductor diodes) in EB or
 684 vacuum phototriodes (conventional photomultipliers) in EE. Since the light output is
 685 low and varies with temperature, the crystals must be kept precisely at 18°C . The EB
 686 and EE crystals, which are slightly tapered to match the lateral shower development,
 687 are shown in Figure 3.14.

688 For each trigger, 10 samples, each separated by 25 ns, are read out. The 10-sample
 689 pulse is amplified and shaped by a multi-gain preamplifier (MGPA) residing on a very
 690 front end (VFE) card serving five crystals. The MGPA can switch between gains 1,
 691 6, and 12 to avoid saturation of the electronics, and affords a dynamic range up to

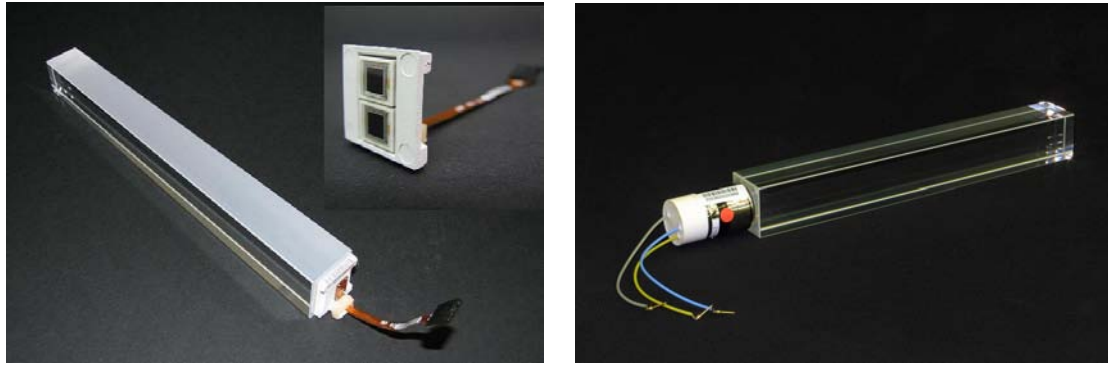


Figure 3.14: Left: EB crystal with attached APD. Right: EE crystal with attached VPT. Reprinted from Fig. 4.2 of ref. [35].

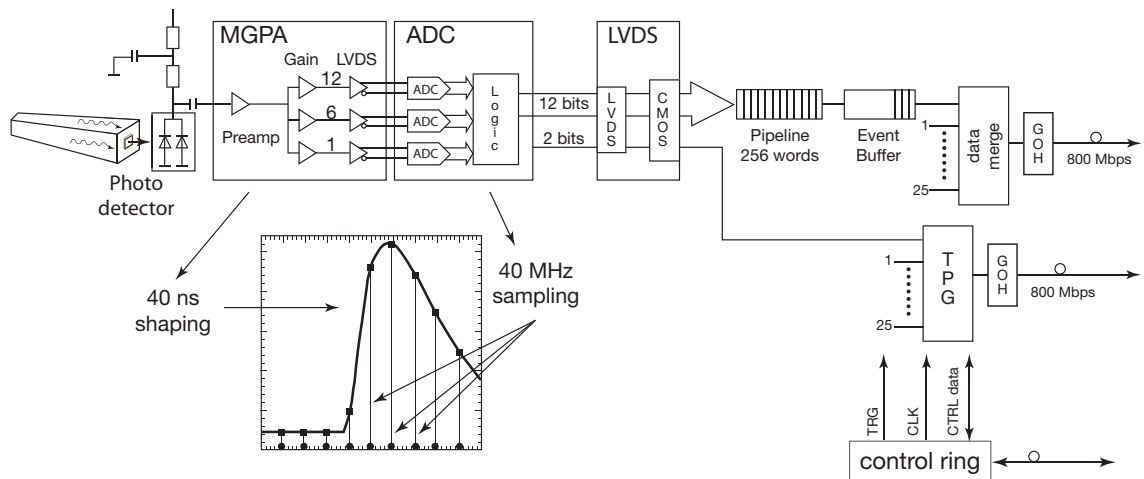


Figure 3.15: Flow chart of the crystal readout, showing the 10-sample pulse shape. Reprinted from Fig. 4.9 of ref. [35].

692 3 TeV. The samples are digitized on the VFE card, then sent to the front end (FE)
 693 card serving five VFEs. Digitized samples are buffered in the FE card until receipt
 694 of a trigger, when they are sent over an optical link to the data concentrator card
 695 (DCC) that interfaces to the global DAQ. The DCC interfaces to the *selective readout*
 696 processor, which decides whether a crystal should be read out with or without zero
 697 suppression based on its proximity to a high-energy hit. The clock is transmitted to
 698 the FE cards from the Clock and Control System (CCS) boards. A flow chart of the
 699 crystal readout is given in Figure 3.15.

At each bunch crossing, the trigger concentrator cards (TCC) of the ECAL compute *trigger primitives* from 5×5 non-overlapping transverse energy sums (in the endcaps the geometry is not always 5×5). This information, along with a special bit in EB only characterizing the transverse shower profile that is used for rejection of anomalous APD hits (see Sec. 4.1.1), is transmitted from the TCCs to the synchronization and link boards (SLBs), and then on to the global trigger system. The trigger decision is communicated to the DCCs, which request the buffered data from the front ends if the decision is affirmative.

Despite the radiation hardness of lead tungstate relative to other types of crystals, it still suffers from transparency loss due to radiation-induced lattice damage, as shown in Figure 3.16. In addition, any unforeseen change in the gains of the MGPAs and VPTs, or in the pedestal levels, will degrade the energy resolution. For this reason, a continuously running calibration system is installed with the ECAL. The system makes use of the LHC abort gaps to read out the pedestal levels, test pulses fired into the MGPAs, and laser (EB and EE) or LED (EE only) pulses fired into the crystals at regular intervals. Laser and LED events are used to compute corrections to the crystal gains for transparency loss, while the other types of calibration events serve to monitor changes in the electronics performance due to magnetic field or high voltage cycling. The mean time between transparency measurements is ~ 40 minutes. Figure 3.17 shows the architecture of the laser monitoring system.

The current ECAL energy resolution is somewhat worse than the design goal of 0.5%. An incomplete understanding of (a) the transparency loss and (b) the photon conversion and electron bremsstrahlung processes in the $\sim 1X_0$ of tracker material in front of the ECAL are the main limiting factors in improving the resolution. However, as more data accumulate, more refined models of transparency loss and EM interactions in the tracker can be built, leading to better resolution. Energy resolution vs. $|\eta|$ can be seen in Figure 3.18.

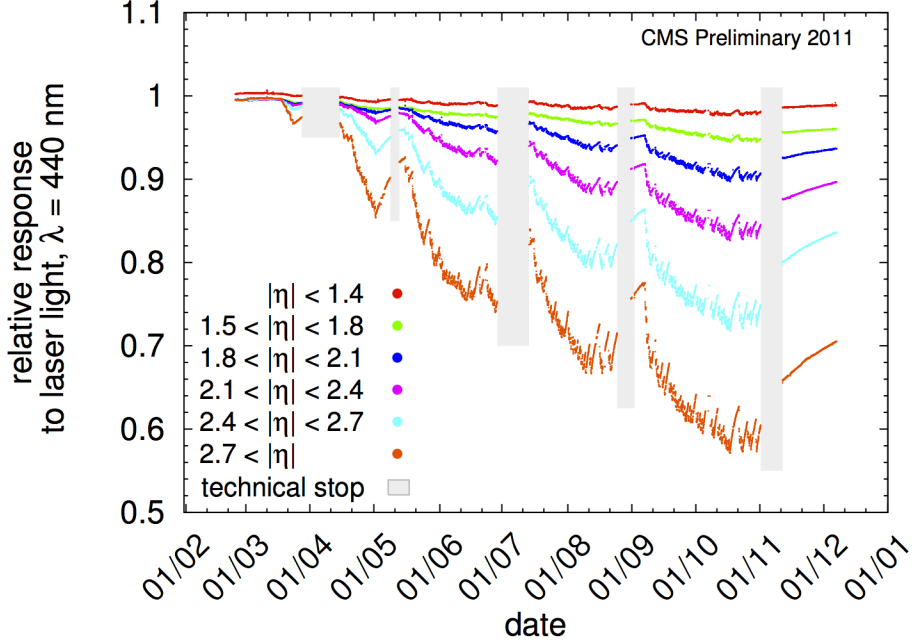


Figure 3.16: Relative response of the crystals to blue laser pulses from February 1, 2011 to January 1, 2012 [44]. Technical stops, during which the LHC is turned off for maintenance and development, are shown in gray. These periods of inactivity correspond to growth in the crystal response, as radiation damage recovery occurs.

727 The 10-sample readout coupled with the fast scintillation time of lead tungstate
 728 allows for a very precise reconstruction of the time of ECAL hits. ECAL timing is used
 729 for searches for long-lived particles that decay to photons or jets, such as long-lived
 730 neutralinos in GMSB [?]. Figure 3.19 shows the timing resolution in EE.

731 3.1.3 Hadronic Calorimeter

732 The CMS hadronic calorimeter (HCAL) has four parts: HCAL barrel (HB), HCAL
 733 endcap (HE), and HCAL outer (HO), which all utilize the same brass absorber /
 734 plastic scintillator sandwich technology; and HCAL forward (HF), which is a Čerenkov
 735 detector made of quartz fibers. A quarter longitudinal cross-sectional view of HCAL
 736 is shown in Figure 3.20. Like EB, HB is formed of 36 ϕ -wedges (18 cover 2π in positive
 737 η , 18 cover 2π in negative η). Each wedge is divided into 16 along η and four along
 738 ϕ , for a total of 64 readout towers per wedge (compare 1700 individually read out

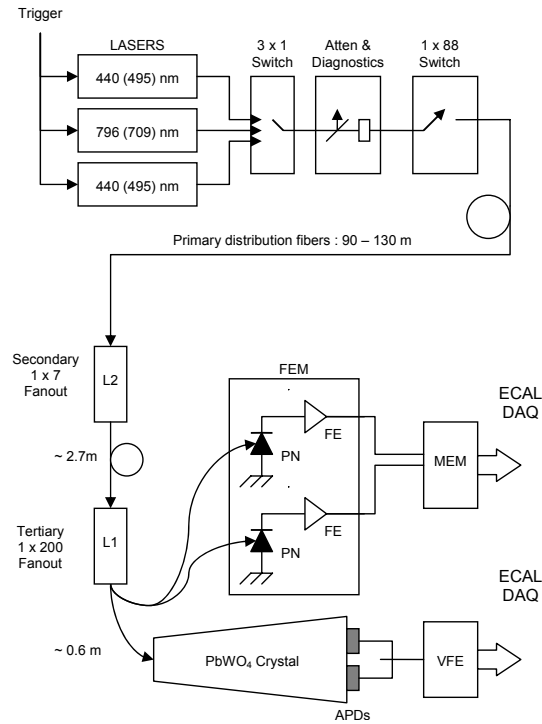


Figure 3.17: Architecture of the laser monitoring system. Reprinted from Fig. 4.16 of ref. [35].

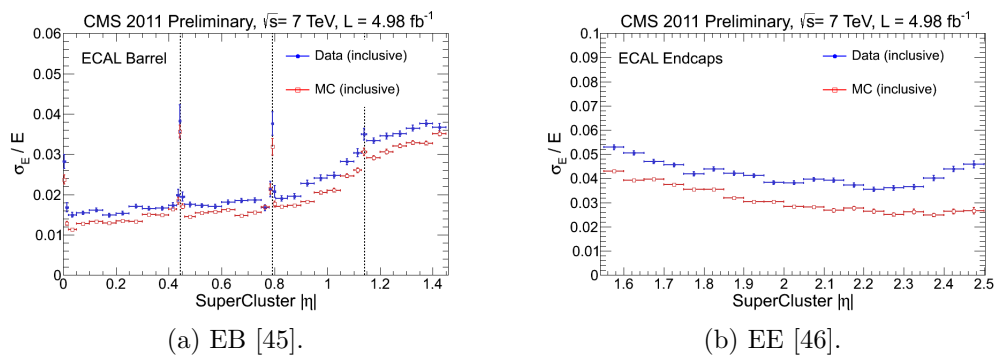


Figure 3.18: Energy resolution vs. $|\eta|$ for Z decay electrons for data (filled blue circles) and MC (empty red squares). The dotted lines show the locations of module gaps (three per SM).

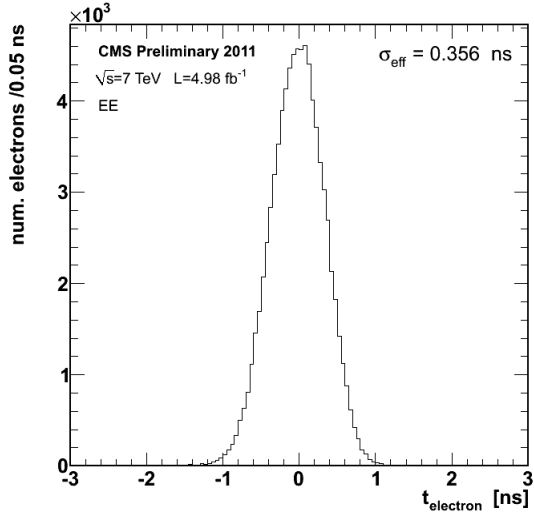


Figure 3.19: Distribution of reconstructed times of Z decay electrons in EE [47].

739 crystals per EB wedge). HE is divided into 36 ϕ -wedges containing 38 readout towers
 740 each. HO consists of five rings around HB and HE distributed symmetrically along z .
 741 There are 72 ϕ -slices per ring, with each ϕ -slice further divided into 5, 6, or 8 along
 742 z depending on ring. The HF fibers are distributed within the steel absorber. HF is
 743 divided into 18 ϕ -wedges per endcap side, each containing 24 readout towers. All HB
 744 towers have a single readout channel except for the two in each wedge at highest $|\eta|$,
 745 which are segmented into two longitudinal layers for readout. In HE, all towers have
 746 two longitudinal readout layers, except for the three rings of towers closest to the
 747 beam line, which have three. There are also two longitudinal depths of HF fibers.

748 HB, HE, and HO are all sampling calorimeters consisting of alternating layers of
 749 brass absorber and plastic scintillator. The absorber initiates the hadronic shower,
 750 and as shower particles travel through the scintillator the scintillation light is read
 751 out by wavelength-shifting (WLS) fibers connected to the scintillator tiles.² The full
 752 development of the shower is sampled by the layers of instrumented scintillator. The
 753 scintillator tiles are staggered so that there are no cracks in coverage along the direc-

²By contrast, in the ECAL, the crystal material acts as both absorber and scintillator, greatly reducing the contribution to energy resolution from sampling fluctuations.

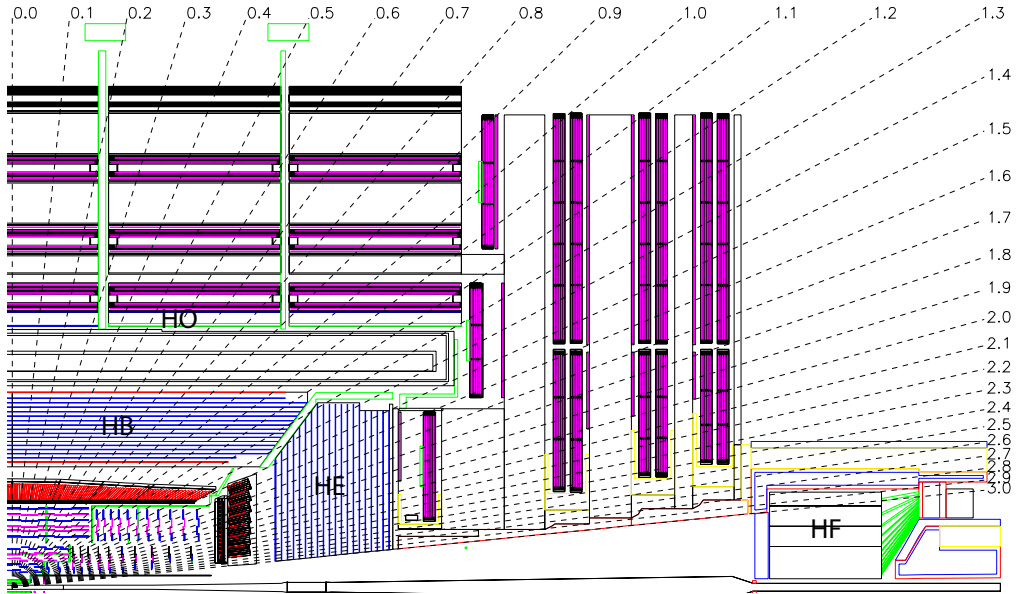


Figure 3.20: Quarter longitudinal cross-sectional view of HCAL (and muon stations in purple). Reprinted from Fig. 5.1 of ref. [35].

tion projected back to the beam spot. Light output from all tiles in a single readout tower is collected via the WLS fibers and merged into a single signal that is amplified by a hybrid photodiode (HPD). A diagram of the optical readout of HB (similar for HE and HO) is shown in Figure 3.21.

Due to the extremely harsh radiation environment near the beam line, HF is constructed of a 1.2-m thick, 1.7-m long ring of steel absorber with radiation hard quartz fibers distributed within the steel and running parallel to the beam line. Hadronic showers develop in the steel and are sampled in the quartz fibers when charged shower particles hit the the fibers and emit Čerenkov light. The light is transmitted by total internal reflection down the fibers to a photomultiplier tube (PMT), where the signals from all fibers in an HF tower are merged into one. Since only relativistic particles emit Čerenkov light in these fibers, it is mostly the EM component of the hadronic shower, consisting of neutral pions decaying to photons that interact electromagnetically with the absorber, that is sampled [48]. The charged hadrons produced in hadronic showers are typically too slow to generate Čerenkov light. Figure 3.22

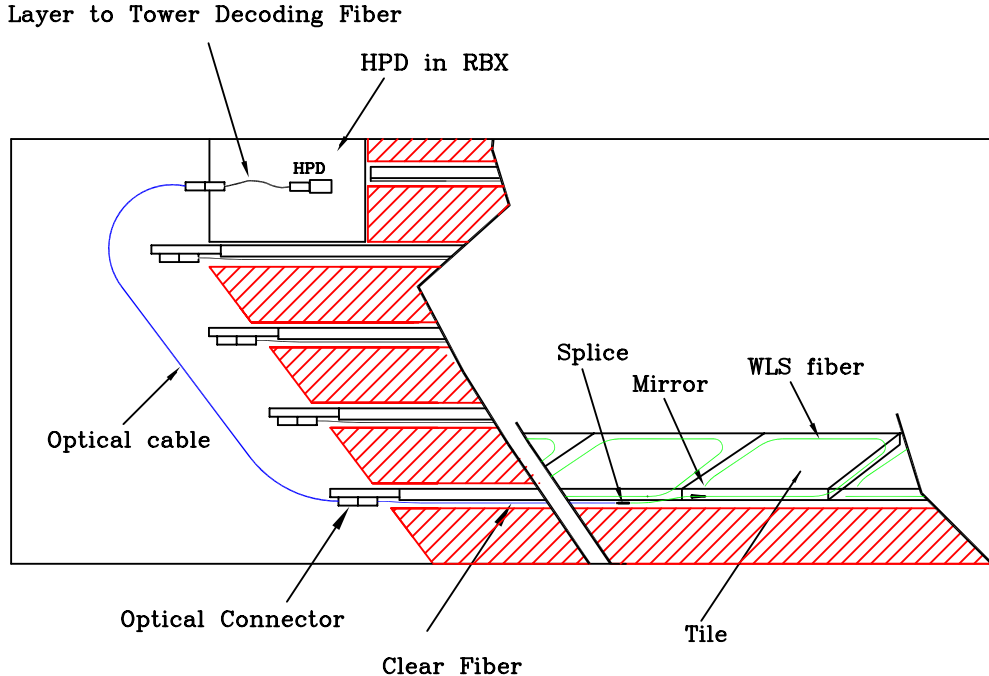


Figure 3.21: Diagram of the optical readout of HB. Reprinted from Fig. 5.7 of ref. [35].

769 shows a cross-sectional view of one side of HF.

770 Electrical signals from either HPDs (HB/HE/HO) or PMTs (HF) are digitized on
 771 the front ends by means of a fast charge-integrating ADC. The digitized signals are
 772 sent off-detector to the HCAL Trigger/Read-Out (HTR) boards, where they await a
 773 trigger decision. If the trigger is accepted, the signals are sent on to the HCAL data
 774 concentrator cards (DCCs), which interface to the global DAQ system. HCAL trigger
 775 primitives, consisting of transverse energy sums over an entire tower, are calculated
 776 in the HTR boards and sent to the global trigger system.

777 Selected HCAL performance results can be seen in Figure 3.23.

778 3.1.4 Muon System

779 Beginning at a radius of ~ 10 interaction lengths from the beam line, where all parti-
 780 cles except muons should have been stopped by the HCAL, are the muon chambers,
 781 interspersed with the iron return yoke of the CMS magnetic field. Three technologies

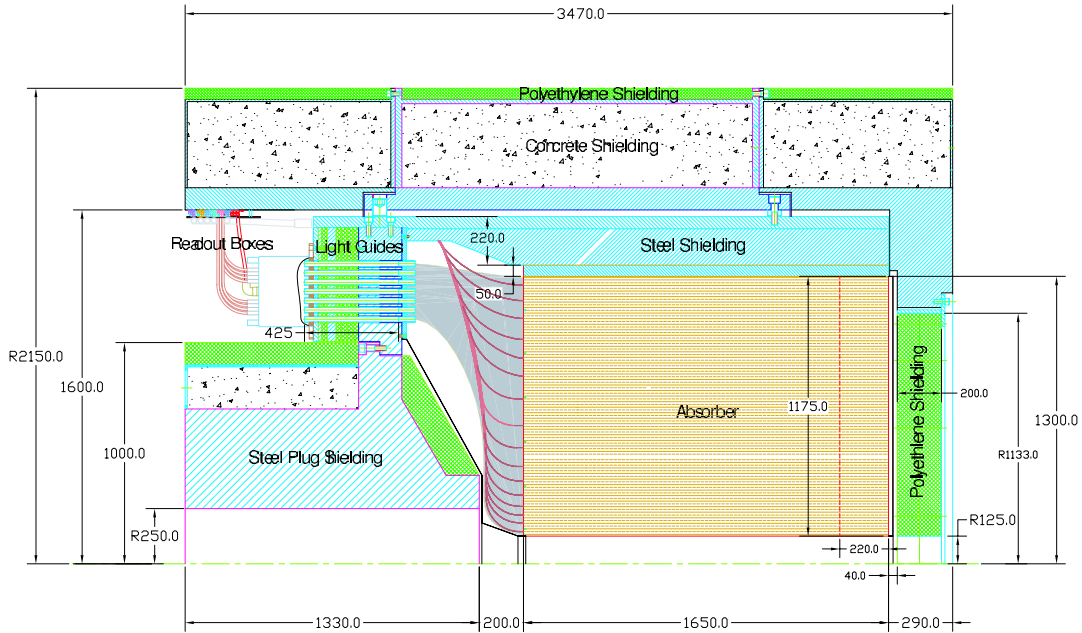
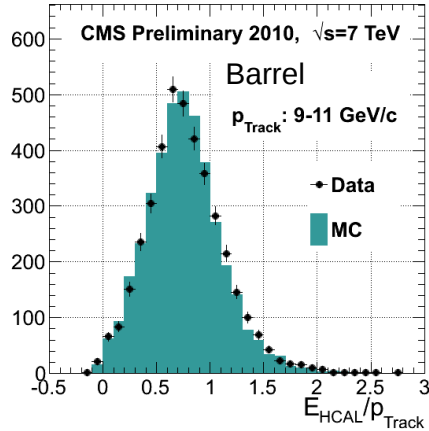


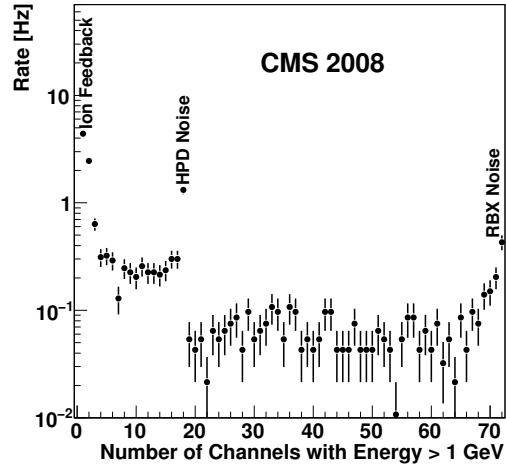
Figure 3.22: Cross-sectional view of one side of HF. The z -axis is horizontal. Reprinted from Fig. 5.28 of ref. [35].

782 are employed: drift tubes in the barrel section (MB), cathode strip chambers (CSCs)
 783 in the endcap section (ME), and resistive plate chambers (RPCs) in both sections to
 784 provide an independent trigger with superior time resolution. There are four barrel
 785 layers of stations extending out to $|\eta| = 1.2$. Each endcap consists of five disks of
 786 stations as shown in Figure 3.24b, covering $1.4 < |\eta| < 2.4$. RPCs populate the barrel
 787 and endcap muon systems alongside the DT chambers and CSCs. Since they have
 788 time resolution much better than a few ns, they are used to assign the bunch crossing
 789 of muon tracks and provide a p_T trigger with sharp turn-on.

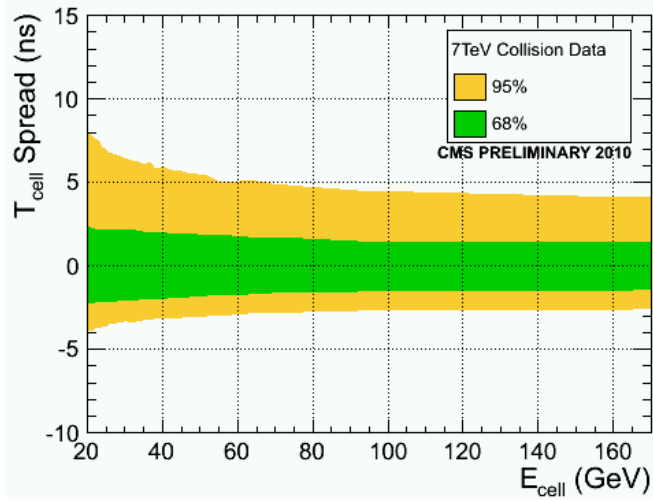
790 Each DT chamber consists of two $r \cdot \phi$ superlayers (SLs) and optionally one z
 791 SL (in all chambers except those in the fourth layer). The SLs contain four rows of
 792 drift tubes, with the rows staggered such that there are no gaps in the coverage. The
 793 $r \cdot \phi$ SLs have the tube axis parallel to the beam line, while the z SL is perpendicular
 794 to the beam line. The tubes are ~ 2.4 m in length and $13 \text{ mm} \times 42 \text{ mm}$ in cross
 795 section. Each chamber therefore records eight $r \cdot \phi$ tracking points and optionally four



(a) Data/MC comparison of HB response to charged tracks of 9-11 GeV/c momentum [49].

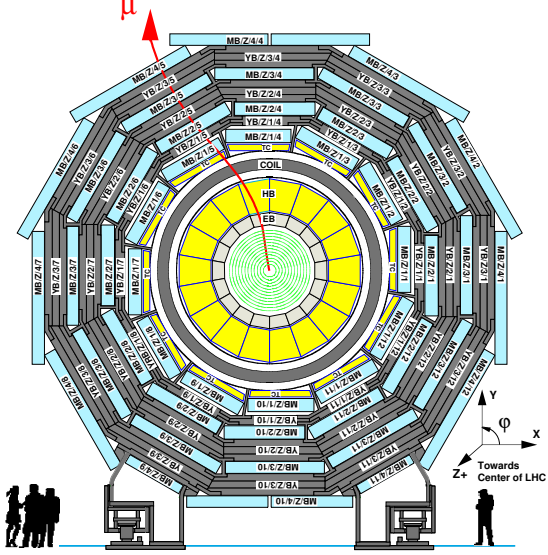


(b) Distribution of tower multiplicity, clearly showing three peaks in rate corresponding to noise sources (see Sec. 4.3) [89].

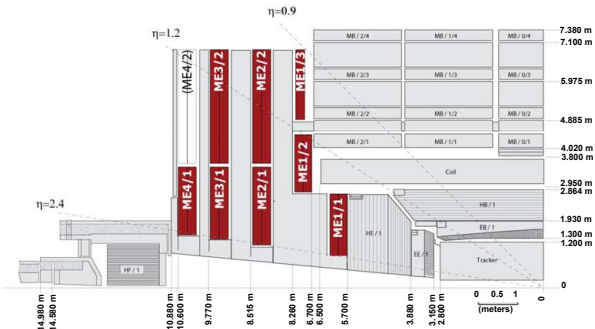


(c) Timing resolution vs. tower energy [49].

Figure 3.23: Selected HCAL performance results.



(a) One of the five wheels of MB, showing the four layers of muon stations. The five wheels are spaced symmetrically in z about $z = 0$. As a muon traverses the muon detectors, its curvature in the transverse plane changes direction and magnitude due to the magnetic field in the return yoke, which is of opposite sign and reduced strength relative to the field within the solenoid volume. Reprinted from Fig. 7.3 of ref. [35].



(b) Quarter longitudinal cross section of CMS highlighting the location of the ME disks. Reprinted from Fig. 7.47 of ref. [35].

Figure 3.24: View of the MB and ME layout in CMS.

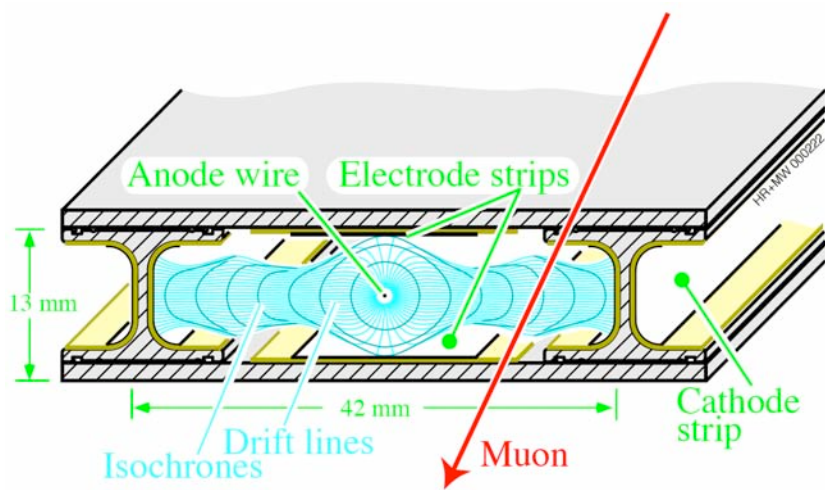


Figure 3.25: Electric field lines within a drift tube as well as the contours of equal drift time. Reprinted from Fig. 7.5 of ref. [35].

796 z tracking points. The tubes are filled with an 85%Ar + 15% CO₂ gas mixture. An
 797 anode wire at 3600 V runs the length of the tube, while the walls are covered with
 798 electrodes held at 1800 V or -1200 V depending on wall. When a muon passes through
 799 the tube, it ionizes the gas atoms. The liberated electrons drift along the electric field
 800 lines created by the electrodes to the anode, which is read out. Figure 3.25 shows
 801 the electric field lines within a drift tube as well as the contours of equal drift time.
 802 The maximum drift time is 380 ns.

803 CSCs consist of alternating layers of cathode strips (four planes oriented along r)
 804 and anode wires (three planes oriented along ϕ). A 40%Ar + 50%CO₂ + 10%CF₄ gas
 805 mixture fills the space between two successive planes, forming six gas gaps. When a
 806 muon ionizes the gas atoms, the positive ions drift toward the anode and are read
 807 out to provide a measurement of r , just as in the DTs. However, an image charge is
 808 induced on the cathode strips, which is also read out to provide a measurement of ϕ .
 809 The wires are spaced 3.2 mm apart. The cathode strips have pitch varying from 8.4
 810 mm at the end closest to the beam line to 16 mm at the other end, and are spaced
 811 0.5 mm apart. A trapezoidal CSC is shown in Figure 3.26.

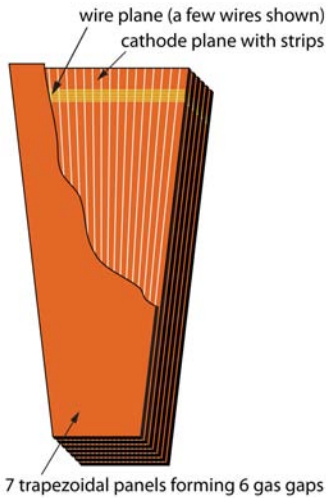


Figure 3.26: CSC wedge, showing the cathode and wire planes. Reprinted from Fig. 7.49 of ref. [35].

812 Track stubs from the muon system are combined with tracks from the tracking
 813 system to form more precise muon tracks than either system could form alone, as
 814 shown in Figure 3.27. This leads to extremely good di-muon invariant mass resolution
 815 (Figure 3.28) over a large p_T range.

816 **3.2 Triggering, Data Acquisition, and Data Trans-** 817 **fer**

818 **3.2.1 Level 1 and High Level Trigger Systems**

819 The Level-1 (L1) trigger system, which encompasses dedicated hardware processors
 820 to construct trigger objects (typically high p_T jets, electrons, photons, taus, and
 821 muons) out of the calorimeter and muon hits, distributes a L1 accept or reject to all
 822 subdetectors at the LHC bunch crossing frequency of 40 MHz. Further data filtering
 823 is performed by the High Level Trigger (HLT) system, a farm of ~ 1000 commercially
 824 available processors running a slimmed down version of the CMS event reconstruction

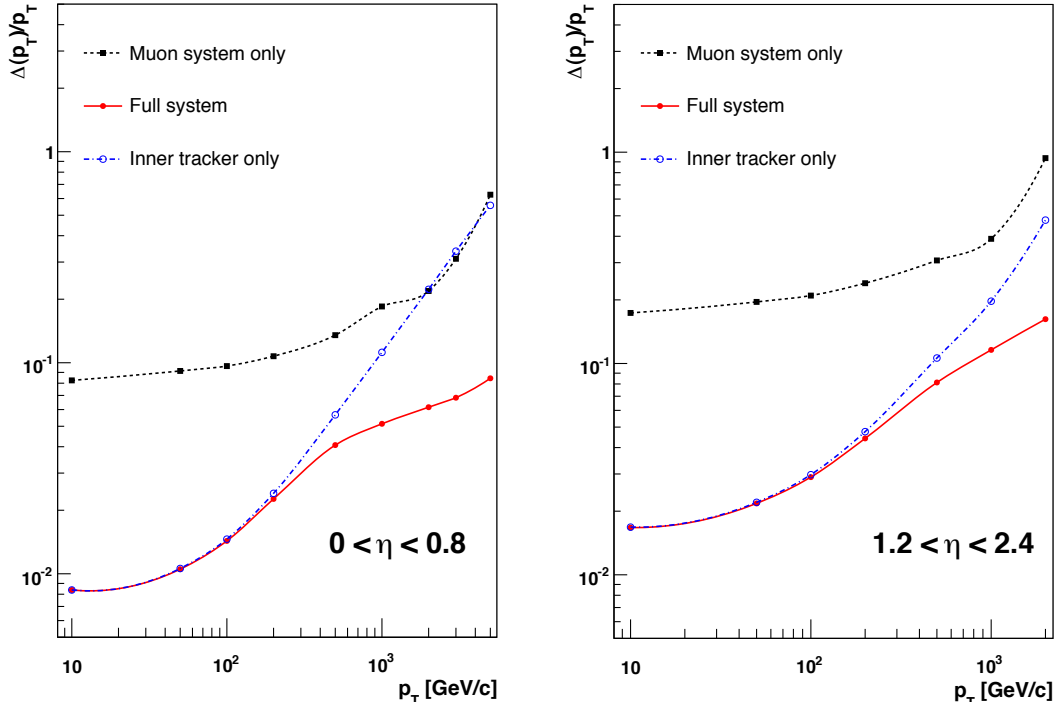


Figure 3.27: Muon p_T resolution as a function of muon p_T for tracker information only (blue), muon information only (black), and both tracker and muon information combined (red). Reprinted from Fig. 1.2 of ref. [35].

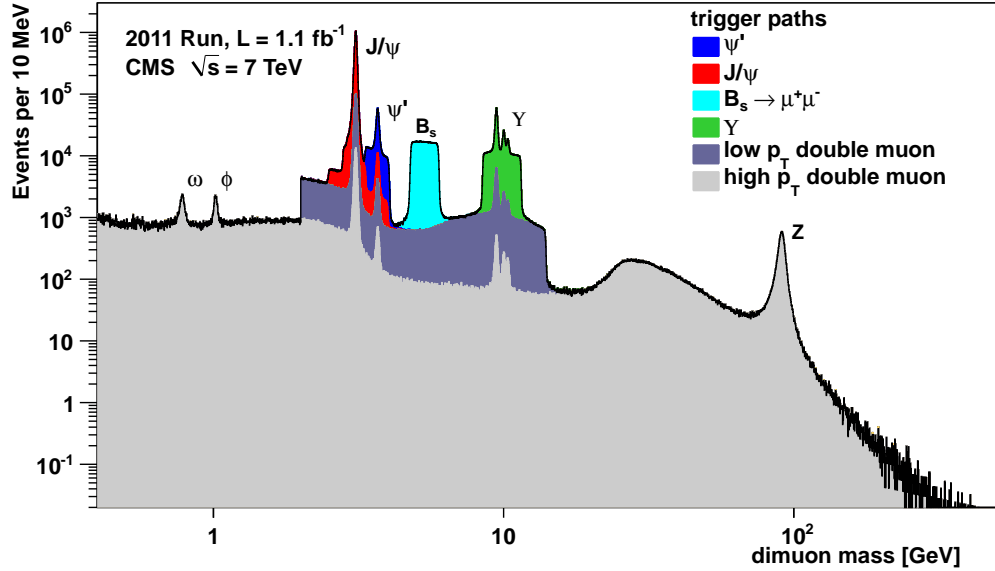


Figure 3.28: Di-muon invariant mass spectrum broken down by trigger path [50]. The light(dark) gray regions show the contribution from high- p_T (low- p_T) di-muon triggers. Note that no $B_s \rightarrow \mu^+\mu^-$ decays have been observed [51]; the light blue region just shows the amount of triggers dedicated to the $B_s \rightarrow \mu^+\mu^-$ search.

825 software CMSSW. The data rate received by the HLT is ~ 100 kHz; the output rate of
 826 events permanently written to disk is ~ 100 Hz. An L1 trigger *latency* (time between
 827 the collision and the distribution of the L1 decision to the subdetectors) of $3.2\ \mu\text{s}$ is
 828 achieved via the use of fast electronics and sufficiently deep buffers to pipeline trigger
 829 primitives waiting to be analyzed. This latency corresponds to the length of the LHC
 830 abort gap, so in principle CMS may be operated with zero *dead time* (during which
 831 LHC bunches are missed because the L1 system is blocked while processing other
 832 triggers).

833 At the bottom, the L1 trigger consists of trigger primitive generators (TPGs) in
 834 the calorimeter and muon systems that send E_T sums or muon track stubs to the
 835 regional calorimeter trigger (RCT) or muon track finders, respectively. The RCT,
 836 DT track finder (DTTF), and CSC track finder (CSCTF) sort and rank the regional
 837 trigger primitives based on p_T and quality. The ranked RCT candidates and muon
 838 track stubs are sent to the global calorimeter trigger (GMT) and global muon trigger
 839 (GMT), respectively, where high-level objects like isolated and non-isolated muons
 840 and EM candidates, jets, taus, and \cancel{E}_T are constructed from all the regional inputs
 841 and ranked. Calorimeter isolation sums for muons are also sent from the RCT to
 842 the GMT. The highest ranked global objects are sent to the global trigger (GT),
 843 which sits at the top of the L1 trigger. The GT issues the final L1 accept or reject to
 844 all subdetectors based on a comparison of the GMT and GCT candidates with the
 845 requirements of its programmed trigger menu. A block diagram of the L1 trigger is
 846 shown in Figure 3.29.

847 A region in the RCT consists of a matrix of 4×4 trigger towers. A trigger tower
 848 in EB/HB is one HCAL tower + the 5×5 matrix of ECAL crystals in front of it;
 849 in EE/HE the idea is similar but the counting of crystals and HE towers is slightly
 850 more complicated. An EM RCT candidate is built around a high E_T seed tower.
 851 The E_T of the candidate is the sum of the tower E_T and the E_T of its highest- E_T

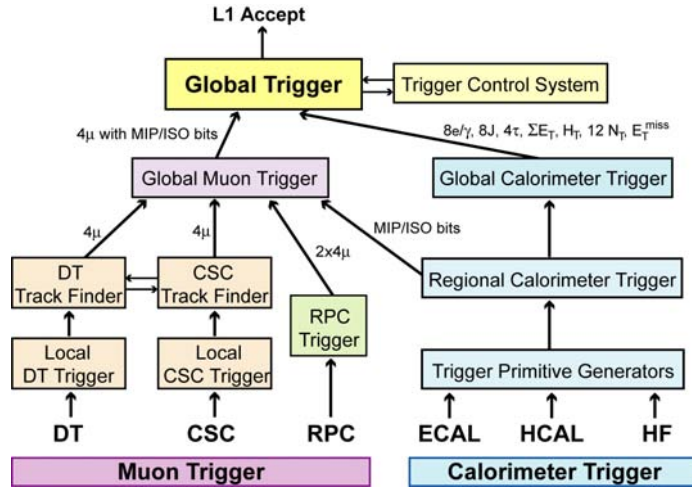


Figure 3.29: Block diagram of the L1 trigger. Reprinted from Fig. 8.1 of ref. [35].

852 broad side neighbor (see Figure 3.30 for a definition of the broad side neighbors). Two
 853 isolation criteria are defined based on (a) the ratio of the EM energy to the HCAL
 854 energy in the tower and (b) the shower shape. For a non-isolated EM candidate, the
 855 highest- E_T broad side neighboring tower must pass these two isolation criteria; for
 856 an isolated EM candidate, all eight neighboring towers must the criteria, and there
 857 must also be at least one quiet corner with the E_T of all five towers in the corner
 858 below some threshold (see Fig. 3.30). The process is repeated until four isolated and
 859 four non-isolated EM candidates are found, starting with the highest- E_T tower in the
 860 region and moving down in tower E_T . An RCT region is flagged as consistent with
 861 tau decay only if the pattern of tower transverse energy sums defines at most a 2×2
 862 matrix of energetic towers within the 4×4 RCT region.

863 From the tower transverse energy sums, eight EM candidates, and tau flag received
 864 from each RCT, the GCT computes the total E_T in the calorimeter (and the total E_T
 865 above some programmable threshold, called H_T), and the \cancel{E}_T . It also classifies the
 866 towers into jets and determines the globally highest ranked isolated and non-isolated
 867 EM candidates. The jet finding uses a clustering algorithm based on the energy of a
 868 sub-cluster with respect to its neighbors [52]. Jets are classified as tau decays if all

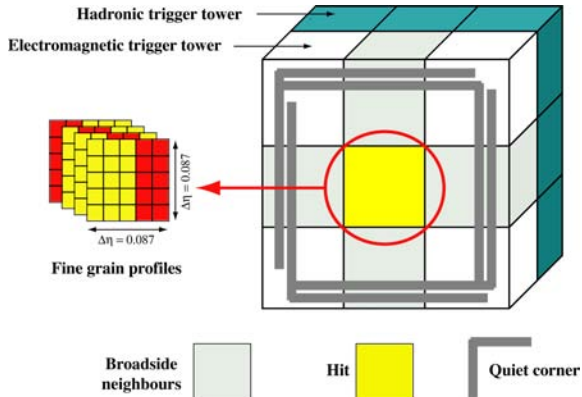


Figure 3.30: Geometry of an EM RCT candidate. Reprinted from Fig. 8.2 of ref. [35].

of the RCT regions participating in the jet clustering had energy patterns consistent with tau decay. Counts of jets above 12 different programmable E_T thresholds are calculated. The jet counts, energy sums, \mathcal{E}_T , and highest ranked EM candidates are sent to the GT, where the final L1 decision is taken and transmitted to the subdetectors. The GT can execute a maximum of 128 trigger algorithms in parallel. If any one of these algorithms yields an accept, the event is accepted, and all trigger information is sent on to the HLT for further filtering. The double-photon HLT paths used in this analysis (see Sec. 4.2) require isolated L1 seeds (i.e. EM candidates built by the RCT) with $E_T > 12$ or 20 GeV, depending on path.

No muon triggers are used in the two-photon analysis. A description of the muon trigger system can be found in ref.[35].

3.2.2 Data Acquisition System

The CMS data acquisition (DAQ) system takes event fragments (calorimeter hits, track hits, etc.) from each of the 626 subdetector front end drivers (FEDs), assembles them into a data structure representing the full event, and sends the event on to the HLT for further filtering. The DAQ must operate at an input rate of ~ 100 GB/s, corresponding to an input rate from the L1 trigger of ~ 100 kHz. To facilitate

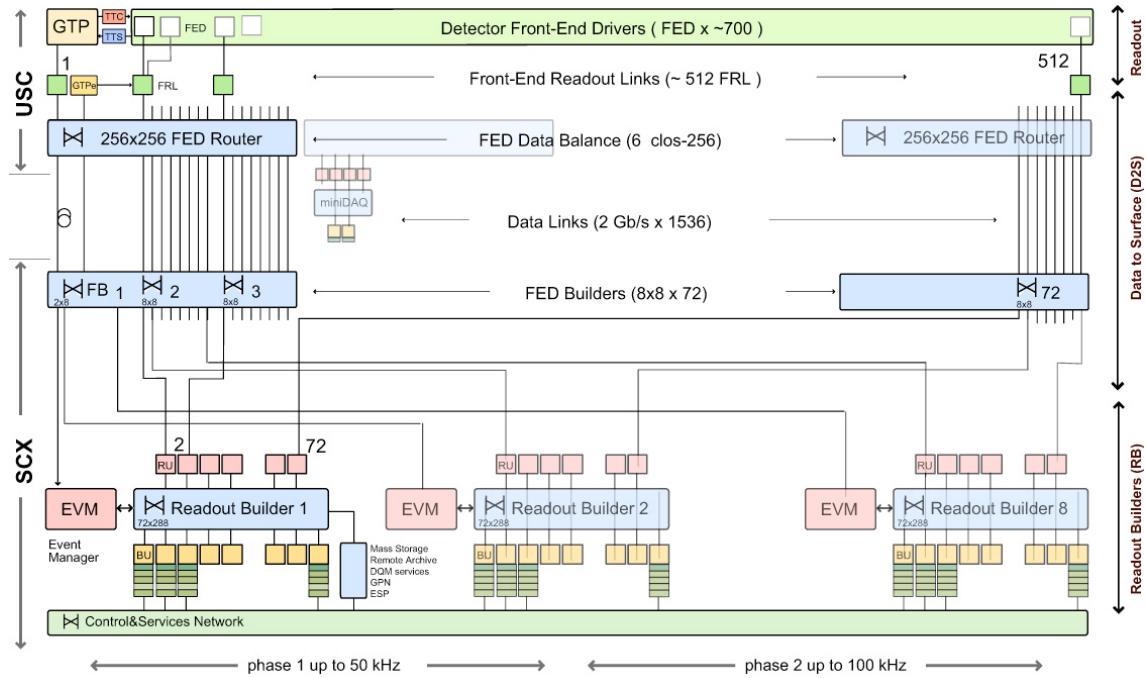


Figure 3.31: Diagram of the DAQ system. The identical event builder systems, shown as inputs and outputs to the boxes labeled “Readout Builder 1”, “Readout Builder 2”, etc., represent the eight slices. Within one slice, data can flow from the detector front ends to the readout systems to the builder network (which assembles the event fragments) to the filter systems (HLT) independently of the other slices. Reprinted from Fig. 9.8 of ref. [35].

expansion of the system as the need arises, the DAQ is composed of eight nearly independent slices. Each slice functions as a smaller version of the whole DAQ that can handle an input event rate up to ~ 12.5 kHz. A diagram of the DAQ system, showing schematically the eight slices, is given in Figure 3.31.

Data from the front ends is collected by the FEDs and pushed to the front end readout links (FRLs), which may take inputs from up to two FEDs simultaneously. The FRLs check for transmission errors, generate event fragments with size ~ 2 kB, buffer the fragments in 64 kB memories, and finally send them to the FED builders. The FEDs, FRLs, and FED builders are located in the underground control room. The 72 FED builders each construct one ~ 16 kB *super-fragment* from the input event fragments, then send the super-fragment on to a readout unit (RU) located in

897 the surface control room ~ 80 m away. Super-fragments belonging to the same event
 898 are sent to RUs in the same DAQ slice. There are 72 RUs per readout builder, one
 899 for each super-fragment of an event, with each DAQ slice built around one readout
 900 builder (see Fig. 3.31). Each readout builder hosts a number of builder units (BUs)
 901 that perform the final integration of super-fragments into complete events.

902 Resource brokers (RBs) in the HLT filter farm request complete events from the
 903 BUs and distribute those events to the filter units (FUs) for HLT selection. If an
 904 event passes any one of the HLT paths in the predefined menu, it is sent back to
 905 the RB for transfer to the storage manager (SM). The SM nodes transfer accepted
 906 events to the CERN Tier-0 prompt reconstruction facility for unpacking of the raw
 907 data into ROOT [53] files that can be accessed by physicists wishing analyze the data.
 908 The lag time between recording of an event in the DAQ and availability of the fully
 909 reconstructed event for analysis is typically 48 hours.

910 If the buffers of the upstream DAQ elements (the filter farm, readout builders,
 911 FED builders, or FRLs) are full, those elements will not request new events from
 912 downstream. This can lead to a buildup of events in the downstream element buffers,
 913 *back-pressuring* all the way down to the FEDs themselves. The CMS trigger throttling
 914 system (TTS) consists of dedicated lines between the FEDs and the GT for the
 915 purpose of sending predefined signals to the GT about the state of the FED buffers.
 916 If the buffer of a particular FED is getting full, it can alert the GT to reduce the
 917 trigger rate so as to prevent FED buffer overflows and loss of time synchronization
 918 between event fragments. The TTS latency is $\sim 1\mu\text{s}$. Causes of back-pressure (hence
 919 dead time) include: problems with the FED electronics (in this case, the upstream
 920 elements request events but the FEDs have trouble sending them), increases in the
 921 L1 accept rate (perhaps due to a noisy detector channel) beyond what the upstream
 922 DAQ elements can handle, increases in the event size due to high pileup or a poor
 923 quality beam that scrapes against the beam pipe, failures of the DAQ transmission

924 lines or DAQ hardware such that events are not requested from the FEDs fast enough,
 925 or bottlenecks at the SM nodes or filter farm due to hardware failures or large event
 926 sizes.

927 All components of the DAQ, from the FEDs up to the SMs, are controlled by
 928 cross-platform DAQ (XDAQ) [54] processes, or *executives*. The Simple Object Access
 929 Protocol (SOAP) [55] protocol is used to transmit control and monitoring data be-
 930 tween XDAQ-enabled devices and to the end user, who can view the running of a
 931 XDAQ executive via a Web interface called HyperDAQ [56]. The Run Control and
 932 Monitoring System (RCMS) handles the configuration and control of all XDAQ exec-
 933 utives via a hierarchical structure. At the top of the hierarchy is the Level-0 *function*
 934 *manager* (FM), controlling the Level-1 sub-detector FMs, which in turn control their
 935 Level-2 system-specific XDAQ executives. The central DAQ and L1 trigger each have
 936 their own Level-1 FM. A unit of data acquisition, called a *run*, may be configured,
 937 started, and stopped by an end user interacting with the RCMS Web interface.

938 3.2.3 Data Processing and Transfer to Computing Centers

939 Data leaving the filter farm are grouped into datasets based on HLT path, i.e. there
 940 are different datasets for events passing diphoton triggers, jet triggers, muon + elec-
 941 tron triggers, etc. At the Tier-0 facility, the datasets are go through three levels of
 942 processing to create three *data tiers*. The first layer produces RAW data by unpack-
 943 ing the detector byte streams sent from the DAQ and L1 trigger into data structures
 944 holding the ADC counts recorded for each channel of the detector, digitized trigger
 945 primitives, and the L1 decision. A single event has ~ 1.5 MB of RAW data. The next
 946 layer of processing is the reconstruction, which forms channel energies in GeV, ap-
 947 plies calibrations, and creates high-level objects like photons, electrons, muons, taus,
 948 jets, E_T , and charged tracks. The RECO data tier occupies ~ 0.5 MB per event.
 949 Finally, analysis object data (AOD) is a subset of the RECO data, comprising the

950 high-level objects but usually excluding the individual channel hit information if it is
951 not associated to a physics object. This tier occupies ~ 0.1 MB per event. One copy
952 of the RAW data is stored permanently at CERN and another copy is distributed
953 amongst the Tier-1 facilities (see below) for permanent storage. Changes in the re-
954 construction algorithms periodically require reprocessing of the RAW data to form a
955 new RECO tier. In general, only the AOD tier is available to physicists wishing to
956 perform analyses due to the smaller size and faster replication and transfer time of
957 AOD with respect to RAW or RECO.

958 There are three tiers of computing and data storage sites within the Worldwide
959 LHC Computing Grid (WLCG) [57]. The tier closest to CMS is Tier-0, which is
960 located at CERN and performs archiving of the RAW data, prompt reconstruction
961 of the data within ~ 48 hours of its being collected, and transferral of copies of the
962 RECO datasets to Tier-1 facilities. There are a few Tier-1 centers worldwide, hosted
963 by national computing facilities and laboratories. They store parts of the RAW dataset
964 and copies of the RECO datasets, participate in subsequent reconstruction passes
965 after the prompt reconstruction at Tier-0, and ship AOD datasets upon request to the
966 Tier-2 centers. Analysts interact primarily with the Tier-2 centers, which store AOD
967 datasets and run batch processing queues for running analysis jobs over the datasets.
968 Different layers of WLCG software control data transfer between sites, data storage,
969 and batch processing. A diagram of the WLCG tier system is given in Figure 3.32.

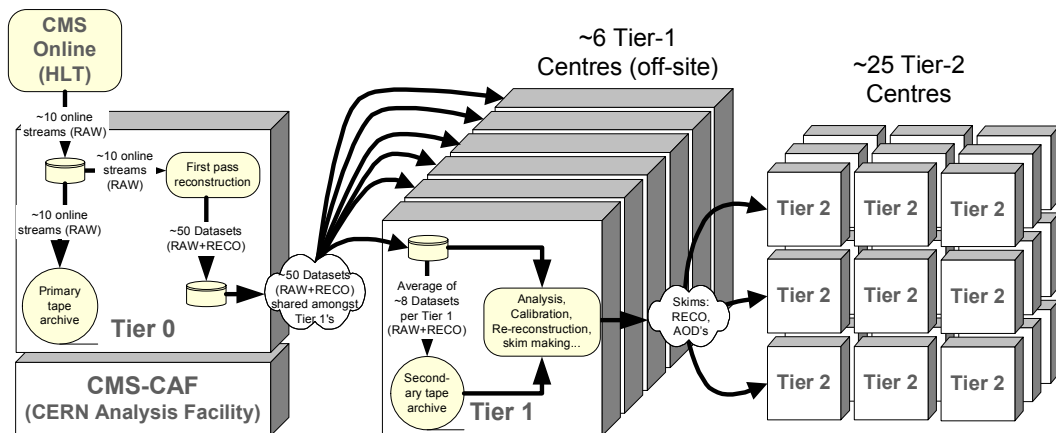


Figure 3.32: Diagram of the WLCG tier system showing data archival and reconstruction at each tier along with data transfer between tiers. Reprinted from Fig. 11.2 of ref. [35].

970 **Chapter 4**

971 **Event Selection**

972 In keeping with the phenomenology described in Sec. 1.5, the candidate GGM events
973 selected in this search consist of two high- E_T photons and a significant momentum
974 imbalance transverse to the beam, indicating the production of an escaping gravitino.
975 This momentum imbalance is usually referred to as *missing transverse energy* and is
976 denoted by the symbol \cancel{E}_T .

977 However, in order to use real CMS data (as opposed to simulation) to derive pre-
978 dictions for the backgrounds to the search, *control samples* distinct from the *candidate*
979 two-photon sample must be collected. These samples consist of different numerical
980 combinations of photons, electrons, and jets, and are explained in more detail in
981 Chapter 5. Since this search is performed in the high- \cancel{E}_T tail of the \cancel{E}_T distribution,
982 where adequate detector simulation is very difficult, it is advantageous to use *data-
983 driven* background estimates, which capture the true detector response, over numbers
984 derived from simulation.

985 In the following sections, the reconstruction of photons, electrons, jets, and \cancel{E}_T
986 is explained. Sec. 4.1 begins with an explanation of the high level reconstruction.
987 It is followed by Sec. 4.2, which describes the triggers used to collect the candidate
988 and control samples. Sec. 4.3 describes event cleaning cuts that are applied to the

989 candidate and control samples. Finally, the chapter concludes with a measurement of
990 the photon identification efficiency in Sec. 4.4.

991 4.1 Object Reconstruction

992 This section describes the *offline* object reconstruction, i.e. the reconstruction of par-
993 ticle objects from events that have already been triggered and written to permanent
994 storage, as opposed to the building of trigger objects explained in Secs. 3.2.1 and 4.2.

995 4.1.1 Photons

996 Uncalibrated EB/EE Hits

997 Photon reconstruction begins with the ADC count value for each of the 10 recorded
998 time samples per ECAL crystal per trigger. To construct an *uncalibrated hit*, the
999 gain (1, 6, or 12; see Sec. 3.1.2) of each sample is determined and the ADC count
1000 value scaled appropriately. The pedestal is estimated from the average of the first
1001 three samples, which, for a properly timed in hit, should contain no signal. This
1002 pedestal value is subtracted from the rest of the samples. Finally, the amplitude of the
1003 pulse is reconstructed using a predetermined weight for each sample [58]. The weights
1004 correspond to the pulse shape expected from the MGPA and shaping circuit response.
1005 The time of the hit is also reconstructed using the ratios between neighboring time
1006 samples [59]. A typical ECAL channel pulse shape is shown in Figure 4.1.

1007 Calibrated EB/EE Hits

1008 In the next phase of the photon reconstruction, calibrations are applied to the un-
1009 calibrated hits to form *calibrated hits* with energy measured in GeV. Channels are
1010 excluded from seeding calibrated hits if

- 1011 • they are excessively noisy,

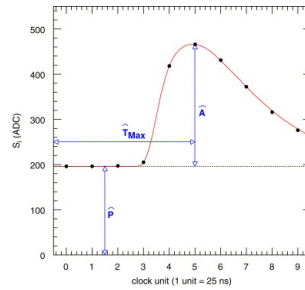


Figure 4.1: Typical ECAL channel pulse shape. \hat{P} is the pedestal value, \hat{A} is the pulse amplitude, and \hat{T}_{\max} is the hit time. The red line is the assumed pulse shape from which the weights are derived. Reprinted from ref. [58].

- 1012 • they are stuck in fixed gain (i.e. the MGPA gain does not change properly to
- 1013 avoid saturation),
- 1014 • they are totally dead,
- 1015 • they have one or more neighboring dead channels, or
- 1016 • they do not have good trigger primitives (i.e. trigger primitive is missing, satu-
- 1017 rated, or *spike-like*).

Added

1018 *ECAL spikes* are hits in which low energy protons and heavy ions from jets ionize this
 1019 in the sensitive volume of the EB APD, causing the APD to register a fake large- para-
 1020 amplitude hit. Because they are not the result of a real electromagnetic shower, spikes graph
 1021 tend to be isolated. They may also appear to arrive early or late with respect to the and the
 1022 nominal bunch crossing. Most spikes are reconstructed with a hit time ~ 10 ns earlier next
 1023 than real EM hits because unlike real hits, whose pulse shapes include the time about
 1024 constant associated with crystal scintillation, the reconstructed spikes only involve spikes
 1025 the rise time of the electronics. There also is a long tail of late arriving spikes due to
 1026 slow neutrons from jets [60].

1027 Because of their particular timing and topological characteristics, cuts have been
 1028 developed to effectively identify and reject spike-like hits. This analysis utilizes both
 1029 the “Swiss cross” cut $1 - E_4/E_1 > 0.95$, where E_1 is the energy of the spike candidate

1030 crystal and E_4 is the sum of the energies in the four crystals whose edges are parallel to
 1031 the four edges of the spike candidate crystal, and a timing cut $t \geq 3$ ns, to flag spikes.
 1032 More information about these cuts can be found in ref. [60]. A simpler algorithm
 1033 using the fine grain veto bit of the L1 TPG is used to reject spikes at the trigger level
 1034 **[insert citation]**.

1035 In addition to the trigger primitives, no uncalibrated hits that are spike-like are eli-
 1036 gible for calibration. The calibrations applied are crystal transparency loss corrections
 1037 measured continuously by the laser/LED system, energy intercalibrations (relative en-
 1038 ergy calibration between crystals), absolute scale calibrations between ADC counts
 1039 and GeV,¹ and time intercalibrations (relative time calibration between crystals).

1040 The ECAL crystals were pre-calibrated before installation in CMS using labora-
 1041 tory light yield and photodetector gain measurements [62]. In addition, some EB and
 1042 EE crystals were intercalibrated using test beams [63], and all EB crystals were inter-
 1043 calibrated with cosmic ray muons [64]. EE precalibrations were validated with LHC
 1044 *splash events* in 2009 [64, 65], in which the beam was dumped onto a collimator ap-
 1045 proximately 150 meters upstream of CMS, causing a spray of muons to enter CMS at
 1046 one endcap and exit at the other. Splash events were also used to derive time intercal-
 1047 ibration constants. Before colliding beam operations commenced, the intercalibration
 1048 precision was estimated to be 0.5%-2.2% in EB and 1%-5% in EE [66].

1049 Three calibration methods were employed once colliding beam operations began:

- 1050 • ϕ symmetry relative calibration between crystals, exploiting the azimuthal sym-
 1051 metry of CMS
- 1052 • π^0 and η relative calibration between crystals, using the diphoton decays of
 1053 these particles

¹The ADC-GeV scale factors (one for EB and one for EE) are defined such that the sum of fully calibrated and scaled hits in a particular 5×5 cluster of crystals (plus the associated energy deposited in ES) is 50 GeV for a 50 GeV incident unconverted photon [61].

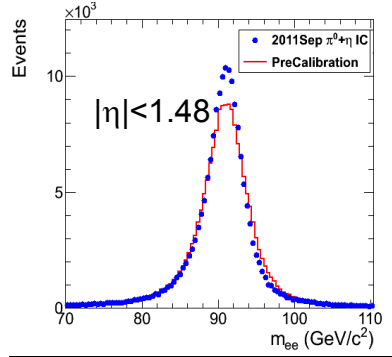


Figure 4.2: Z peak reconstructed using pre-LHC calibration constants (red) or September 2011 π^0/η -derived intercalibration constants (blue). Reprinted from ref. [67].

- 1054 • E/p absolute calibration, comparing the momentum measured in the tracker p
 1055 to the energy measured in the ECAL E of a sample of electrons from Z decay

1056 By September 2011, the intercalibration precision in EB was measured to be be-
 1057 tween 0.3% and 1.1% using the π^0/η method [67]. Figure 4.2 shows the improvement
 1058 in Z reconstruction from pre-LHC calibration constants to the latest π^0/η -derived
 1059 constants.

1060 **Calibrated ES Hits**

1061 ES calibrated hits are formed from the three samples read out per sensor. Just as in the paren-
 1062 case of EB/EE crystals, ES uncalibrated hits gain-adjusted, pedestal-subtracted, and thetical
 1063 reconstructed using weights. To make a calibrated ES hit, intercalibration constants, remark
 1064 angle correction constants (for the non-uniformity of sensor angle with respect to the
 1065 vertical across ES), and a MIP-GeV absolute scale factor are applied.

1066 **Clustering**

1067 After calibrated ECAL hits are formed, they must be clustered into shapes that
 1068 represent the energy deposit from a single particle. *Basic clusters* are formed around
 1069 seed hits, defined as a hit that

- 1070 • has calibrated $E_T > 1(0.18)$ GeV in EB(EE),
- 1071 • does not originate from a dead channel or one with faulty hardware,
- 1072 • is not poorly calibrated,
- 1073 • was reconstructed with the standard algorithm (i.e. not a special recovery algo-
- 1074 rithm for channels with subpar data integrity),
- 1075 • is not saturated,
- 1076 • is not spike-like, and
- 1077 • is in time (EB).

1078 EB basic clusters are formed around the seeds via the *hybrid* algorithm, while EE basic
 1079 clusters are formed with the `multi5x5` algorithm [68]. In addition to non-radiating
 1080 electrons and unconverted photons, both algorithms are designed to also recover all of
 1081 the energy associated with electron bremsstrahlung deposits and photon conversions.
 1082 The geometry of the CMS magnetic field means that bremsstrahlung and conversions
 1083 will tend to spread the shower out in ϕ , not η . Both algorithms work by forming
 1084 basic clusters around seeds, then combining the basic clusters into *superclusters* (SC)
 1085 by searching in a window extended in the ϕ direction for all basic clusters consistent
 1086 with bremsstrahlung radiation from the primary electron, or with a photon conversion.
 1087 Figure 4.3 illustrates the hybrid algorithm in EB. In EE, the energy deposited in ES
 1088 must also be added into the total clustered energy sum.

1089 Figure 4.4 shows the effect of superclustering on $Z \rightarrow ee$ reconstruction.

1090 **Supercluster Corrections**

1091 The total clustered ECAL energy is defined as

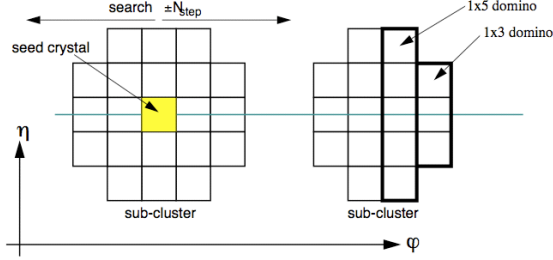


Figure 4.3: Hybrid algorithm in EB. The shower extent is essentially constant in η , but spreads out in ϕ as the two sub-clusters (or basic clusters) are grouped into the same supercluster. Reprinted from ref. [68].

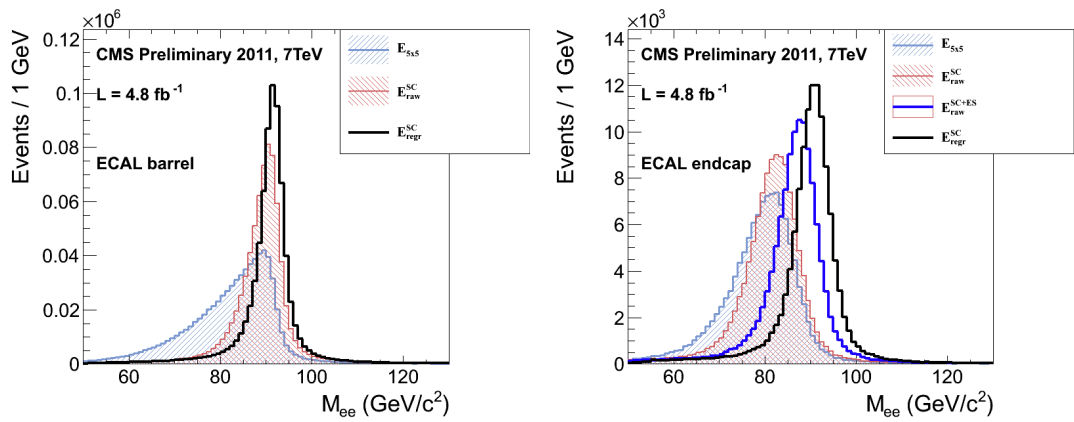


Figure 4.4: Z peak reconstructed in the dielectron channel for different kinds of clustering. The left plot is for EB and the right plot for EE. The constituent hits were calibrated with the best available intercalibrations and laser calibrations as of December 2011. The light blue histogram shows the reconstruction using a 5×5 energy sum, the red histogram shows the reconstruction using the SC energy for crystals only (the dark blue histogram on the right-hand side adds in the energy from ES), and the black histogram shows the reconstruction after the SCs are corrected using a multivariate method [?]. Reprinted from Fig. 30 of ref. [?].

$$E = F \times \sum_{i=1}^{n_{\text{crystal}}} G \times c_i \times A_i \quad (4.1)$$

where G is the ADC-GeV or MIP-GeV scale factor, c_i are the intercalibration constants, A_i is the uncalibrated hit amplitude in ADC counts, and F is a SC correction factor. G and c_i were explained in Sec. 4.1.1. F is a product of three factors for hybrid SCs (two for multi5x5 SCs) [68]:

1. $C_{\text{EB}}(\eta)$, which compensates for lateral energy leakage due to the crystal off-pointing in EB. These corrections are taken from MC simulation [68] and were confirmed in test beams [63].
2. $f(\text{brem})$, which corrects for biases in the clustering algorithms for showers characterized by differing amounts of bremsstrahlung. These corrections are taken from MC simulation [68].
3. Residual correction $f(E_T, \eta)$, due to the variation in η of detector material traversed by a primary electron or photon, and to any residual E_T dependence of the reconstruction. These corrections are determined from MC and validated on $Z \rightarrow ee$ data samples [69].

Changed

As a benchmark of ECAL calibration performance, the extra energy smearing in MC needed to achieve data/MC agreement in the Z width was between $\sim 0.9\%$ (in the central part of EB for electrons with little bremsstrahlung) and $\sim 3.3\%$ (in the outer part of EE for heavily radiating electrons) [70].

From Supercluster to Photon

The CMS photon object is any SC with $E_T > 10$ GeV and $H/E < 0.5$, unless the SC $E_T > 100$ GeV, in which case the H/E requirement is dropped. H/E is defined as the

ratio of energy in the HCAL in a 0.15 cone around the SC centroid, directly behind
 the SC, to the SC energy. SCs with $R9 > 0.94(0.95)$ in EB(EE), where $R9$ is defined
 as the ratio of the energy in the central 3×3 cluster of crystals divided by the SC
 energy $E_{3 \times 3}/E_{\text{SC}}$, are the best calibrated and most accurate type of electromagnetic
 shower. Therefore, for these objects, the photon energy is defined as the energy sum
 of the fully calibrated hits in the central 5×5 cluster around the seed (with $C_{\text{EB}}(\eta)$
 applied for EB photons). For all other SCs, the photon energy is equal to the fully
 corrected SC energy (cf. Sec. 4.1.1).

Reorganized

In this search, candidate photons and *fake photons* (f , “fakes”) are further selected
 according to the criteria listed in Table 4.1. Fakes are used in the determination of
 the QCD background, as explained in Chapter 5.

next 3

para-

graphs;

edited

Ta-

ble 4.1

caption

Table 4.1: Selection criteria for photons and fakes. “Pixel seed,” I_{comb} , and $\sigma_{i\eta i\eta}$ are
 defined in the text.

Variable	Cut (γ)	Cut (f)
SC $ \eta $	< 1.4442	< 1.4442
H/E	< 0.05	< 0.05
$R9$	< 1	< 1
Has pixel seed	No	No
$I_{\text{comb}}, \sigma_{i\eta i\eta}$	$< 6 \text{ GeV} \&\& < 0.011$	$(\geq 6 \&\& < 20 \text{ GeV}) \parallel \geq 0.011$

I_{comb} is defined as

Updated

effective

area

$$I_{\text{comb}} = I_{\text{ECAL}} - 0.093\rho + I_{\text{HCAL}} - 0.0281\rho + I_{\text{track}} \quad (4.2)$$

where I_{ECAL} , I_{HCAL} , and I_{track} are E_T sums in the annular regions defined in Figure 4.5
 and ρ is the average pileup energy density in the calorimeters (per unit $\eta \cdot \phi$) as
 measured with the Fastjet algorithm [71, 72]. Note that the ECAL and track isolation
 veto strips at constant η ensure that the isolation cuts are similarly efficient for
 converted photons, radiating electrons, and unconverted photons.

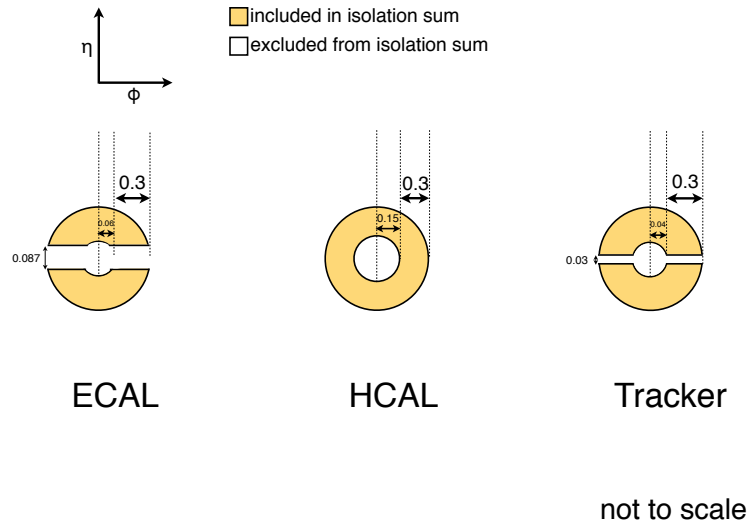


Figure 4.5: ECAL, HCAL, and track Isolation cones.

₁₁₃₀ $\sigma_{i\eta i\eta}$ is the log energy weighted extent of the shower in η and is defined as Added $\sigma_{i\eta i\eta}$

$$\sigma_{i\eta i\eta} = \frac{\sum_{i=1}^{25} w_i (\eta_i - \bar{\eta})^2}{\sum_{i=1}^{25} w_i} \quad (4.3) \quad \text{defini-} \quad \text{tion}$$

₁₁₃₁ where the sums run over the 5×5 matrix of crystals surrounding the seed, $w_i =$
₁₁₃₂ $\max(0, 4.7 + \ln(E_i/E))$, E_i is the energy of the i^{th} crystal, E is the total energy in the
₁₁₃₃ 25 crystals, η_i is the offset in η of the i^{th} crystal from the seed, and $\bar{\eta}$ is the weighted
₁₁₃₄ average η of the 25 crystals (using the w_i as weights) [73]. Changed

₁₁₃₅ Figure 4.6 shows the ρ distribution for a sample of two-photon events, with at average
₁₁₃₆ least one 40 GeV and one 25 GeV photon, passing the selection requirements in ρ ; up-
₁₁₃₇ Table 4.1 and the trigger requirements in Table 4.3. This sample represents the full dated
₁₁₃₈ 2011 dataset of 4.7 fb^{-1} . Since the average ρ is $\sim 7.5 \text{ GeV}$, and there is a long tail fig. 4.6
₁₁₃₉ above this average value, it is necessary to subtract pileup energy from the ECAL
₁₁₄₀ and HCAL isolation cones to recover otherwise clean photons in events with large
₁₁₄₁ pileup. The ECAL and HCAL *effective areas* of 0.093 and 0.0281, respectively, are

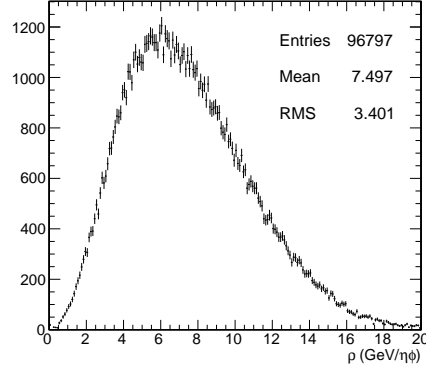


Figure 4.6: ρ distribution for a sample of two-photon events, with at least one 40 GeV and one 25 GeV photon, passing the selection requirements in Table 4.1 and the trigger requirements in Table 4.3. This sample covers the full 2011 dataset of 4.7 fb^{-1} .

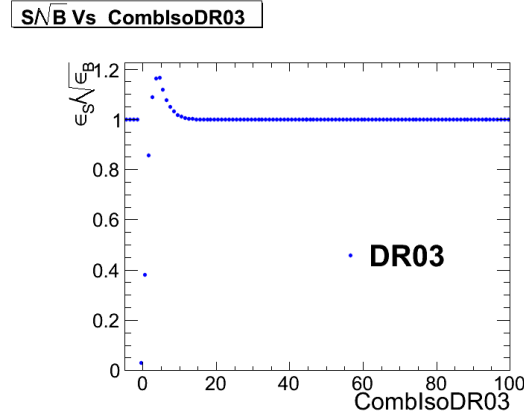


Figure 4.7: S/\sqrt{B} (S and B defined in the text) vs. combined isolation. Reprinted from Fig. 7 of ref. [74].

1142 calculated by fitting the average ECAL or HCAL isolation energy vs. ρ in a sample
 1143 of $Z \rightarrow ee$ events to a straight line. The slope of the line—which has the units of $\eta \cdot \phi$,
 1144 or area—is the effective area.

1145 The cut on combined isolation of 6 GeV (Table 4.1) is the result of an S/\sqrt{B}
 1146 optimization procedure [74]. S is a sample of photons in simulated GGM events that
 1147 are products of neutralino decay, while B is a sample of photons matched to generated
 1148 hadronic jets in simulated QCD events. Figure 4.7 shows the value of S/\sqrt{B} vs.
 1149 combined isolation, in particular the pronounced peak around 6 GeV.

New

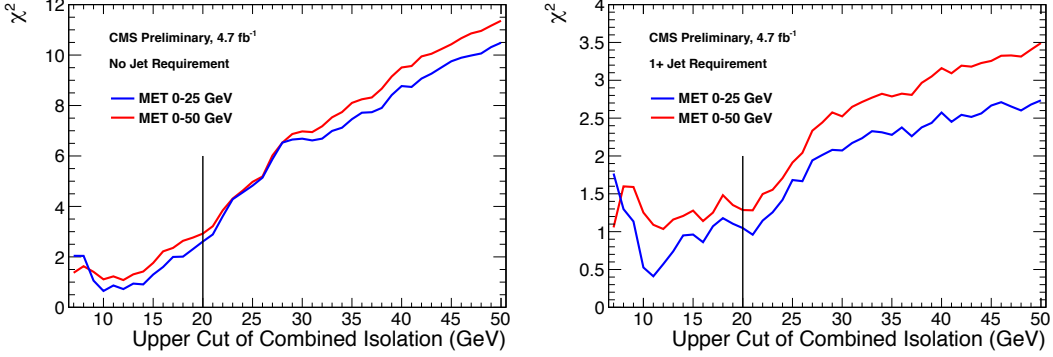


Figure 4.8: Neyman’s χ^2 between the ff and $\gamma\gamma$ \cancel{E}_T distributions, truncated at either 25 (red) or 50 (blue) GeV, vs. upper bound on fake combined isolation. The left plot includes all events; the right plot is for events with ≥ 1 jet defined as in Table 4.2, but with the ΔR cleaning criteria applied to the two primary EM objects and all additional electrons, photons, and fake photons. The full reweighting and normalization procedure is employed in the \cancel{E}_T calculation (see Sec. 5.1). Error bars include statistical, reweighting, and normalization error (see Sec. 5.3). Reprinted from Fig. 9 of ref. [74].

1150 The upper bound on fake photon combined isolation guarantees that poorly iso-
 1151 lated dijet events, with \cancel{E}_T resolution dissimilar to the candidate diphoton events,
 1152 do not enter the ff sample. The exact value of 20 GeV (cf. Table 4.1) arises from
 1153 a low- \cancel{E}_T $ff/\gamma\gamma$ χ^2 optimization procedure [74]. Figure 4.8 shows the value of the
 1154 Neyman’s χ^2 between the ff and $\gamma\gamma$ \cancel{E}_T distributions, truncated at either 25 or 50
 1155 GeV, vs. upper bound on fake combined isolation. As shown in the figure, 20 GeV
 1156 very nearly minimizes the χ^2 , while also being large enough that a sufficient number
 1157 of ff events may be collected.

1158 Finally, a “pixel seed” is defined as a hit in the pixel detector consistent with a
 1159 track extrapolated from the position of the ECAL SC back to the primary vertex.
 1160 Real photons, having no charge and therefore no bending in the magnetic field, should
 1161 not have a pixel seed.

1162 4.1.2 Electrons

1163 Electrons are reconstructed identically to photons, except that in the electron case
1164 the presence of a pixel seed is enforced, rather than vetoed.² Photons and electrons
1165 are defined by very similar criteria so that $Z \rightarrow ee$ events can be used to model
1166 the QCD background in the two-photon sample without introducing any bias in the
1167 electron energy measurement (cf. Sec. 5.1).

1168 4.1.3 Jets and Missing Transverse Energy

1169 Particle Flow

1170 In this analysis, jets and \cancel{E}_T are formed from *particle flow* (PF) candidates. The parti-
1171 cle flow algorithm [78, 79] uses information from all CMS subdetectors to reconstruct
1172 as accurately as possible the positions and momenta of all visible jet constituents,
1173 exploiting the fine granularity of the tracker and ECAL to achieve a greatly improved
1174 momentum resolution over calorimeter-only jets [80]. The PF algorithm is summa-
1175 rized below [81].

1176 1. Reconstruct the fundamental detector objects via iterative procedures

- 1177 • Tracks in the inner silicon layers
 - 1178 – High efficiency and low fake rate for charged hadrons in jets
 - 1179 – Relaxed primary vertex constraint allows photon conversions, parti-
1180 cles originating from nuclear interactions in the silicon, and long-lived
1181 particles to be reconstructed
- 1182 • Calorimeter clusters
- 1183 • Muon tracks in the outer muon layers

2In many CMS analyses, electrons are reconstructed very differently from photons. In particular, a special tracking algorithm [77] is used to best follow a radiating electron. However, in this analysis, the electron tracking is not used.

1184 2. Create a “block” of linked fundamental objects

- 1185 • Link silicon tracks to calorimeter clusters via $\Delta R_{\text{track-cluster}}$ (account for
1186 electron bremsstrahlung)
- 1187 • Link clusters in one calorimeter layer to clusters in a separate layer via
1188 $\Delta R_{\text{cluster-cluster}}$
- 1189 • Link silicon tracks to muon tracks via global track χ^2

1190 3. ID the particles in the block

- 1191 • If global (silicon + muon layers) muon p_T is compatible with silicon track
1192 p_T , ID as a muon and remove corresponding tracks from block
- 1193 • ID electron tracks via special algorithm and removed all corresponding
1194 tracks and cluster from block
- 1195 • Remove fake tracks from the block Fixed
- 1196 • Remove excess track-cluster links via $\Delta R_{\text{track-cluster}}$ minimization (but al-
1197 low multiple tracks to be associated to one cluster) typo
- 1198 • If the cluster energy is significantly larger then the energy of the linked
1199 track, ID as a PF photon or PF neutral hadron and remove corresponding
1200 clusters from the block
- 1201 • If the cluster is not linked to a track, ID as a PF photon or PF neutral
1202 hadron and remove corresponding clusters from the block
- 1203 • Remaining track-cluster links are PF charged hadrons

1204 **Jets**

1205 PF candidates are clustered into jets by means of the anti- k_T algorithm with $R = 0.5$
1206 [82]. In this algorithm, all possible pairs of PF candidates i, j are looped over, and
1207 the momenta of the pair that minimize the distance variable

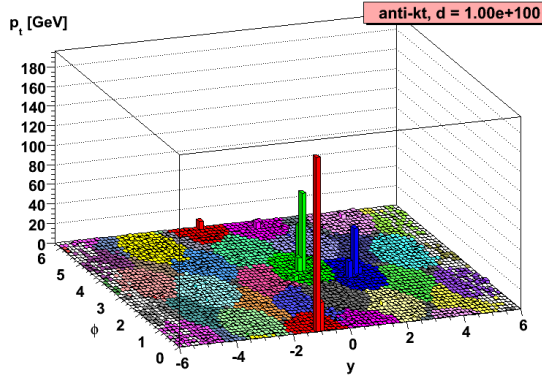


Figure 4.9: Example event display showing jets clustered via the anti- k_T algorithm. y is pseudorapidity. Reprinted from slide 85 of ref. [83].

$$d_{ij} = \frac{\Delta R_{ij}^2}{R^2 \max(k_{Ti}^2, k_{Tj}^2)} \quad (4.4)$$

1208 are combined, where k_{Ti} is the transverse momentum of “combined” PF candidate i .
 1209 The constituent PF candidates are clustered together. The process is repeated until
 1210 $d_{ij} > 1/k_{Ti}^2$ for all pairs of clustered PF momenta [83]. An illustration is given in Fig-
 1211 ure 4.9. The anti- k_T algorithm is infrared and collinear safe, leading to well-behaved Added
 1212 theoretical predictions and ease of comparison between data and MC simulation. It refer-
 1213 also tends to form circular jets, making it easy for experimental effects such as ex- ence to
 1214 pected out-of-cone energy and fiducial acceptance to be measured or simulated. For Fig. 4.9
 1215 these reasons, the anti- k_T jet clustering algorithm was chosen for this analysis.

1216 Once jets are clustered, they must be corrected for biases in the energy mea-
 1217 surement due to non-compensation [84], invisible energy (lost to overcoming nuclear
 1218 binding energy, in neutrinos, or in unclustered muons, for example) [84], detector
 1219 geometry and cracks [85], zero suppression and trigger inefficiencies [86], pileup, and
 1220 effects of the clustering algorithm [85]. Four multiplicative correction factors are ap-
 1221 plied to the raw jet four-momentum p_μ^{raw} [80]:

- 1222 • $C_{\text{offset}}(p_T^{\text{raw}})$, which accounts for extra energy due to noise, pileup, and the un-

1223 derlying event;

- 1224 • $C_{\text{MC}}(C_{\text{offset}}p_T^{\text{raw}}, \eta)$, which is derived from MC and accounts for most of the p_T
 1225 and η dependence;
- 1226 • $C_{\text{rel}}(\eta)$, which accounts for the remaining differences in uniformity over the
 1227 entire calorimeter between data and MC; and
- 1228 • $C_{\text{abs}}(C_{\text{rel}}C_{\text{MC}}C_{\text{offset}}p_T^{\text{raw}})$, which accounts for the remaining differences in linear-
 1229 ity over the full p_T range between data and MC.

1230 Figure 4.10 shows the total jet energy correction factor $C_{\text{offset}}C_{\text{MC}}C_{\text{rel}}C_{\text{abs}}$ vs. η
 1231 for jets reconstructed with the anti- k_T algorithm, $R = 0.5$. The PF jet corrections
 1232 are more uniform across η than those of CALO jets (composed of simple calorimeter
 1233 towers) or JPT jets (Jet Plus Tracks; composed of calorimeter energies replaced,
 1234 where possible, with matching track p_T) [87]. In addition, for p_T in the range 30-200
 1235 GeV and $|\eta|$ up to 2.0, the PF jet energy correction uncertainty is lower than that of
 1236 the other two types of jets, and never exceeds $\sim 3\%$ [80]. The superior performance
 1237 of PF jets motivates their use in this search.

1238 In this analysis, candidate and QCD control events are binned by number of jets
 1239 satisfying the criteria in Table 4.2.

1240 Missing Transverse Energy

1241 To be consistent with the jet reconstruction, \cancel{E}_T in this analysis is also reconstructed
 1242 from PF candidates. Raw \cancel{E}_T is defined as

$$\cancel{E}_{T\text{raw}} = \left| - \sum_{i=1}^{n_{\text{PF}}} \vec{p}_{Ti} \right| \quad (4.5)$$

Table 4.2: Definition of HB/HE hadronic jets.

Variable	Cut
Algorithm	L1FastL2L3Residual corrected PF
p_T	$> 30 \text{ GeV}$
$ \eta $	< 2.6
Neutral hadronic energy fraction	< 0.99
Neutral electromagnetic energy fraction	< 0.99
Number of constituents	> 1
Charged hadronic energy	$> 0.0 \text{ GeV}$ if $ \eta < 2.4$
Number of charged hadrons	> 0 if $ \eta < 2.4$
Charged electromagnetic energy fraction	< 0.99 if $ \eta < 2.4$
ΔR to nearest PF electron ^a , muon ^b , or one of the two primary EM objects	> 0.5

^aA PF electron is defined as an electron reconstructed with the PF algorithm [75] with $p_T > 15 \text{ GeV}$, $|\eta| < 2.6$, and $(I_{\text{charged}} + I_{\text{photon}} + I_{\text{neutral}})/p_T < 0.2$, where $I_{\text{charged}}(I_{\text{photon}})(I_{\text{neutral}})$ is the sum of PF charged hadron(PF photon)(PF neutral hadron) momenta in a $\Delta R = 0.4$ cone around the PF electron.

^bMuons are reconstructed [76] from a combination of muon station and inner tracker hits. Here, a muon must have track $\chi^2 < 10$, at least one good muon station hit, inner track transverse impact parameter $< 0.02 \text{ cm}$, inner track longitudinal impact parameter $< 0.5 \text{ cm}$, $p_T > 15 \text{ GeV}$, $|\eta| < 2.6$, and $(I_{\text{ECAL}} + I_{\text{HCAL}} + I_{\text{track}})/p_T < 0.2$, where $I_{\text{ECAL}}(I_{\text{HCAL}})(I_{\text{track}})$ is the sum of ECAL(HCAL)(track) momenta in a $\Delta R = 0.3$ cone around the muon.

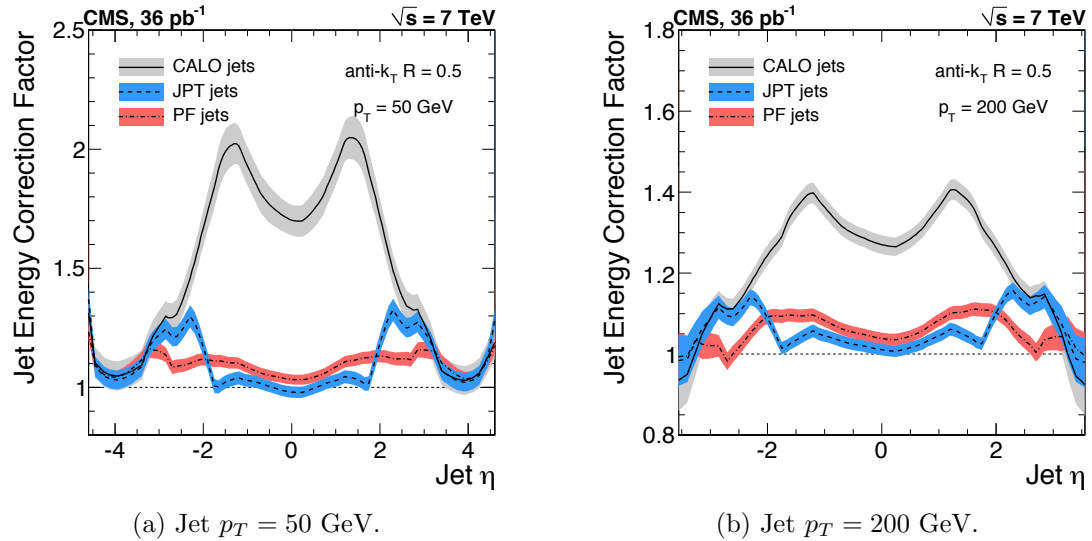


Figure 4.10: Total jet energy correction factor $C_{\text{offset}}C_{\text{MC}}C_{\text{rel}}C_{\text{abs}}$ vs. η , including uncertainty band, for jets reconstructed with the anti- k_T algorithm, $R = 0.5$. Reprinted from Fig. 26 of ref. [80].

where n_{PF} is the number of PF candidates in the event. $\cancel{E}_{T\text{raw}}$ may be corrected for the same effects that necessitate jet corrections, since $\cancel{E}_{T\text{raw}}$ is usually the result of jet mis-measurement (except, of course, in electroweak physics processes that include an energetic neutrino, or SUSY production). CMS *Type-I* \cancel{E}_T corrections simply involve replacing the PF jets with their corrected energies (cf. Sec 4.1.3) and recalculating \cancel{E}_T . Only jets with electromagnetic fraction (EMF) below 90% and $p_T > 20$ GeV are replaced. This ensures that very electromagnetic jets (as well as isolated leptons, which also receive no correction), which consist chiefly of neutral pions and are measured accurately by the ECAL, do not receive a correction derived for jets with a large fraction of their energy in charged hadrons. In addition, the p_T cut guarantees that jet corrections are only applied where they are known to within a few percent. For this search, the level of agreement between the SM background estimate and the two-photon search sample in a low- \cancel{E}_T control region is the same regardless of whether the \cancel{E}_T is corrected or not, so for simplicity the Type-I \cancel{E}_T corrections are not used (see Sec. ??).

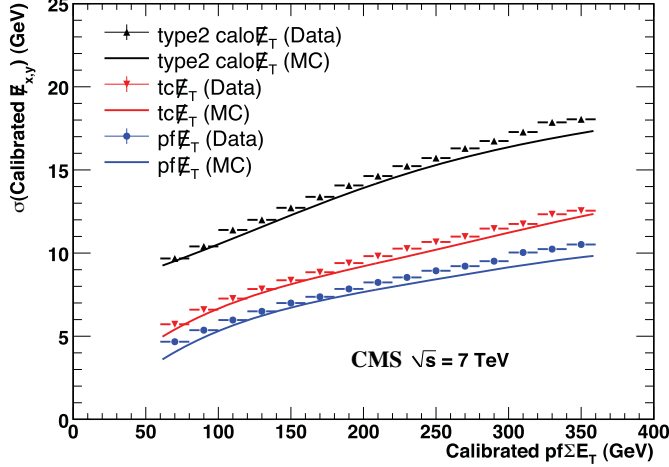


Figure 4.11: σ of a Gaussian fit to the x- and y-components of calibrated E_T vs. the calibrated PF E_T sum in a sample of events containing at least two jets with $p_T > 25$ GeV. σ is calibrated such that the E_T scale is equal for all three algorithms. PF $\sum E_T$ is corrected, on average, to the particle level using a Pythia v8 simulation [88]. The blue markers (data) and line (MC) refer to PF jets. Reprinted from Fig. 13 of ref. [86].

1258 Figure 4.11 shows the σ of a Gaussian fit to the x- and y-components of calibrated
 1259 E_T vs. the calibrated PF E_T sum in a sample of events containing at least two jets
 1260 with $p_T > 25$ GeV. Again, PF E_T outperforms E_T constructed of calorimeter towers
 1261 or track-corrected calorimeter deposits.

1262 4.2 HLT

1263 From the objects described in Sec. 4.1, four samples of events are formed:

- 1264 • $\gamma\gamma$ candidate sample, in which the two highest E_T objects are photons,
- 1265 • $e\gamma$ control sample, in which the two highest E_T objects are one electron and
 one photon,
- 1267 • ee control sample, in which the two highest E_T objects are electrons, and
- 1268 • ff control sample, in which the two highest E_T objects are fakes.

1269 In all samples, the leading EM object is required to have $E_T > 40$ GeV, while the
1270 trailing EM object is required to have $E_T > 25$ GeV. The high level triggers used to
1271 select the four samples, by run range, are listed in Table 4.3. No trigger is prescaled.

Table 4.3: HLT paths triggered by the $\gamma\gamma$, $e\gamma$, ee , and ff samples, by run range. No triggers are prescaled.

Run range	$\gamma\gamma$	$e\gamma$	ee	ff
160404-163261	Photon26_ IsoVL_ Photon18	Photon26_ IsoVL_ Photon18	Photon26_ IsoVL_ Photon18	Photon26_ IsoVL_ Photon18
161216-166967	Photon36_ CaloIdL_ Photon22_ CaloIdL	Photon36_ CaloIdL_ Photon22_ CaloIdL	Photon36_ CaloIdL_ Photon22_ CaloIdL	Photon36_ CaloIdL_ Photon22_ CaloIdL
166347-180252	Photon36_ CaloIdL_ IsoVL_ Photon22_ CaloIdL_ IsoVL	Photon36_ CaloIdL_ IsoVL_ Photon22_ CaloIdL_ IsoVL	Photon36_ CaloIdL_ IsoVL_ Photon22_ R9Id	Photon36_ CaloIdL_ IsoVL Photon36_ CaloIdL_ IsoVL Photon36_ R9Id_ Photon22_ CaloIdL_ IsoVL Photon36_ R9Id_ Photon22_ R9Id

1272 Each piece of the HLT path name is defined as follows.

- 1273 • Photon: Energy deposit in the ECAL that fired an L1 trigger (cf. Sec. 3.2.1).

1274 For Photon26_IsoVL_Photon18, the L1 seed E_T threshold is 12 GeV, while for Switched
 1275 all other triggers in Table 4.3 it is 20 GeV (cf. Sec. 3.2.1). HLT
 1276 • Integer following the word **Photon**: E_T threshold in GeV for offline reconstructed path
 1277 photon, using the full photon reconstruction of Sec. 4.1.1 minus the laser cali- names
 1278 brations and assuming the primary vertex at (0, 0, 0). to ver-
 1279 • **CaloIdL**: For EB photons, $H/E < 0.15$ and $\sigma_{in\eta} < 0.014$. batim
 1280 • **IsoVL**: $I_{ECAL} < 0.012E_T + 6$ GeV, $I_{HCAL} < 0.005E_T + 4$ GeV, and $I_{track} <$ font and
 1281 $0.002E_T + 4$ GeV. added
 1282 • **R9Id**: $R9 > 0.8$. reference
 1283 In addition, the versions of **HLT_Photon26_IsoVL_Photon18** and to L1
 1284 **Photon36_CaloIdL_Photon22_CaloIdL** that were active during runs 160404-163268 section
 1285 included a cut $E_{max}/E_{5\times5} < 0.98$ for spike rejection. E_{max} is the energy in the Switched
 1286 highest HLT path
 1287 energy crystal of the EM cluster and $E_{5\times5}$ is the energy in the 5×5 crystal matrix names
 1288 around the seed crystal. For runs after 163268, Swiss cross spike rejection of individual to ver-
 1289 crystals from HLT quantities was performed (cf. Sec. 4.1.1). All information about the batim
 1290 evolution of the CMS HLT settings can be found in the HLT configuration browser font
 1291 at <http://j2eeps.cern.ch/cms-project-confdb-hltdev/browser/>. Switched
 1292 As an example of the naming convention just described, the HLT path HLT
 1293 **Photon36_CaloIdL_IsoVL_Photon22_R9Id** is fired if one photon is found with $E_T >$ path
 1294 36 GeV passing the **CaloIdL** and **IsoVL** requirements, and another is found with names
 1295 $E_T > 22$ GeV passing the **R9Id** requirement. to ver-
 1296 For the offline E_T cuts described in this section, the triggers are > 99% efficient, batim
 1297 as shown in Figure 4.12 [74]. The efficiencies are measured with respect to triggers font
 1298 with lower E_T thresholds. Added
 1299 HLT ef-
 1300 ficiency
 1301 discus-
 1302 sion

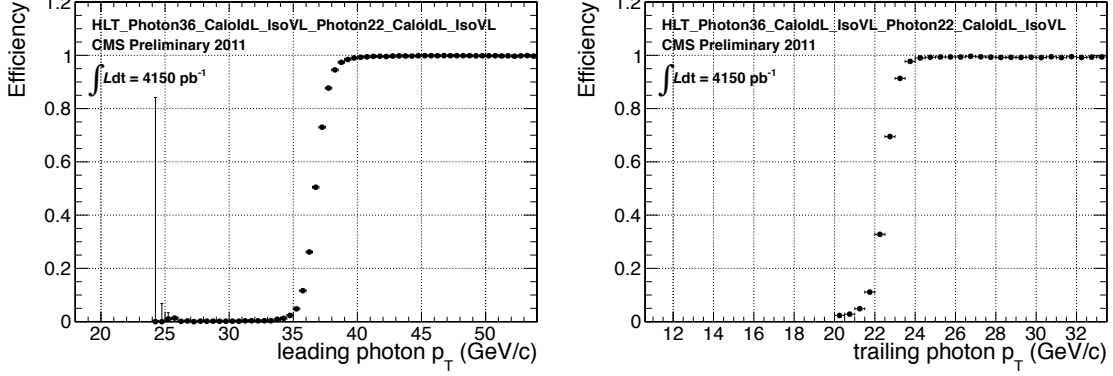


Figure 4.12: Efficiency of `HLT_Photon36_CaloIdL_IsoVL_Photon22_CaloIdL_IsoVL` for offline selected leading photon (left) and trailing photon (right) vs. photon p_T . Reprinted from Fig. 2 of ref. [74].

1298 4.3 Event Quality

1299 To suppress instrumental backgrounds, a set of event quality cuts are applied to the
 1300 $\gamma\gamma$, $e\gamma$, ee , and ff samples. First, all events are required to pass a good run selec-
 1301 tion, as determined by the CMS Physics Validation Team (<https://twiki.cern.ch/twiki/bin/view/CMS/PVTMain>, CERN computing ID needed). The good run selec-
 1302 tion excludes luminosity sections during which a sufficient part of the CMS detector
 1303 was unpowered or malfunctioning. Such conditions could occur if, for example, a high
 1304 voltage supply trips off in the middle of a run, or a DAQ error corrupts data quality
 1305 but is not spotted until after the data have been collected. The severity of a detec-
 1306 tor problem is judged by its effect on a wide range of analyses and reconstruction
 1307 algorithms. Of the $\sim 5 \text{ fb}^{-1}$ of integrated luminosity delivered by the LHC in 2011,
 1308 4.68 fb^{-1} passed the good run selection. This analysis is performed on the entire 2011
 1309 certified dataset.

1311 Second, all events must contain at least one good interaction vertex. The criteria
 1312 for a good vertex are:

- 1313 • $\chi^2 \neq 0 \parallel \text{ndof} \neq 0 \parallel N_{\text{tracks}} \neq 0$, where χ^2 and ndof are calculated for the track
 1314 fit to the vertex, and N_{tracks} is the number of tracks in the vertex fit

- 1315 • $\text{ndof} > 4$
- 1316 • $|z| < 24 \text{ cm}$, where z is the z -coordinate of the vertex position
- 1317 • $|\rho| < 2 \text{ cm}$, where ρ is the transverse displacement of the vertex position from
1318 the beam line

1319 The good vertex requirement eliminates non-collision backgrounds such as beam
1320 scraping, beam halo, cosmic muon interactions, and instrumental effects.

1321 Third, the two electromagnetic objects in the $\gamma\gamma$, $e\gamma$, ee , and ff events must
1322 be separated in ϕ by at least 0.05. This requirement protects against beam halo
1323 bremsstrahlung, in which a halo muon traveling parallel to the beam line radiates an
1324 energetic photon while itself depositing a large amount of energy in the ECAL. In
1325 this case, the two ECAL hits would likely be at the same ϕ (and ρ).

1326 Fourth, the two EM objects must be separated in R by at least 0.6. Since the
1327 isolation cone size used is 0.3, this ensures that the isolation energy of one EM object
1328 cannot be in the veto strip (Fig. 4.5) of the other.

1329 Finally, the $\gamma\gamma$, $e\gamma$, ee , and ff events must pass an HCAL noise filter and ECAL
1330 dead channel filter. The HCAL noise filter guarantees that all HCAL reconstructed
1331 hits are inconsistent with any noise source. Noise sources [89] include:

- 1332 • Ion feedback in the HPDs absent any true incident photons, in which a thermal
1333 electron ionizes a molecule in the HPD acceleration gap, faking a real signal
- 1334 • HPD discharge affecting nearly all channels in the same HPD [90], partially
1335 explained by the effect of the 4 T CMS magnetic field on the flashover voltage
1336 of the dielectric [92]
- 1337 • Concurrent signals in nearly all 72 channels of a single RBX, as yet unexplained
- 1338 • HF PMT window hits (as opposed to the usual quartz fiber hits)

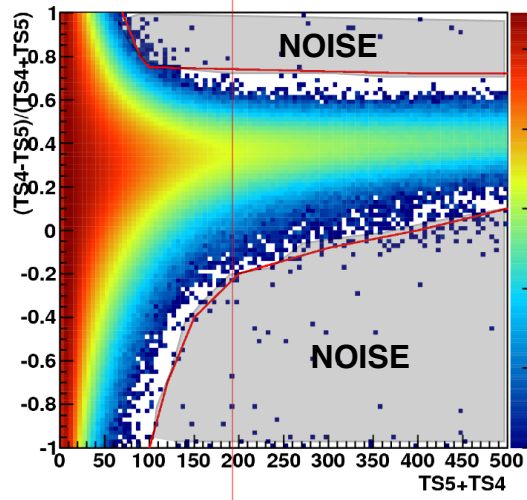


Figure 4.13: $(TS4 - TS5)/(TS4 + TS5)$ vs. $TS4 + TS5$ for a minimum bias sample. HB/HE hits are considered noisy if they lie in the sparsely populated gray region labeled "NOISE" defined by the curved red lines. Adapted from ref. [91].

- 1339 • ADC saturation

- 1340 Since HCAL noise may induce fake jets or E_T , events are rejected if any of the
- 1341 following criteria are true:

- 1342 • Any HPD has > 17 hits

- 1343 • A single HPD has > 10 hits, but every other HPD has zero hits

- 1344 • An RBX has > 10 zero-ADC-count hits

- 1345 • Any HB/HE reconstructed hit corresponding to an RBX with > 50 GeV of
- 1346 energy fails a two-dimensional cut defined by the variables $(TS4 - TS5)/(TS4 +$
- 1347 $TS5)$ vs. $TS4 + TS5$, where $TS4(TS5)$ is the hit amplitude in the fourth(fifth)
- 1348 time sample read out for that hit. The cut is defined in Fig. 4.13.

- 1349 The ECAL dead channel filter is designed to flag events in which significant EM
- 1350 energy was deposited in a masked region of the ECAL by using the trigger primitive
- 1351 information for the corresponding trigger tower. Energy deposited in a masked region

1352 of ECAL can cause fake E_T . Events are rejected if the trigger primitive E_T exceeds
1353 the maximum value of 63.75 GeV in any trigger tower that is masked in the readout.

1354 4.4 Photon Identification Efficiency

1355 In order to determine the cross section (or cross section upper limit) for a GGM
1356 signal, the photon identification efficiency is needed. Since no suitably large sample
1357 of $Z \rightarrow \mu\mu\gamma$ events in CMS exists yet, the efficiency calculation relies on the similarity
1358 between detector response to electrons and photons. A scale factor to correct the MC
1359 photon ID efficiency to the real photon efficiency for the data is obtained from the
1360 ratio of the electron efficiency from the data to the electron efficiency from MC.
1361 The different types of photon ID variables—calorimeter and track isolation, ratio of Removed
1362 hadronic to electromagnetic energy of the shower, and transverse shower shape—are refer-
1363 chosen so that their distributions for isolated electrons and photons are similar.³ ence to
1364 The photon selection efficiency is plots

$$\epsilon_\gamma = \epsilon_\gamma^{\text{MC}} \times \frac{\epsilon_e^{\text{data}}}{\epsilon_e^{\text{MC}}} \quad (4.6)$$

1365 where

- 1366 • ϵ_γ is the photon ID efficiency in data,
- 1367 • $\epsilon_\gamma^{\text{MC}}$ is the photon ID efficiency in MC,
- 1368 • ϵ_e^{data} is the electron ID efficiency obtained using $Z \rightarrow ee$ electrons in the data
1369 that satisfy the photon ID cuts, and

3 $R9$ differs between photons and radiating electrons, but the requirement $R9 < 1$ is loose enough not to introduce problems with the use of electrons to measure the photon ID efficiency.

- 1370 • ϵ_e^{data} is the electron ID efficiency obtained using $Z \rightarrow ee$ electrons in MC that
 1371 satisfy the photon ID cuts.

1372 The ratio $\epsilon_e^{\text{data}}/\epsilon_e^{\text{MC}}$ is defined as the scale factor by which the GGM signal MC
 1373 photon ID efficiency must be multiplied to give an estimate of the photon ID efficiency
 1374 in data. The photon ID requirements of Table 4.1 plus the IsoVL HLT requirement
 1375 described in Sec. 4.2 and Table 4.3 are repeated in Table 4.4.

Table 4.4: Candidate photon ID requirements.

Variable	Cut
I_{ECAL}	$< 0.012E_T + 6 \text{ GeV}$
I_{HCAL}	$< 0.005E_T + 4 \text{ GeV}$
I_{track}	$< 0.002E_T + 4 \text{ GeV}$
H/E	< 0.05
$\sigma_{i\eta i\eta}$	< 0.011
$I_{\text{ECAL}} - 0.0792\rho + I_{\text{HCAL}} - 0.0252\rho + I_{\text{track}}$	$< 6 \text{ GeV}$
$R9$	< 1

1376 4.4.1 Tag and Probe Method

1377 A *Z tag and probe* method is utilized to measure the efficiency of the photon ID
 1378 cuts in Table 4.1. The tag is a well-identified electron. The probe, by contrast, is as
 1379 loosely identified as possible, and all tags must pass the probe criteria in addition to
 1380 the stringent tag criteria. The tag and probe criteria used in this study are shown in
 1381 Table 4.5.

1382 The invariant mass of the tag and probe are required to be within a narrow window
 1383 around Z mass. Assuming that the probabilities of the tag and probe legs of the Z
 1384 decay to pass the photon ID cuts are uncorrelated, the efficiency can be estimated as

$$\epsilon = \frac{N_{\text{tag-pass}}}{N_{\text{tag-pass}} + N_{\text{tag-fail}}} \quad (4.7)$$

Table 4.5: Tag and probe criteria. The superscript 0.4 indicates that the isolation variable was calculated in a cone of $\Delta R = 0.4$ around the photon candidate. The isolations without superscripts use the standard $\Delta R = 0.3$ cones.

Variable	Cut	
	Tag	Probe
RECO object	photon	photon
HLT	HLT_Ele17_CaloIdVT_CaloIsoVT_TrkIdT_TrkIsoVT_SC8_Mass30_v* (must have fired the 17 GeV leg)	—
H/E	< 0.05	< 0.15
$I_{\text{ECAL}}^{0.4}$	$< 0.006E_T + 4.2 \text{ GeV}$	—
$I_{\text{HCAL}}^{0.4}$	$< 0.0025E_T + 2.2 \text{ GeV}$	—
$I_{\text{track}}^{0.4}$	$< 0.001E_T + 2.0 \text{ GeV}$	—
E_T	$> 25 \text{ GeV}$	—
SC E_T	—	$> 15 \text{ GeV}$
SC $ \eta $	< 1.4442	< 1.4442
$\sigma_{i\eta i\eta}$	< 0.009	—
Has pixel seed	Yes	—
Track match type	General track ^a	—
Track match ΔR	< 0.04	—
Track match p_T	$> 15 \text{ GeV}$	—
Track match $ \eta $	< 1.479	—

^aA general track is reconstructed with the CMS standard combinatorial track finder [93].

1385 where $N_{\text{tag-pass}}$ is the number of tag-probe pairs in which the probe leg passes the
 1386 photon ID cuts under study and $N_{\text{tag-fail}}$ is the number of tag-probe pairs in which
 1387 the probe leg fails the cuts. Implicit in these definitions is a double counting of pairs
 1388 in which both electrons pass the tag and probe criteria [94]. In addition, in the rare
 1389 circumstance (less than 1% in MC [94]) that two or more probes may be matched to
 1390 one tag, the pair with invariant mass closest to the Z mass is chosen.

1391 In practice, $N_{\text{tag-pass}}$ and $N_{\text{tag-fail}}$ are returned by a simultaneous unbinned maxi-
 1392 mum likelihood fit to the invariant mass distributions of tag-pass and tag-fail events,
 1393 with appropriate signal and background PDF assumptions. The fit form used is

$$\begin{aligned} f_{\text{tag-pass}}(m_{\text{tag-pass}}) &= \epsilon N_S f_S^{\text{pass}}(m_{\text{tag-pass}}) + N_B^{\text{pass}} f_B^{\text{pass}}(m_{\text{tag-pass}}) \\ f_{\text{tag-fail}}(m_{\text{tag-fail}}) &= (1 - \epsilon) N_S f_S^{\text{fail}}(m_{\text{tag-fail}}) + N_B^{\text{fail}} f_B^{\text{fail}}(m_{\text{tag-fail}}) \end{aligned} \quad (4.8)$$

1394 where $f_{\text{tag-pass}}(m_{\text{tag-pass}})$ and $f_{\text{tag-fail}}(m_{\text{tag-fail}})$ are the tag-pass and tag-fail PDFs,
 1395 respectively; ϵ is the efficiency; N_S is the total number of Z signal events summed over
 1396 both samples; $f_S^{\text{pass}}(m_{\text{tag-pass}})$ and $f_S^{\text{fail}}(m_{\text{tag-fail}})$ are the tag-pass and tag-fail signal
 1397 PDFs, respectively; N_B^{pass} and N_B^{fail} are the numbers of background events in the tag-
 1398 pass and tag-fail samples, respectively; and $f_B^{\text{pass}}(m_{\text{tag-pass}})$ and $f_B^{\text{fail}}(m_{\text{tag-fail}})$ are the
 1399 tag-pass and tag-fail background PDFs, respectively. This particular implementation
 1400 of the tag and probe methodology is based on tag `CMSSW_4_2_5` of the CMSSW
 1401 package `PhysicsTools/TagAndProbe`, and uses the MINUIT2 [95] library, as coded
 1402 in RooFit [96], for the likelihood maximization. For this study, CMSSWv4.2.8 was
 1403 used.

1404 For both samples, the signal shape is assumed to be a Crystal Ball function [97]
 1405 convoluted with the Z generated lineshape, while the background shape is a PDF
 1406 that describes the falling background as well as the kinematic turn-on at low invariant

1407 mass. The background PDF, called `RooCMSShape` [94], is given by

$$f_{\text{RooCMSShape}}(x) = \begin{cases} 1e20 & \text{for } (x - \mu)\gamma < -70 \\ 0 & \text{for } (x - \mu)\gamma > 70 \\ \text{erfc}((\alpha - x)\beta) \exp(-(x - \mu)\gamma) & \text{otherwise} \end{cases} \quad (4.9)$$

1408 where α , β , γ , and μ are parameters of the fit, most of which are held fixed. In the
1409 three lowest E_T bins, all parameters of the tag-pass and tag-fail background PDFs
1410 are left floating, because the effect of the relaxed E_T cuts has a significant effect on
1411 the background shape. More details of the signal and background PDFs are given
1412 in Table 4.6. The fixed signal and background parameter values were determined by
1413 fitting a small sample ($0.0 \leq \eta < 0.25$) of `Fall11 MC signal (DYJetsToLL)` and back-
1414 ground (`QCD_Pt-20to30_BCToE`, `QCD_Pt-30to80_BCToE`, `QCD_Pt-80to170_BCToE`,
1415 `GJet_Pt-20_doubleEMEnriched`, `WJetsToLNu`, `TTJets`) with parameters left float-
1416 ing.⁴

Added

1417 Some fit examples are shown in Figures 4.14 and 4.15. In Fig. 4.14, which shows fits
1418 fits to data and MC for $15 \text{ GeV} \leq \text{probe } E_T < 20 \text{ GeV}$, the kinematic turn-on is below
1419 the invariant mass range covered by the plot. The exponentially falling background
1420 is easily seen underneath the signal, and is especially pronounced in the background-
1421 dominated tag-fail sample.

1422 4.4.2 Photon Efficiency Scale Factor $\epsilon_e^{\text{data}}/\epsilon_e^{\text{MC}}$

1423 Figure 4.16 shows the dependence of the photon ID efficiency scale factor $\epsilon_e^{\text{data}}/\epsilon_e^{\text{MC}}$
1424 on E_T , η , and N_{jet} , where jets are defined as in Table 4.2, but with only the two
1425 Z electrons considered as candidates for overlap removal. Errors are statistical only.

1426⁴See Appendix A for a discussion of the MC samples.

Table 4.6: Parameter values (parameter definitions are in the text) for the signal and background PDFs for the different samples. The background PDF applies to all efficiency bins except the four lowest E_T bins, which use a floating `RooCMSShape` background. When a bracketed range is given, the parameter is allowed to float within that range. When a constant is given, the parameter is fixed to that constant.

PDF	Crystal Ball fit parameters				RooCMSShape fit parameters			
	μ	σ	α	n	μ	α	β	γ
Tag-pass signal	[-1.0, 1.0]	[1.0, 3.0]	0.87	97.0	N/A	N/A	N/A	N/A
Tag-fail signal	[-1.0, 1.0]	[1.0, 3.0]	0.73	134.9	N/A	N/A	N/A	N/A
Tag-pass background	N/A	N/A	N/A	N/A	65.0	61.949	0.04750	0.01908
Tag-fail background	N/A	N/A	N/A	N/A	α	[50.0, 100.0]	0.065	0.048

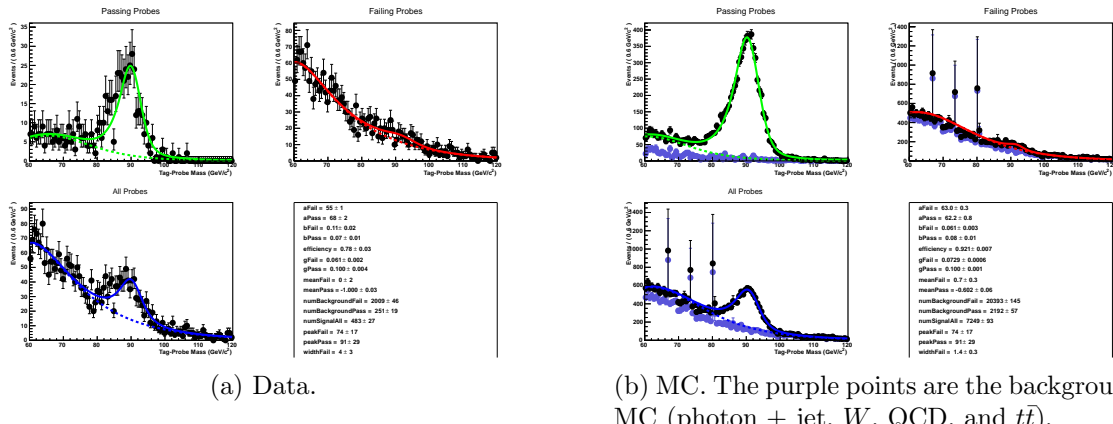


Figure 4.14: Tag and probe invariant mass fits for $15 \text{ GeV} \leq \text{probe } E_T < 20 \text{ GeV}$. Errors are statistical only. The tag-pass fit is shown in green, the tag-fail fit in red, and a fit to both samples in blue. Dotted lines are the background components of the fits; solid lines are signal plus background.

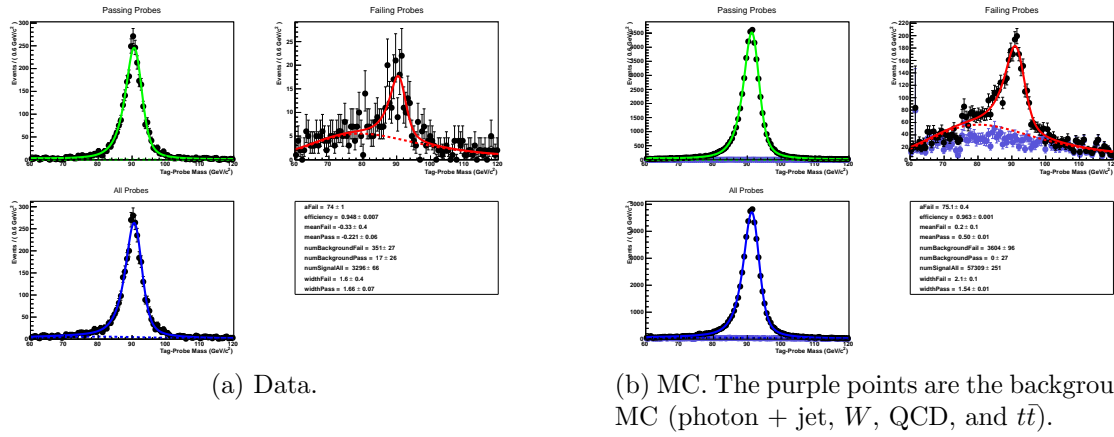


Figure 4.15: Tag and probe invariant mass fits for $-0.25 \leq \text{probe } \eta < -0.5$. Errors are statistical only. The tag-pass fit is shown in green, the tag-fail fit in red, and a fit to both samples in blue. Dotted lines are the background components of the fits; solid lines are signal plus background.

1426 There no significant dependence of the scale factor on these variables, so only one
1427 scale factor is computed from the entire dataset.

1428 The effect of pileup is studied by comparing the efficiencies ϵ_e^{data} and ϵ_e^{MC} vs. the
1429 number of primary vertices (N_{PV}) in the event. The efficiency only drops a few percent
1430 for events with large N_{PV} after using pileup-corrected isolation cuts, as can be seen in
1431 Figure 4.17a. The MC tracks the data, and the scale factor is flat vs. N_{PV} , as shown
1432 in Fig. 4.17b.

1433 The scale factor is measured to be $\epsilon_e^{\text{data}}/\epsilon_e^{\text{MC}} = 0.994 \pm 0.002(\text{stat.}) \pm 0.035(\text{syst.})$.
1434 Four main sources of systematic error, in addition to the statistical error of 0.2%, were
1435 studied.

1436 **Different behavior of electrons and photons in MC** Even though the photon
1437 ID cuts are designed to be similarly efficient for both electrons and photons,
1438 there might be a small difference in the performance between the two kinds
1439 of particles, e.g. because of electron bremsstrahlung. To check this effect, the
1440 MC electron ID efficiency was calculated using a $Z \rightarrow ee$ sample and the MC
1441 photon ID efficiency was calculated using a $\gamma + \text{jets}$ sample. Both samples were

Official
result
uses this
syst.
error, so
I am not
recheck-
ing
it

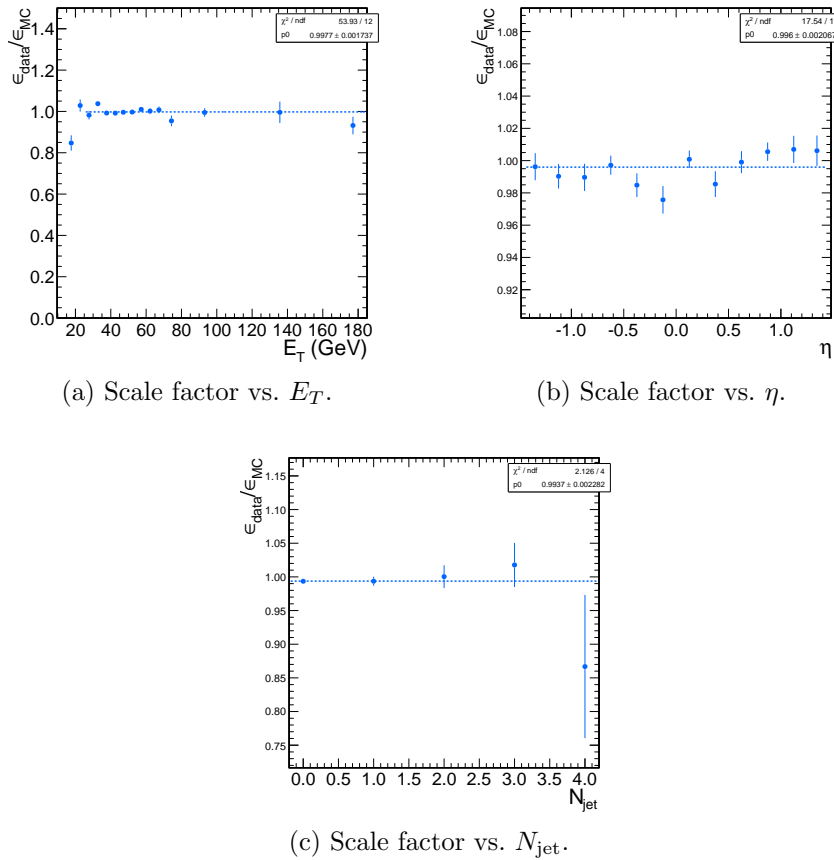


Figure 4.16: Dependence of the photon ID efficiency scale factor on some kinematic variables. Errors are statistical only.

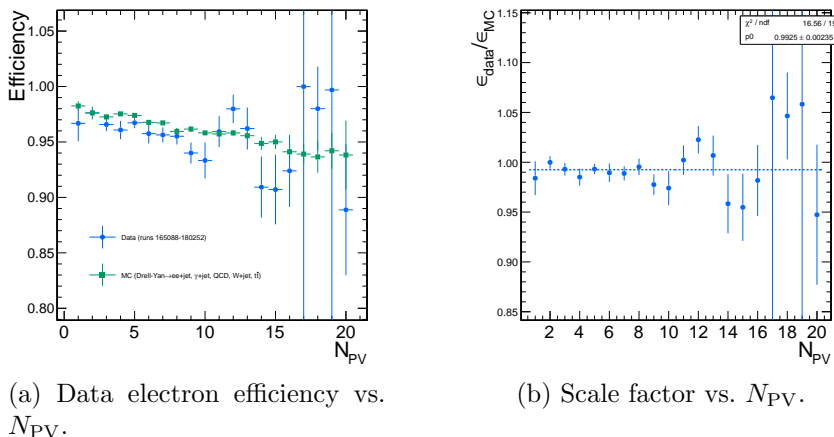


Figure 4.17: Dependence of the photon ID efficiency scale factor on the number of primary vertices per event. Errors are statistical only.

1442 reconstructed in CMSSWv3.6. Half the difference between these two results,
 1443 0.5%, was taken as an error on the scale factor.

Corrected

1444 **Pileup** To account for the possibility that the MC simulation may not adequately some of
 1445 reproduce the data in a high pileup environment, the data/MC scale factor these
 1446 for events with 1-4 good reconstructed primary vertices was calculated, along bullets
 1447 with the same for events with ≥ 5 good reconstructed primary vertices. The
 1448 difference between the scale factors from both samples, 2.4%, was taken as an
 1449 error on the scale factor from pileup.

1450 **Signal fit over/underestimation** It was found that the signal fit slightly under-
 1451 estimates the data in the tag-pass sample, and slightly overestimates it in the
 1452 tag-fail sample. To cover this effect with a systematic error, the efficiencies in
 1453 data and MC, and then the scale factor, were recalculated using the background
 1454 (from fit) subtracted integrals of the tag-pass and tag-fail distributions, rather
 1455 than the fitted signal yields in those distributions. The difference between the
 1456 scale factor found in this way and the nominal scale factor, 1.9%, was taken as
 1457 an error on the scale factor.

1458 **Signal and background shape assumption** To assess the magnitude of the error
 1459 from the signal and background shape assumptions, the tag-pass and tag-fail
 1460 tail parameters (Crystal Ball α and n) were varied by $\pm 1\sigma$, and the background
 1461 shape was varied between `RooCMSShape`, exponential, power law, and quadratic.
 1462 All possible combinations of varied parameters were generated, and the data and
 1463 MC were refit and new scale factors generated according to those combinations.
 1464 The error was taken as the largest deviation of the scale factor from nominal,
 1465 1.8%.

1466 Finally, the pixel veto efficiency was estimated from MC to be 0.96 ± 0.005 (syst.),
 1467 with error due to varying assumptions of the tracker material distribution [98].

¹⁴⁶⁸

Chapter 5

¹⁴⁶⁹

Data Analysis

¹⁴⁷⁰ The signature of GGM SUSY particle production in this search is an excess of two-
¹⁴⁷¹ photon events with high \cancel{E}_T . \cancel{E}_T is reconstructed using the particle flow algorithm
¹⁴⁷² as described in Sec. 4.1.3. Candidate two-photon events, as well as control events,
¹⁴⁷³ are selected according to the offline object criteria presented in Secs. 4.1.1, 4.1.2,
¹⁴⁷⁴ and 4.1.3; the event quality criteria in Sec. 4.3; and the trigger requirements in Sec. 4.2.
¹⁴⁷⁵ These are summarized in Table 5.1.

Table 5.1: Selection criteria for $\gamma\gamma$, $e\gamma$, ee , and ff events.

Variable	Cut			
	$\gamma\gamma$	$e\gamma$	ee	ff
HLT match	IsoVL	IsoVL	IsoVL	IsoVL R9Id
E_T	$> 40/$ $> 25 \text{ GeV}$			
SC $ \eta $	< 1.4442	< 1.4442	< 1.4442	< 1.4442
H/E	< 0.05	< 0.05	< 0.05	< 0.05
$R9$	< 1	< 1	< 1	< 1
Pixel seed	No/No	Yes/No	Yes/Yes	No/No
I_{comb} , $\sigma_{inj\eta}$	$< 6 \text{ GeV} \&\&$ < 0.011	$< 6 \text{ GeV} \&\&$ < 0.011	$< 6 \text{ GeV} \&\&$ < 0.011	$< 20 \text{ GeV} \&\&$ $(\geq 6 \text{ GeV} \parallel$ $\geq 0.011)$
JSON	Yes	Yes	Yes	Yes
No. good PVs	≥ 1	≥ 1	≥ 1	≥ 1
ΔR_{EM}	> 0.6	> 0.6	> 0.6	> 0.6
$\Delta\phi_{\text{EM}}$	≥ 0.05	≥ 0.05	≥ 0.05	≥ 0.05

1476 This search utilizes 4.7 fb^{-1} of CMS data collected during the period April
1477 December 2011, corresponding to the following datasets [99]:

- 1478 • `/Photon/Run2011A-05Jul2011ReReco-ECAL-v1/AOD`
- 1479 • `/Photon/Run2011A-05Aug2011-v1/AOD`
- 1480 • `/Photon/Run2011A-03Oct2011-v1/AOD`
- 1481 • `/Photon/Run2011B-PromptReco-v1/AOD`

1482 The search strategy is to model the backgrounds to the GGM SUSY signal using
1483 \cancel{E}_T shape templates derived from the control samples, and then to look for a high- \cancel{E}_T
1484 excess above the estimated background in the $\gamma\gamma$ sample. There are two categories
1485 of backgrounds: QCD processes with no real \cancel{E}_T and electroweak processes with real
1486 \cancel{E}_T from neutrinos. The relevant QCD background processes are multijet production
1487 with at least two jets faking photons, photon + jet production with at least one jet
1488 faking a photon, and diphoton production, and Z production with a radiated photon
1489 where at least one of the Z decay products (typically a jet) fakes a photon. The
1490 relevant electroweak background processes, which are small compared to the QCD
1491 background, involve $W \rightarrow e\nu$ decay with a recoiling jet that fakes a photon or a
1492 real radiated photon (the W may come from the decay of a top quark in $t\bar{t}$ events).
1493 In both cases, the electron is misidentified as a photon due to a small inefficiency
1494 in reconstructing the electron pixel seed. The main diagrams contributing to the
1495 QCD(electroweak) backgrounds are shown in Figure 5.1(5.2).

1496 Data control samples are used to model all of the backgrounds. The primary
1497 control sample used to model the QCD background is the ff sample, which is similar
1498 to the candidate $\gamma\gamma$ sample but with combined isolation or $\sigma_{inj\eta}$ cuts inverted. The cuts
1499 on these variables are used to distinguish between photons and jets, so by inverting
1500 those cuts, the resulting ff sample becomes enriched with QCD dijets. Because the

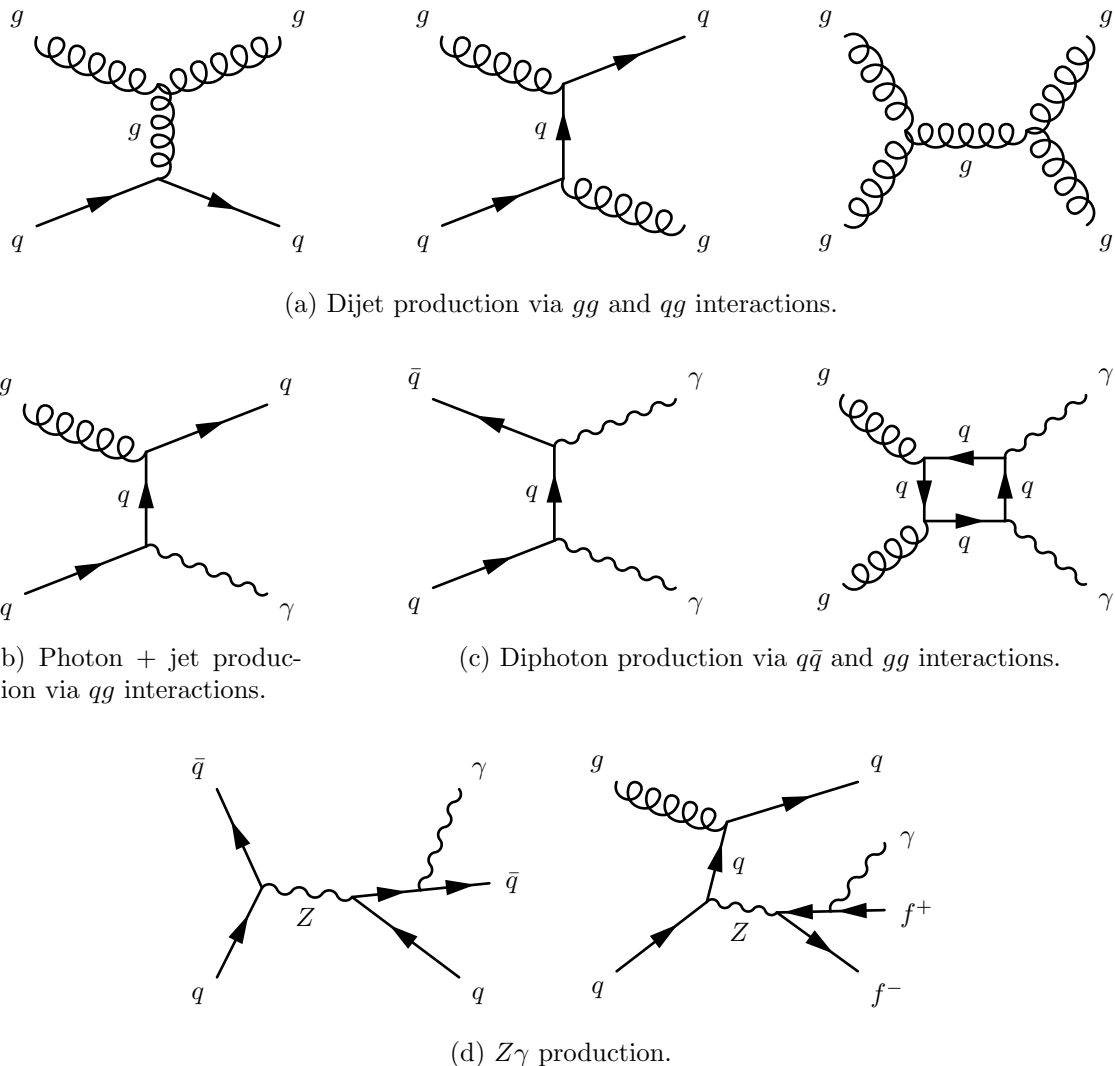


Figure 5.1: Representative Feynman diagrams of some QCD backgrounds to the GGM SUSY search.

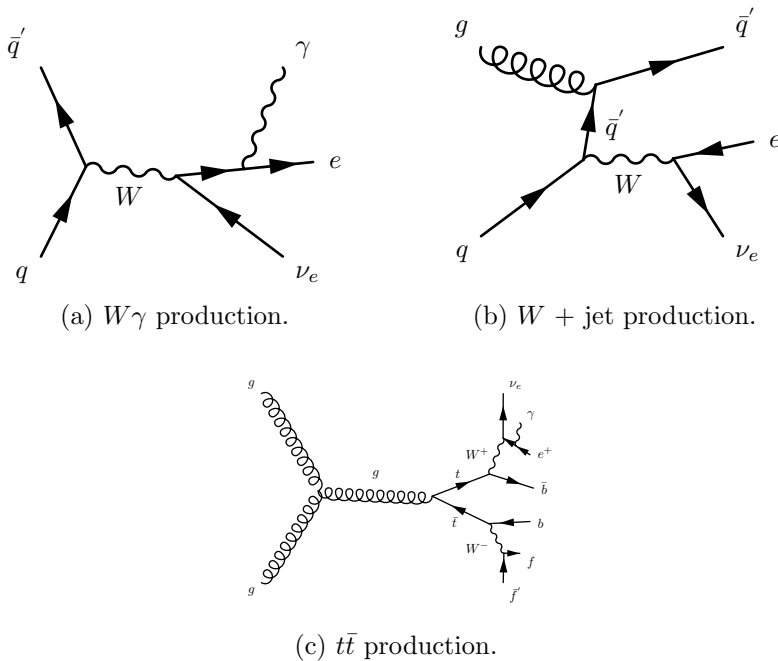


Figure 5.2: Representative Feynman diagrams of some electroweak backgrounds to the GGM SUSY search.

fake photons are still required to pass a tight cut on H/E , they are guaranteed to be very electromagnetic jets, with an EM energy scale and resolution similar to that of the candidate photons. This insures that the resulting estimate of the \cancel{E}_T shape does not have too long of a tail from severe HCAL mis-measurements that are actually rare in the $\gamma\gamma$ sample.

As a cross-check, the ee sample is also used to model the QCD background. This sample of Z decays should have no true \cancel{E}_T , just like the ff sample, and the electron definition (differing from the photon definition only in the presence of a pixel seed) insures that the electron energy scale and resolution is similar to that of the photon.

Finally, the $e\gamma$ sample is used to model the electroweak background from $W \rightarrow e\nu$ decays. The $e\gamma$ \cancel{E}_T distribution is scaled by the electron \rightarrow photon misidentification rate to predict the number of $W\gamma$, $W + \text{jet}$, and $t\bar{t}$ events in the $\gamma\gamma$ sample.

The remainder of this chapter describes the data analysis procedures and the final results of the search. Sec. 5.1 addresses the QCD background estimation. Sec. 5.2

1515 addresses the electroweak background estimation. The chapter concludes with a dis-
 1516 cussion of systematic errors in Sec. 5.3 and a presentation of the final results in
 1517 Sec. 5.4.

1518 5.1 Modeling the QCD Background

1519 5.1.1 Outline of the Procedure

1520 Due to the fact that the CMS ECAL energy resolution is much better than the
 1521 HCAL energy resolution, the energies of the two candidate photons in the events of
 1522 the $\gamma\gamma$ sample are typically measured to far greater accuracy and precision than the
 1523 energy of the hadronic recoil in those events. Therefore, fake E_T in the $\gamma\gamma$ sample
 1524 is almost entirely the result of hadronic mis-measurement in QCD dijet, photon +
 1525 jet, and diphoton events. The strategy employed to model this background is to find
 1526 a control sample in data consisting of two well-measured EM objects, just like the
 1527 candidate $\gamma\gamma$ sample, and assign each event a weight to account for the underlying
 1528 kinematic differences between the control and candidate samples. Once the reweighted
 1529 E_T spectrum of the control sample is created, it is then normalized in the low- E_T
 1530 region, the assumption being that GGM SUSY does not predict a significant amount
 1531 of events at low E_T . There are three aspects of this QCD background estimation
 1532 procedure that bear highlighting:

1533 **Choice of control sample** Since the underlying cause of E_T in the candidate sam-
 1534 ple is mis-measured hadronic activity, a control sample with similar hadronic
 1535 activity to the candidate sample should be chosen. Hadronic activity refers to
 1536 number of jets, jet E_T , pileup, etc.

1537 **Reweighting** The control sample is reweighted so that its E_T spectrum appears as it
 1538 would if the control sample had the same kinematic properties as the candidate

sample (i.e. particle p_T and η distributions, etc.). By choosing an appropriate control sample and reweighting it, the control \cancel{E}_T distribution should now match both the hadronic activity and the kinematics of the candidate sample.

Normalization Finally, the control E_T distribution is normalized in a region of low \cancel{E}_T , where contamination from the expected GGM SUSY signal is small. This implies an extrapolation of the low- \cancel{E}_T QCD background prediction to the high- \cancel{E}_T signal region.

As explained in the beginning of this chapter, the ff sample is used as the primary QCD control sample, while the ee sample is used as a cross-check. Both samples have two well-measured EM objects per event, no real \cancel{E}_T , and similar hadronic activity to the $\gamma\gamma$ sample. Figure 5.3 shows a comparison of the shapes of some distributions relevant to hadronic activity between the $\gamma\gamma$, ee , and ff samples. In general, the ee sample has less hadronic activity than the $\gamma\gamma$ and ff samples, as shown by the more steeply falling ee distributions in Figs. 5.3a, 5.3b, 5.3c, and 5.3d. In addition to the kinematic reweighting, there is also a reweighting by number of jets per event, which attempts to correct for this difference (see Sec. 5.1.2).

5.1.2 Reweighting

To reweight the control sample events to match the kinematics of the candidate sample events, a weight based on the p_T of the di-EM-object system and the number of jets in the event is used. As explained in Sec. 5.1.1, E_T in the $\gamma\gamma$, ff , and ee samples is due to the poorly measured hadronic recoil off the well-measured di-EM system. Therefore, the p_T of the di-EM system is a good handle on the true magnitude of the hadronic recoil, which affects the measured \cancel{E}_T . The di-EM system is depicted in Figure 5.4. As shown in Figure 5.5, \cancel{E}_T is largely uncorrelated with di-EM p_T , so there is little danger of reweighting away a true signal excess.

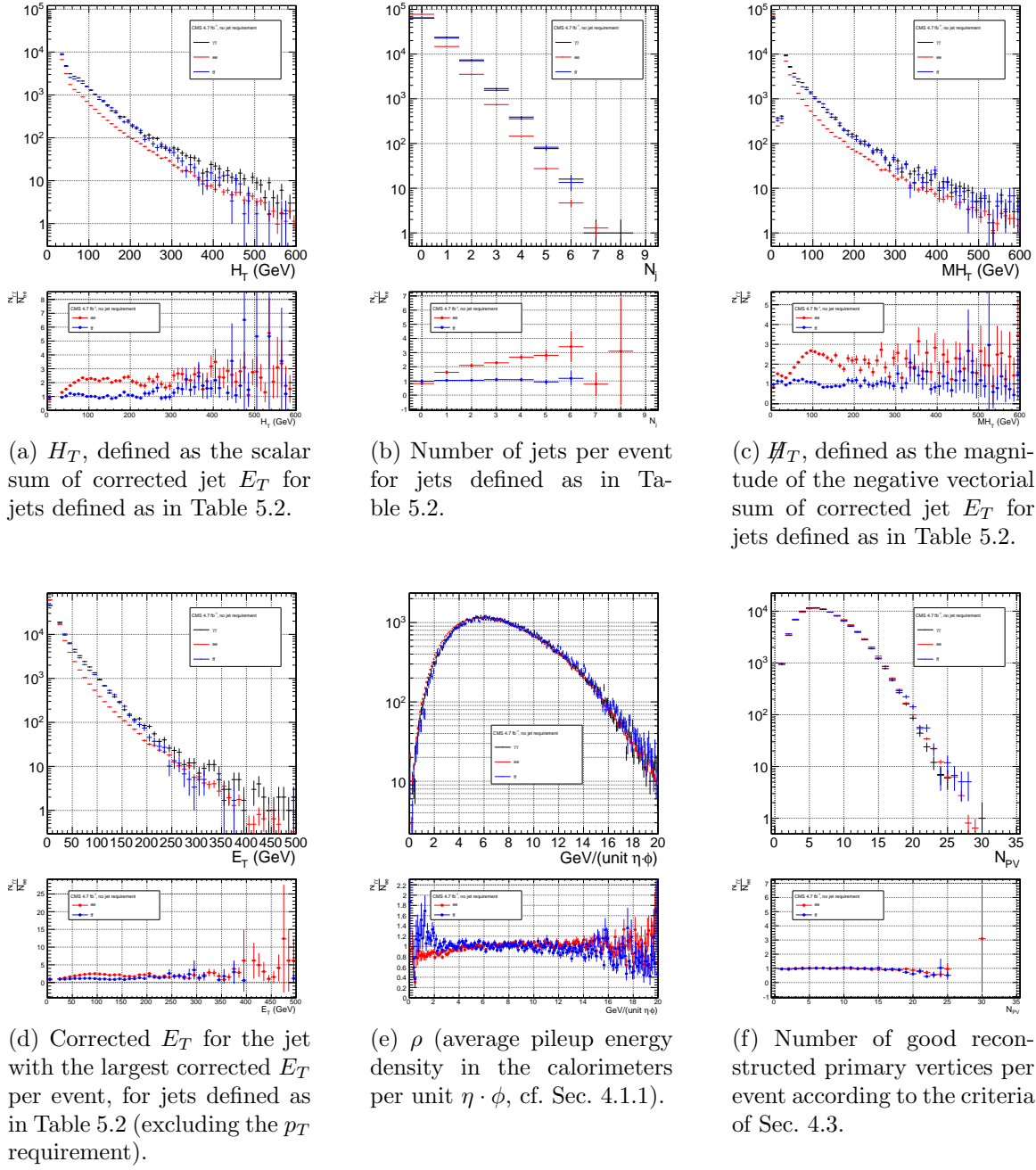


Figure 5.3: Comparison of the shapes of some distributions relevant to hadronic activity between the $\gamma\gamma$, ee ($81 \text{ GeV} \leq m_{ee} < 101 \text{ GeV}$), and ff samples. The ee and ff distributions are normalized to the number of events in the $\gamma\gamma$ distribution. Errors are statistical only.

Table 5.2: Definition of HB/HE/HF hadronic jets.

Variable	Cut
Algorithm	L1FastL2L3Residual corrected PF (cf. Sec. 4.1.3)
p_T	$> 30 \text{ GeV}$
$ \eta $	< 5.0
Neutral hadronic energy fraction	< 0.99
Neutral electromagnetic energy fraction	< 0.99
Number of constituents	> 1
Charged hadronic energy	$> 0.0 \text{ GeV}$ if $ \eta < 2.4$
Number of charged hadrons	> 0 if $ \eta < 2.4$
Charged electromagnetic energy fraction	< 0.99 if $ \eta < 2.4$
ΔR to nearest PF electron ^a , muon ^b , or one of the two primary EM objects	> 0.5

^aA PF electron is defined as an electron reconstructed with the PF algorithm [75] with $p_T > 15 \text{ GeV}$, $|\eta| < 2.6$, and $(I_{\text{charged}} + I_{\text{photon}} + I_{\text{neutral}})/p_T < 0.2$, where $I_{\text{charged}}(I_{\text{photon}})(I_{\text{neutral}})$ is the sum of PF charged hadron(PF photon)(PF neutral hadron) momenta in a $\Delta R = 0.4$ cone around the PF electron.

^bMuons are reconstructed [76] from a combination of muon station and inner tracker hits. Here, a muon must have track $\chi^2 < 10$, at least one good muon station hit, inner track transverse impact parameter $< 0.02 \text{ cm}$, inner track longitudinal impact parameter $< 0.5 \text{ cm}$, $p_T > 15 \text{ GeV}$, $|\eta| < 2.6$, and $(I_{\text{ECAL}} + I_{\text{HCAL}} + I_{\text{track}})/p_T < 0.2$, where $I_{\text{ECAL}}(I_{\text{HCAL}})(I_{\text{track}})$ is the sum of ECAL(HCAL)(track) momenta in a $\Delta R = 0.3$ cone around the muon.

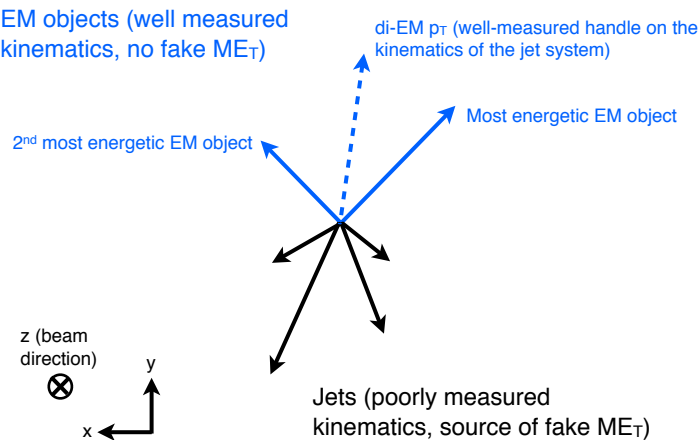


Figure 5.4: Cartoon showing the di-EM system in blue and the hadronic recoil in black. The di-EM p_T (dashed blue line) is used to reweight the control sample kinematic properties to match those of the candidate $\gamma\gamma$ sample.

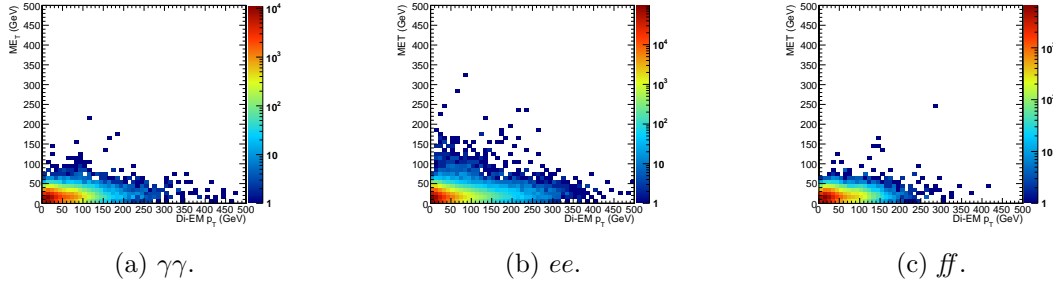


Figure 5.5: E_T vs. di-EM p_T .

Whereas the di-EM p_T reweighting accounts for differences in production kinematics between the control and $\gamma\gamma$ samples, a simultaneous reweighting based on the number of jets in the event accounts for differences in hadronic activity between the samples, especially between ee and $\gamma\gamma$ (cf. Fig. 5.3). Jets are defined as in Table 4.2. Figure 5.6 shows the effect of reweighting by number of jets per event, which is to increase(decrease) the tail of the $ee(ff)$ E_T spectrum.

1570 Although the electron and photon energies are well measured by the ECAL, the
 1571 ECAL-only measurement of the fake photon energy (cf. Sec 4.1.1) is biased slightly
 1572 low due to the fact that fakes (which are really jets) tend to deposit some energy in
 1573 the HCAL. This can be seen in Figs. 5.7 and 5.8, which show the relative difference
 1574 between the ECAL-only E_T measurement and the PF E_T measurement vs. EMF for
 1575 electrons, photons, and fakes. PF E_T is defined as the L1Fast-corrected E_T of the
 1576 nearest PF jet with $p_T \geq 20$ GeV (i.e., the E_T of the PF jet object reconstructed from
 1577 the same ECAL shower as the fake photon). On average, the fakes tend to deposit
 1578 a few percent more energy in the HCAL than the electrons or photons, which is
 1579 recovered by the PF algorithm. For this reason, the PF p_T is used in the calculation
 1580 of di-EM p_T rather than the ECAL-only p_T .¹ This leads to a modest improvement in
 1581 the agreement between the ee and ff E_T spectra, as shown in Figure 5.9.

1582 The control sample event weights are defined as

¹In the few events ($\mathcal{O}(10^{-3})$) in which two PF jet objects, corresponding to the two electrons or fakes, are not found, the ECAL-only p_T is used.

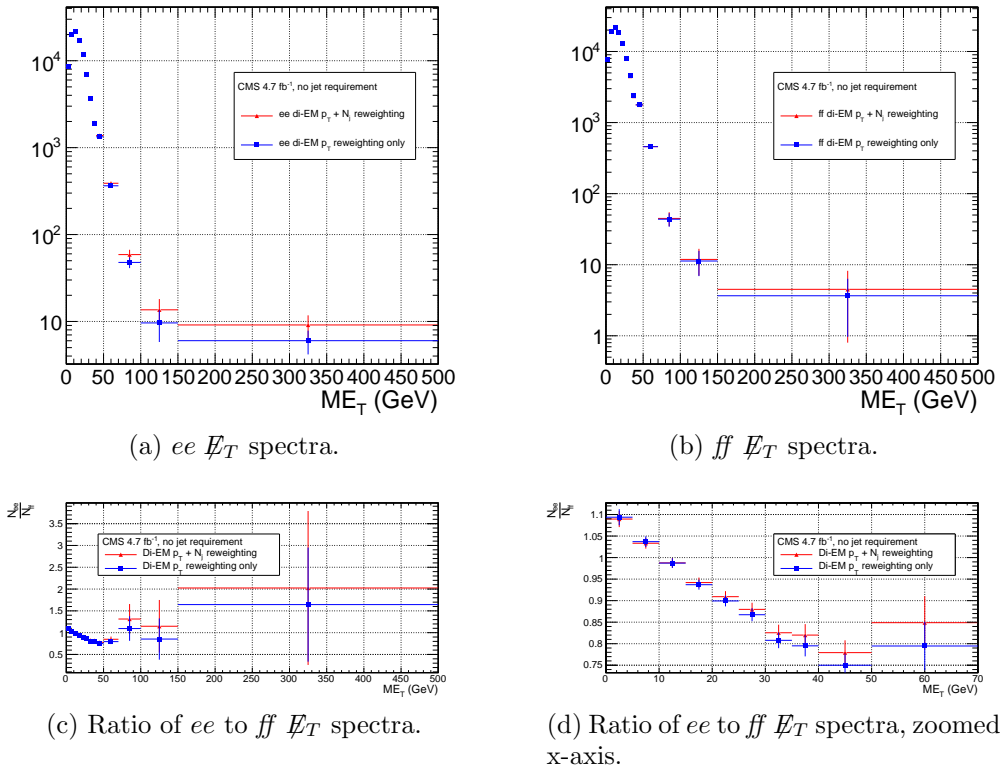


Figure 5.6: \cancel{E}_T spectra of the reweighted ee ($81 \text{ GeV} \leq m_{ee} < 101 \text{ GeV}$) and ff control samples. Blue squares indicate di-EM p_T reweighting only; red triangles indicate di-EM $p_T + \text{number of jets}$ reweighting. PF p_T (cf. p. 112) is used to calculate the di-EM p_T . The full normalization procedure is employed, along with ee sideband subtraction (discussed at the end of this section). Error bars are statistical only.

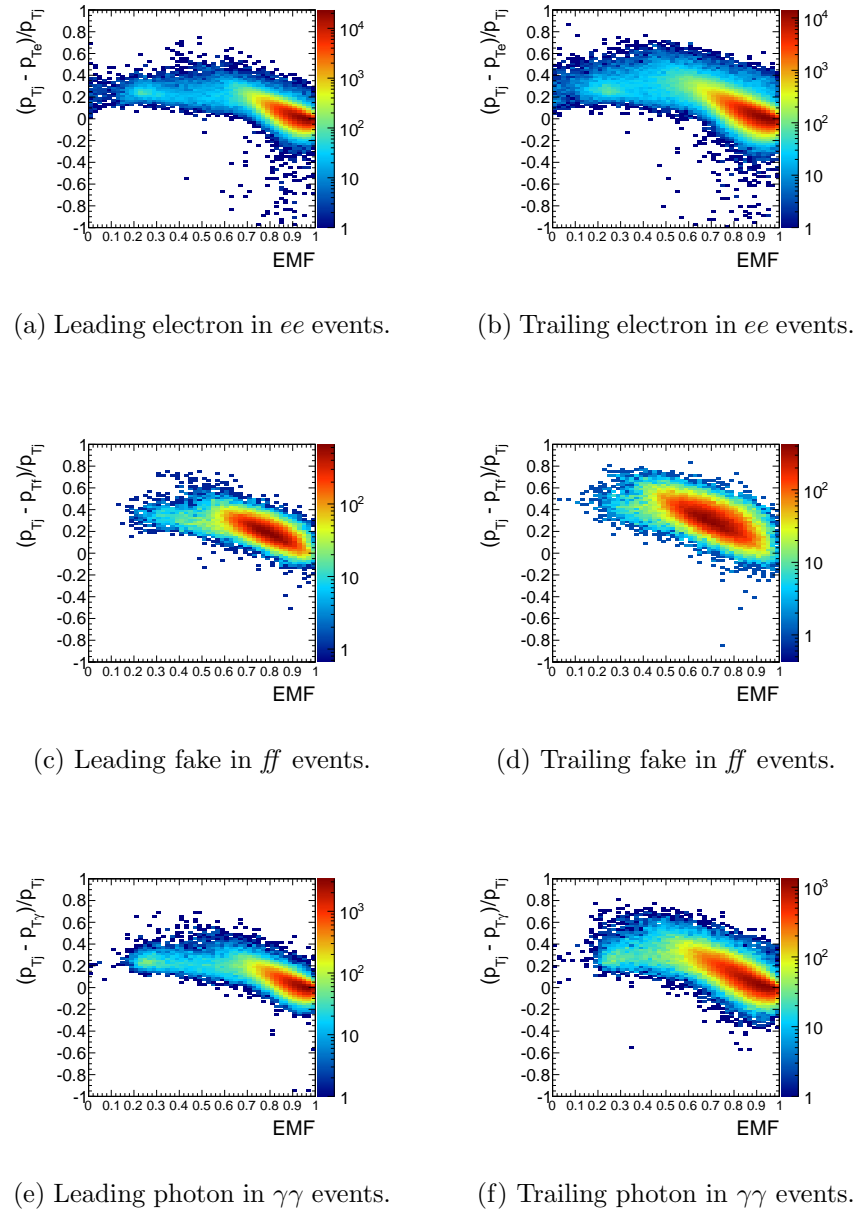


Figure 5.7: Relative difference between the ECAL-only E_T measurement and the PF E_T measurement vs. EMF. PF E_T is defined in the text.

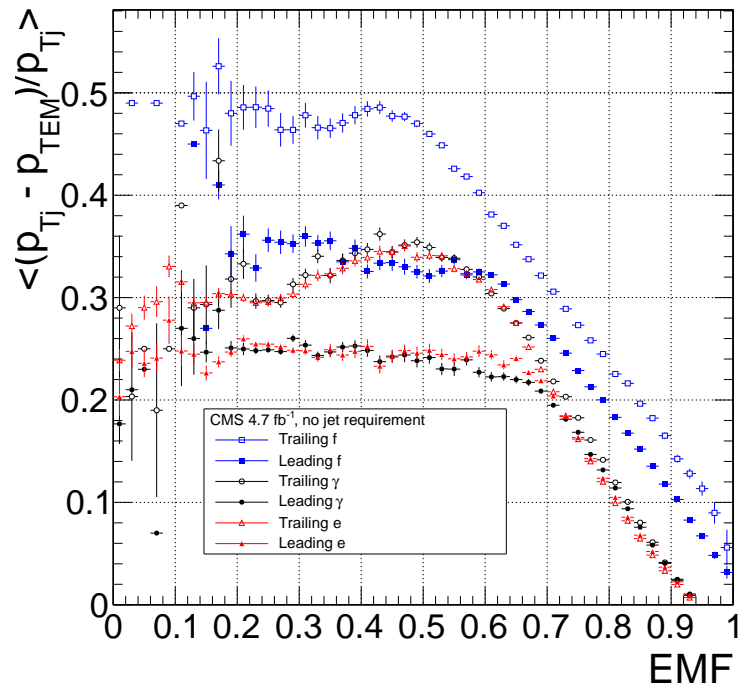


Figure 5.8: Average relative difference between the ECAL-only E_T measurement and the PF E_T measurement vs. EMF for the leading (filled marker) and trailing (open marker) electrons in ee events (red triangles), fakes in ff events (blue squares), and photons in $\gamma\gamma$ events (black circles). These are nothing more than profile histograms of Fig. 5.7. PF E_T is defined in the text. Error bars are statistical only.

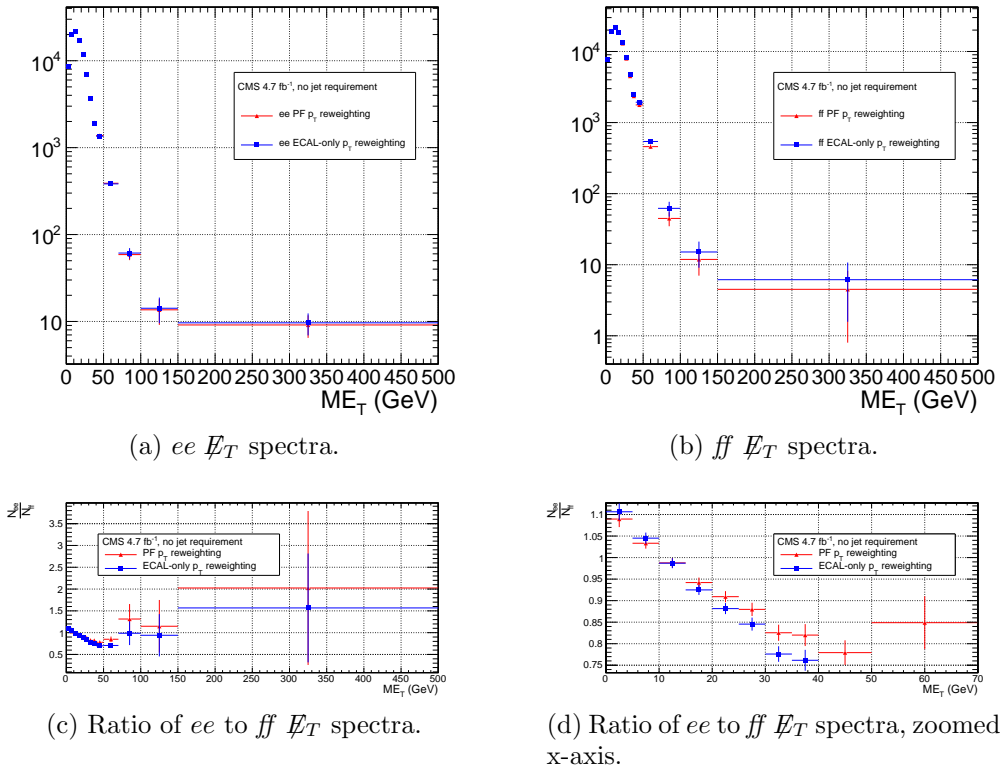


Figure 5.9: E_T spectra of the reweighted ee ($81 \text{ GeV} \leq m_{\text{ee}} < 101 \text{ GeV}$) and ff control samples. Blue squares indicate reweighting using the ECAL-only p_T estimate; red triangles indicate reweighting using the PF p_T estimate. The full reweighting and normalization procedure is employed, along with ee sideband subtraction (discussed at the end of this section). Error bars are statistical only.

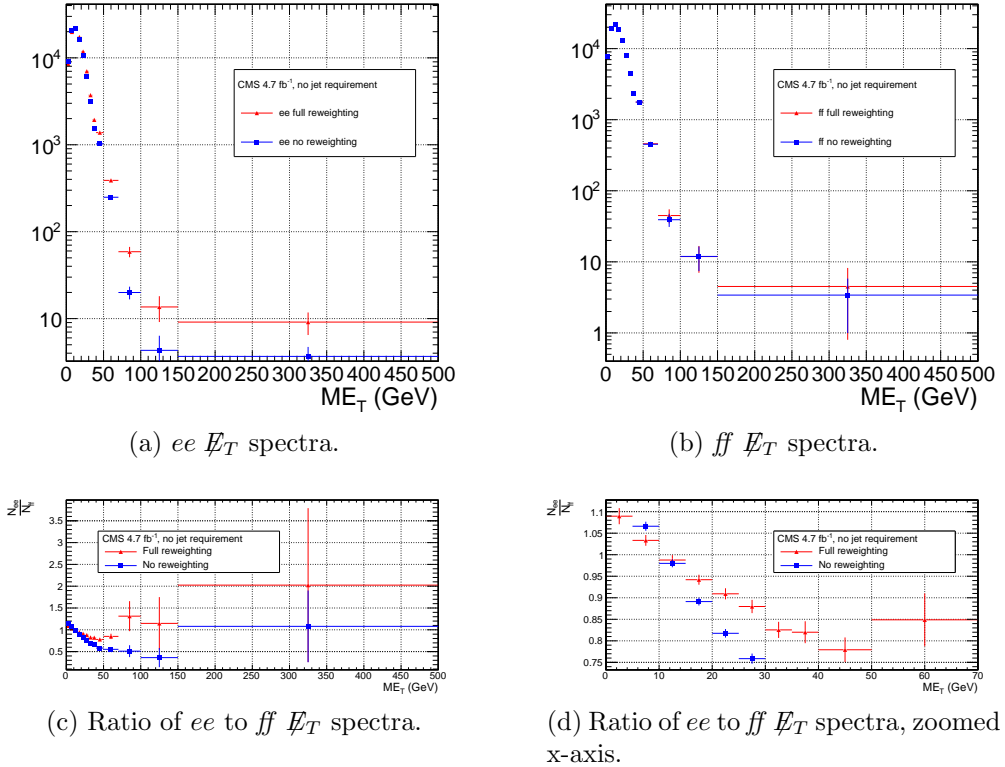


Figure 5.10: \cancel{E}_T spectra of the ee ($81 \text{ GeV} \leq m_{ee} < 101 \text{ GeV}$) and ff control samples. Red triangles indicate full di-EM $p_T +$ number of jets reweighting; blue squares indicate no reweighting. PF p_T (cf. p. 114) is used to calculate the di-EM p_T . The full normalization procedure is employed, along with ee sideband subtraction (discussed at the end of this section). Error bars are statistical only.

$$w_{ij} = \frac{N_{\text{control}}}{N_{\gamma\gamma}} \frac{N_{\gamma\gamma}^{ij}}{N_{\text{control}}^{ij}} \quad (5.1)$$

1583 where i runs over the number of di-EM p_T bins, j runs over the number of jet bins,
 1584 N_{control} is the total number of events in the control sample, $N_{\gamma\gamma}$ is the total number of
 1585 events in the $\gamma\gamma$ sample, $N_{\gamma\gamma}^{ij}$ is the number of $\gamma\gamma$ events in the i^{th} di-EM p_T bin and
 1586 j^{th} jet bin, and N_{control}^{ij} is the number of control sample events in the i^{th} di-EM p_T
 1587 bin and j^{th} jet bin. The effect of the reweighting is more significant for the ee sample
 1588 than for the ff sample, as shown in Figure 5.10.

1589 The ee sample contains a non-negligible background of $t\bar{t}$ events in which both
 1590 W bosons decay to electrons. These events have significant real \cancel{E}_T from the two
 1591 neutrinos (unlike the $\gamma\gamma$ events), and therefore inflate the background estimate at
 1592 high \cancel{E}_T . In order to remove the $t\bar{t}$ contribution from the ee sample, a sideband
 1593 subtraction method is employed.

1594 Only events in the ee sample with $81 \text{ GeV} \leq m_{ee} < 101 \text{ GeV}$, where m_{ee} is the
 1595 di-electron invariant mass, are used in the QCD background estimate. This choice
 1596 maximizes the ratio of Z signal to background. The sidebands used to estimate the
 1597 background contribution within the Z window are defined such that $71 \text{ GeV} \leq m_{ee} <$
 1598 81 GeV and $101 \text{ GeV} \leq m_{ee} < 111 \text{ GeV}$.

1599 The full reweighting procedure is applied to the Z signal region and the two
 1600 sideband regions independently. Only Z signal events are used in the calculation of
 1601 the di-EM p_T weights for the Z signal region, and likewise only the events within
 1602 a given sideband region are used in the calculation of the weights for that region.
 1603 Assuming a constant $t\bar{t}$ background shape, the resulting reweighted sideband \cancel{E}_T
 1604 distributions are added together and subtracted from the reweighted Z signal \cancel{E}_T
 1605 distribution. The sideband subtracted Z signal \cancel{E}_T distribution is then normalized
 1606 as discussed in Secs. 5.1.1 and 5.1.3. The statistical and reweighting error from the
 1607 sideband regions is propagated to the error on the final ee QCD \cancel{E}_T estimate.

1608 The di-EM p_T weights for the two ee sideband regions are shown in Figure 5.11.
 1609 The overall scale of the weights, as well as the trend with di-EM p_T , is similar for
 1610 the two regions (except at high di-EM p_T , where the statistics are poor anyway).
 1611 Figure 5.12 shows the \cancel{E}_T spectra for the two sideband regions and the Z signal
 1612 region after subtraction. The shapes of the spectra indicate that the high- \cancel{E}_T $t\bar{t}$ tail,
 1613 present in the sideband distributions, was successfully subtracted from the Z signal
 1614 distribution.

1615 The ee ($81 \text{ GeV} \leq m_{ee} < 101 \text{ GeV}$), ff , and $\gamma\gamma$ di-EM p_T spectra for events with

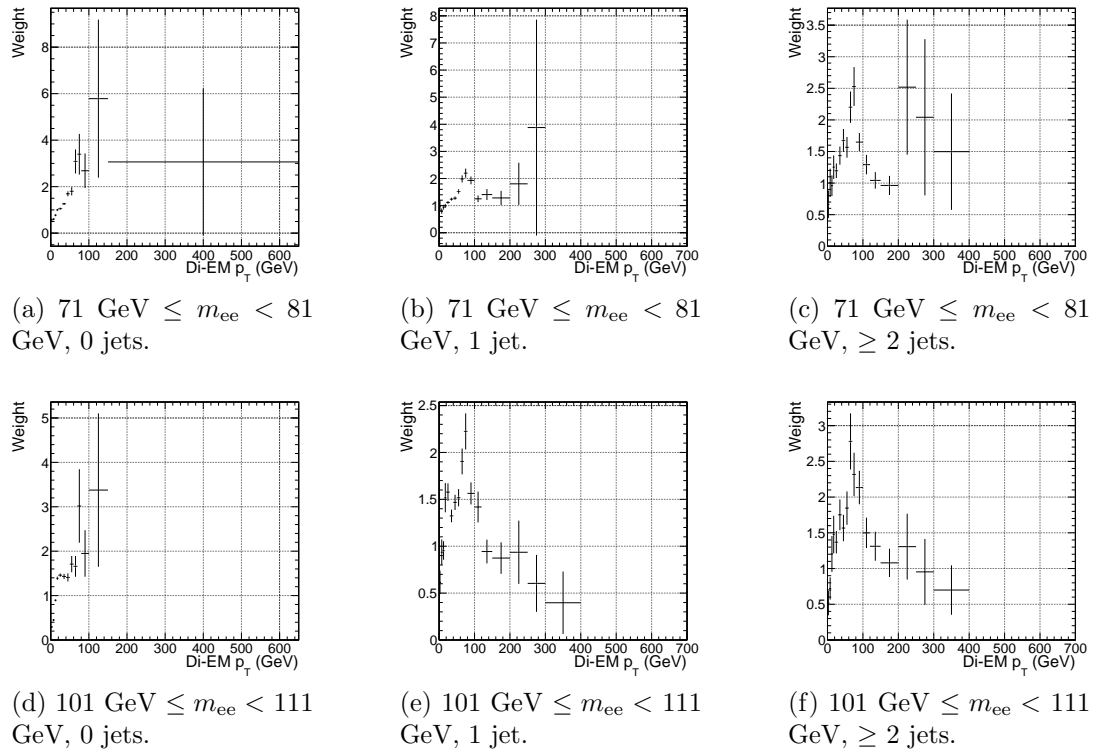


Figure 5.11: ee sideband di-EM p_T weights for events with 0, 1, or ≥ 2 jets (as in Table 4.2). Errors are statistical only.

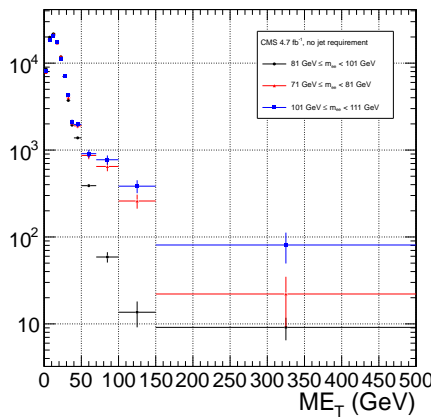


Figure 5.12: E_T spectra of the ee sample for $71 \text{ GeV} \leq m_{ee} < 81 \text{ GeV}$ (red triangles), $81 \text{ GeV} \leq m_{ee} < 101 \text{ GeV}$ (black circles), and $101 \text{ GeV} \leq m_{ee} < 111 \text{ GeV}$ (blue squares). The two sideband distributions (red and blue) and the Z signal distribution (black) are normalized to the total number of $\gamma\gamma$ events. Errors are statistical only.

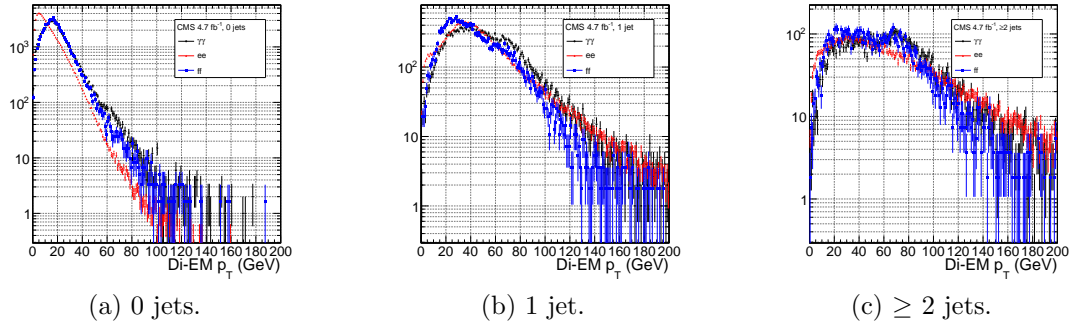


Figure 5.13: ee ($81 \text{ GeV} \leq m_{ee} < 101 \text{ GeV}$) (red triangles), ff (blue squares), and $\gamma\gamma$ (black circles) di-EM p_T spectra for events with 0, 1, or ≥ 2 jets (as in Table 4.2). Errors are statistical only.

¹⁶¹⁶ 0, 1, or ≥ 2 jets (as in Table 4.2) are shown in Figure 5.13. Broad humps in the ff
¹⁶¹⁷ and $\gamma\gamma$ spectra are due to kinematic ΔR and p_T turn-ons that are suppressed in the
¹⁶¹⁸ ee sample due to the invariant mass cut. Figure 5.14 shows the weights applied to
¹⁶¹⁹ the ee ($81 \text{ GeV} \leq m_{ee} < 101 \text{ GeV}$) and ff \cancel{E}_T spectra as a function of di-EM p_T and
¹⁶²⁰ number of jets per event.

1621 5.1.3 Normalization

After reweighting, the \cancel{E}_T distributions of the QCD control samples are normalized to the $\cancel{E}_T < 20$ GeV region of the candidate $\gamma\gamma \cancel{E}_T$ spectrum, where signal contamination is low. The normalization factor is $(N_{\gamma\gamma}^{\cancel{E}_T < 20\text{GeV}} - N_{e\gamma}^{\cancel{E}_T < 20\text{GeV}})/N_{\text{control}}^{\cancel{E}_T < 20\text{GeV}}$, where $N_{e\gamma}^{\cancel{E}_T < 20\text{GeV}}$ is the expected number of electroweak background events with $\cancel{E}_T < 20$ GeV (discussed in Section 5.2).

¹⁶²⁷ 5.2 Modeling the Electroweak Background

¹⁶²⁸ $W\gamma$, $W + \text{jet}$, and $t\bar{t}$ processes in which the W decay electron is misidentified as a
¹⁶²⁹ photon (due to a failure to properly associate a pixel seed to the electron candidate)
¹⁶³⁰ can contribute significantly to the high- E_T tail of the $\gamma\gamma E_T$ spectrum. To estimate

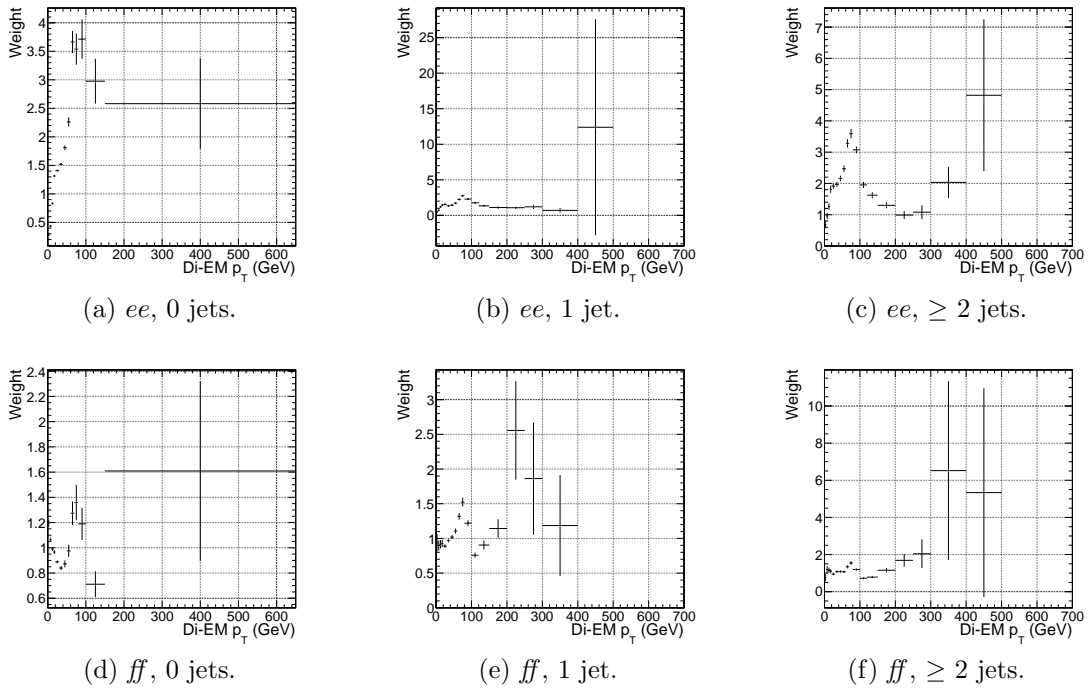


Figure 5.14: ee ($81 \text{ GeV} \leq m_{ee} < 101 \text{ GeV}$) and ff di-EM p_T weights for events with 0, 1, or ≥ 2 jets (as in Table 4.2). Errors are statistical only.

1631 this background, the $e\gamma$ sample, which is enriched in $W \rightarrow e\nu$ decays, is scaled by
 1632 $f_{e \rightarrow \gamma}/(1 - f_{e \rightarrow \gamma})$, where $f_{e \rightarrow \gamma}$ is the rate at which electrons are misidentified as photons.
 1633 The derivation of this scaling factor comes from the two equations

$$N_{e\gamma}^W = f_{e \rightarrow e} N_W \quad (5.2)$$

$$N_{\gamma\gamma}^W = (1 - f_{e \rightarrow e}) N_W \quad (5.3)$$

1634 where $N_{e\gamma}^W$ is the number of W events in the $e\gamma$ sample in which the electron was
 1635 correctly identified, $f_{e \rightarrow e}$ is the probability to correctly identify an electron, N_W is
 1636 the true number of triggered $W \rightarrow e\nu$ events, and $N_{\gamma\gamma}^W$ is the number of W events in
 1637 the $\gamma\gamma$ sample in which the electron was misidentified as a photon. The contribution
 1638 from $Z \rightarrow ee$ can be neglected (i.e. $f_{e \rightarrow \gamma}$ is small and the Z contribution involves
 1639 $f_{e \rightarrow \gamma}^2$, since both electrons have to be misidentified). Since $f_{e \rightarrow e} = 1 - f_{e \rightarrow \gamma}$, solving

1640 for $N_{\gamma\gamma}^W$ gives

$$N_{\gamma\gamma}^W = \frac{f_{e\rightarrow\gamma}}{1 - f_{e\rightarrow\gamma}} N_{e\gamma}^W \quad (5.4)$$

1641 $f_{e\rightarrow\gamma}$ is measured by fitting the Z peaks in the ee and $e\gamma$ samples. The number of
1642 Z events fitted in the ee and $e\gamma$ samples, respectively, is given by

$$N_{ee}^Z = (1 - f_{e\rightarrow\gamma})^2 N_Z \quad (5.5)$$

$$N_{e\gamma}^Z = 2f_{e\rightarrow\gamma}(1 - f_{e\rightarrow\gamma}) N_Z \quad (5.6)$$

1643 where N_Z is the true number of triggered $Z \rightarrow ee$ events. Solving for $f_{e\rightarrow\gamma}$ gives

$$f_{e\rightarrow\gamma} = \frac{N_{e\gamma}^Z}{2N_{ee}^Z + N_{e\gamma}^Z} \quad (5.7)$$

1644 A Crystal Ball function is used to model the Z signal shape in both the ee and
1645 $e\gamma$ samples, while an exponential convoluted with an error function (`RooCMSShape`,
1646 see Sec. 4.4.1) is used to model the background shape. The fixed fit parameters are
1647 identical for the two samples, but the other parameters are allowed to float indepen-
1648 dently. Table 5.3 shows the values and ranges of the fixed and floating fit parameters,
1649 respectively.

1650 Fits to the ee and $e\gamma$ invariant mass spectra are shown in Figure 5.15. Figure 5.16
1651 indicates that the dependence of $f_{e\rightarrow\gamma}$ on the electron p_T and η is small. (Note that all
1652 fit parameters are floating in the p_T -dependent fits.) Therefore, a constant misidenti-
1653 fication rate (derived from all ee and $e\gamma$ events), rather than a p_T - and η -dependent
1654 misidentification rate, is used in the final electroweak background estimate, with the

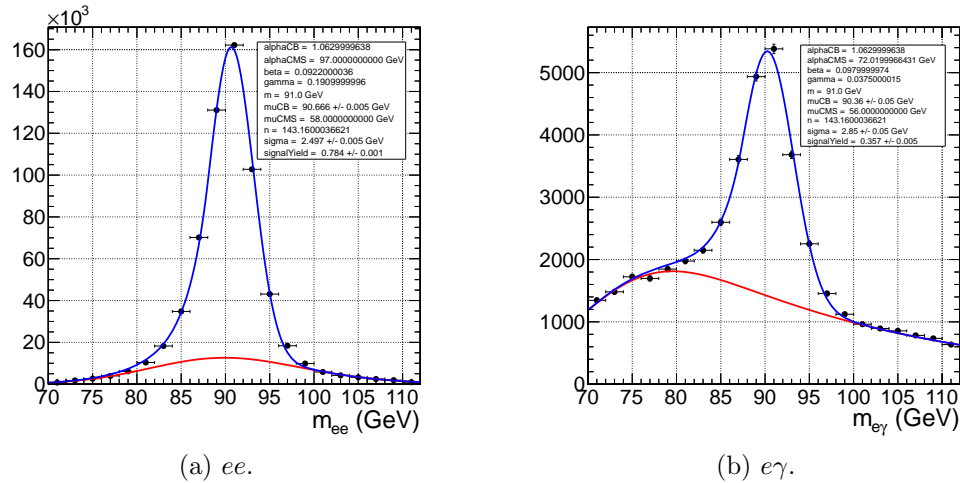


Figure 5.15: Fits to the ee and $e\gamma$ invariant mass spectra using the Crystal Ball RooCMSShape function described in the text and in Table 5.3. The total fit is shown in blue, while the background component is shown in red.

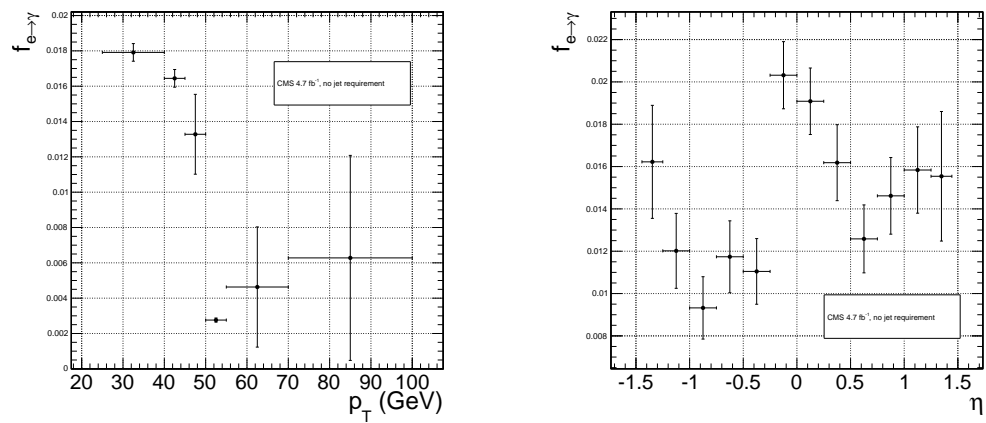
difference between the constant rate and the rate for electrons with p_T between 25 and 40 GeV (the range in which the bulk of the trailing photons in the $\gamma\gamma$ sample lie) taken as a systematic error.

Using the integrals of the Z fits shown in Fig. 5.15, Eq. 5.7, and the p_T systematic discussed above, $f_{e \rightarrow \gamma}$ is calculated to be $0.014 \pm 0.000(\text{stat.}) \pm 0.004(\text{syst.})$. The scaled $e\gamma$ MET distribution is shown in Figure 5.17.

In the 36 pb^{-1} version of this analysis [100], it was shown that the ee sample could accurately predict the QCD and real Z contribution to the $e\gamma$ sample at low \cancel{E}_T , and that the expectation from $W \rightarrow e\nu$ MC accounted for the remaining W contribution at high \cancel{E}_T . A plot of the \cancel{E}_T distributions of the 2010 $e\gamma$ sample and the predicted components is shown in Figure 5.18. This exercise helps to validate both the QCD and electroweak background prediction methods.

Table 5.3: Parameter values for the signal and background PDFs for the ee and $e\gamma$ samples. When a bracketed range is given, the parameter is allowed to float within that range. When a constant is given, the parameter is fixed to that constant.

PDF	Crystal Ball fit parameters				RooCMSShape fit parameters			
	μ	σ	α	n	μ	α	β	γ
ee signal	[86.2, 96.2]	[1.0, 5.0]	1.063	143.16	N/A	N/A	N/A	N/A
$e\gamma$ signal	[86.2, 96.2]	[1.0, 5.0]	1.063	143.16	N/A	N/A	N/A	N/A
ee background	N/A	N/A	N/A	N/A	58	97.0	0.0922	0.191
$e\gamma$ background	N/A	N/A	N/A	N/A	56	72.02	0.098	0.0375



(a) $f_{e \rightarrow \gamma}$ vs. electron p_T . For the lowest p_T bin, the fit to the $e\gamma$ spectrum does not converge well, so the Z signal fraction is fixed to the value in Fig. 5.15b.

(b) $f_{e \rightarrow \gamma}$ vs. electron η .

Figure 5.16: $f_{e \rightarrow \gamma}$ vs. electron p_T and η .

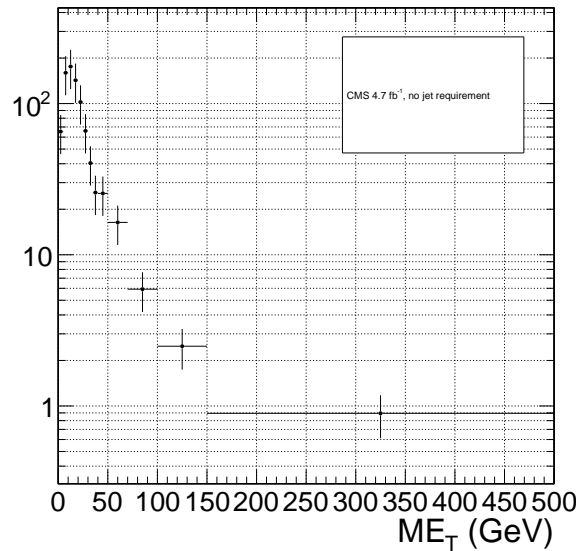


Figure 5.17: \cancel{E}_T spectrum of the $e\gamma$ sample after scaling by $f_{e \rightarrow \gamma}$. The total error on $f_{e \rightarrow \gamma}$ is propagated to the total error on the electroweak background estimate.

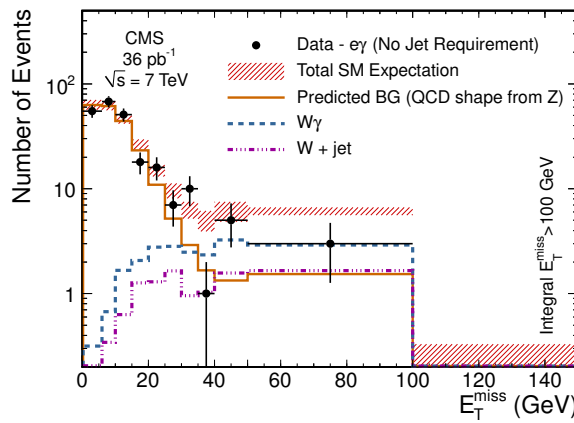


Figure 5.18: \cancel{E}_T spectrum of the $e\gamma$ sample in 35 pb⁻¹ of 2010 LHC data scaled by the 2010 measured $f_{e \rightarrow \gamma}$ (black dots), QCD and real Z predicted background from the 2010 ee sample (solid orange line), MC $W + \text{jet}$ estimate (dash-dotted purple line), and MC $W\gamma$ estimate (dashed blue line). The total $e\gamma$ prediction (red band) is the sum of the ee , $W + \text{jet}$, and $W\gamma$ predictions. Reprinted from Fig. 2 of ref. [100].

1667 5.3 Errors on the Background Prediction

1668 The statistical error on the final background estimate in a particular \cancel{E}_T bin comes
 1669 from three sources: the number of control sample events collected in that bin, the
 1670 statistical error on the weights applied to events in that bin, and the statistics of the
 1671 normalization region. In the case of the ee control sample, there are contributions
 1672 from the statistics of the m_{ee} sidebands as well.

1673 In order to estimate the statistical error due to the reweighting procedure, 1000
 1674 toy sets of weights are generated. Each set includes a weight for each (di-EM p_T , N_j)
 1675 bin, with the values picked from a Gaussian distribution with mean and standard
 1676 deviation equal to the observed weight for that bin and its statistical error. The effect
 1677 of reweighting error is not correlated between \cancel{E}_T bins. For each of the 1000 exper-
 1678 iments, the control sample data are reweighted according to the generated weights,
 1679 and the background estimates are calculated for each \cancel{E}_T bin. Since the distribution
 1680 of the toy background estimates follows a Gaussian distribution in each \cancel{E}_T bin, the
 1681 RMS spread of the estimates is taken as the statistical error due to reweighting. This
 1682 procedure is carried out for the ff , ee , low sideband ee , and high sideband ee samples.

1683 The total statistical error on the background estimate per \cancel{E}_T bin is given by

$$\sigma_{\text{stat}}^2 = \sigma_{\text{stat,QCD}}^2 + \sigma_{\text{stat,EW}}^2 \quad (5.8)$$

1684 where $\sigma_{\text{stat,QCD}}^2$ is the square of the total statistical error on the QCD prediction in
 1685 the \cancel{E}_T bin

$$\sigma_{\text{stat,QCD}}^2 = \sigma_{\text{stat},s}^2 + \sigma_{\text{Poisson,QCD}}^2 + \sigma_{\text{reweight},s}^2 + \sigma_{\text{reweight,QCD}}^2 \quad (5.9)$$

1686 and $\sigma_{\text{stat,EW}}$ is the Poisson error on the number of $e\gamma$ events in the \cancel{E}_T bin ($= \sqrt{N_{e\gamma}}$,
 1687 where $N_{e\gamma}$ is the prediction in the \cancel{E}_T bin after scaling by $f_{e\rightarrow\gamma}$). The contributions
 1688 to $\sigma_{\text{stat,QCD}}^2$ are discussed below.

1689 • $\sigma_{\text{stat},s}^2$ is the statistical error contributed by the normalization factor s (i.e. from
 1690 Poisson error in the normalization region $\cancel{E}_T < 20$ GeV):

$$\begin{aligned}\sigma_{\text{stat},s}^2 = & \frac{N_{\text{control}}^2}{(N_{\gamma\gamma}^{\text{norm}} - N_{e\gamma}^{\text{norm}})^2} (\sigma_{\text{Poisson},\gamma\gamma}^{\text{norm}})^2 + (\sigma_{\text{Poisson},e\gamma}^{\text{norm}})^2 + \\ & \frac{N_{\text{control}}^2}{(N_{\text{control}}^{\text{norm}})^2} (\sigma_{\text{Poisson,control}}^{\text{norm}})^2\end{aligned}\quad (5.10)$$

1691 where N_{control} is the number of reweighted, normalized events in the \cancel{E}_T bin,
 1692 $N_{\gamma\gamma}^{\text{norm}}$ is the number of $\gamma\gamma$ events in the normalization region, $N_{e\gamma}^{\text{norm}}$ is the num-
 1693 ber of $e\gamma$ events in the normalization region (after scaling by $f_{e\rightarrow\gamma}$), $\sigma_{\text{Poisson},\gamma\gamma}^{\text{norm}}$
 1694 is the Poisson error on the number of $\gamma\gamma$ events in the normalization region
 1695 ($= \sqrt{N_{\gamma\gamma}^{\text{norm}}}$), $\sigma_{\text{Poisson},e\gamma}^{\text{norm}}$ is the Poisson error on the number of $e\gamma$ events in the
 1696 normalization region ($= \sqrt{N_{e\gamma}^{\text{norm}}}$), $N_{\text{control}}^{\text{norm}}$ is the number of QCD control (ee
 1697 or ff) events in the normalization region, and $\sigma_{\text{Poisson,control}}^{\text{norm}}$ is the Poisson error
 1698 on the number of QCD control (ee or ff) events in the normalization region
 1699 ($= \sqrt{\sum_{i=1}^{N_{\text{control}}^{\text{norm}}} w_i^2}$, where w_i is the di-EM p_T weight applied to event i). For
 1700 the ee control region, N_{control} and $N_{\text{control},\text{norm}}$ are sideband subtracted, and
 1701 $\sigma_{\text{Poisson,control}}^{\text{norm}}$ includes the Poisson error on the number of sideband events.

- 1702 • $\sigma_{\text{Poisson,QCD}}$ is the Poisson error due to the number of QCD control (ee or ff)
 1703 events in the \cancel{E}_T bin, equal to $\sqrt{\sum_{i=1}^{N_{\text{control}}^{\text{norm}}} w_i^2}$, where w_i is the di-EM p_T weight
 1704 applied to event i . For the ee control region, $\sigma_{\text{Poisson,QCD}}$ includes the Poisson
 1705 error on the number of subtracted sideband events.
- 1706 • $\sigma_{\text{reweight},s}$ is the error contributed by the control sample reweighting in the nor-

1707 malization region ($= \frac{N_{\text{control}}^2}{(N_{\text{control}}^{\text{norm}})^2} \sigma_{\text{reweight,control}}^{\text{norm}}$). $\sigma_{\text{reweight,control}}^{\text{norm}}$ is the quadrature
 1708 sum of the RMS of the 1000 toy reweighting experiments for each \cancel{E}_T bin in the
 1709 normalization region. For the ee control sample, it also includes (in quadrature)
 1710 the RMS of the toys in the sideband samples.

- 1711 • $\sigma_{\text{reweight,QCD}}$ is the error contributed by the control sample reweighting in the \cancel{E}_T
 1712 bin ($= s\sigma_{\text{reweight,control}}$). $\sigma_{\text{reweight,control}}$ is the RMS of the 1000 toy reweighting
 1713 experiments for the E_T bin. For the ee control sample, it also includes (in
 1714 quadrature) the RMS of the toys in the sideband samples.

1715 The dominant source of systematic error on the background estimate is the slight
 1716 difference in hadronic activity between the ee , ff , and $\gamma\gamma$ samples. This results in a
 1717 small bias (~ 1 GeV) of the ee \cancel{E}_T distribution towards lower values with respect to
 1718 the ff and $\gamma\gamma$ samples, as shown in Figure 5.19. Therefore, the ff sample is used as
 1719 the primary QCD background estimator, and the difference between the ee and ff
 1720 predictions is assigned as an error on the knowledge of the hadronic activity. For \cancel{E}_T
 1721 > 100 GeV, this error amounts to 43% of the total QCD + electroweak background
 1722 estimate.

1723 The second largest source of systematic error comes from the p_T dependence of the
 1724 $e \rightarrow \gamma$ misidentification rate (see 5.2). For $\cancel{E}_T > 100$ GeV, the expected electroweak
 1725 background is 3.4 ± 1.0 events, so this error amounts to 4.8% of the total QCD +
 1726 electroweak background estimate.

1727 The assumption of a constant $t\bar{t}$ and $W + \text{jets}$ background shape under the Z
 1728 peak in the ee sample induces a systematic error on the ee sideband-subtracted back-
 1729 ground prediction. To assess the magnitude of this error, the sideband subtraction
 1730 (see Sec. 5.1.2) is performed once using only the prediction from the high sideband,
 1731 and once using only the prediction from the low sideband. In each of these cases, the
 1732 prediction is weighted by a factor of two, to account for the fact that the sideband
 1733 regions are only half as wide (10 GeV) as the signal region (20 GeV). The maximum

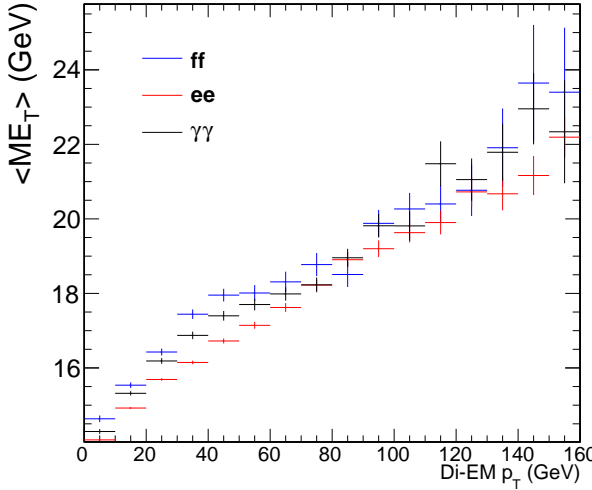


Figure 5.19: Average E_T vs. di-EM p_T for the ff (blue), ee (red), and $\gamma\gamma$ (black) samples.

1734 variation from the nominal ee estimate is taken as the error, which amounts to 11%
 1735 for $E_T > 100$ GeV. E_T distributions using the nominal ee sideband subtraction, the
 1736 low-sideband-only subtraction, and the high-sideband-only subtraction are shown in
 1737 Figure 5.20.

Added

1738 Finally, the few percent error on the jet energy correction factors introduces an this
 1739 error on the final background estimate through (a) the use of the PF p_T to measure para-
 1740 the di-EM p_T , (b) the counting of jets passing a 30 GeV p_T threshold for placement of graph
 1741 the event in an N_j bin for reweighting, and (c) the counting of jets above threshold for
 1742 the ≥ 1 -jet version of the selection. To estimate this error, 100 pseudo-experiments
 1743 are generated with identical properties as the true data sample, except with corrected
 1744 jet energies (in all events) all shifted by an amount $r\sigma(p_T, \eta)$. r is a random number
 1745 drawn from a Gaussian distribution with mean 0 and width 1, and $\sigma(p_T, \eta)$ is the
 1746 uncertainty on the jet energy correction factor (which, like the correction factor itself,
 1747 is a function of p_T and η). The same factor r is applied to all jets in all events in the
 1748 pseudo-experiment because the jet energy correction errors are correlated from jet to
 1749 jet (they result from e.g. uncertainties in MC simulation or uncertainties in ECAL

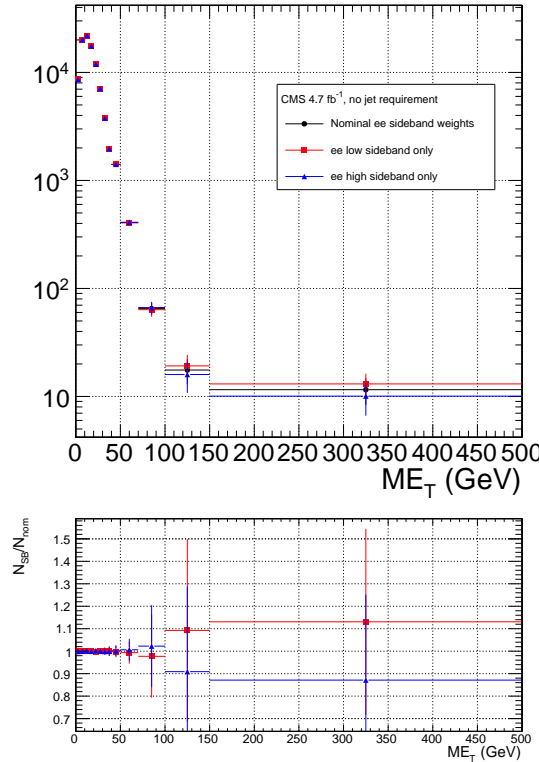


Figure 5.20: ee E_T distributions using the nominal sideband subtraction (black circles), low sideband only (red squares), and high sideband only (blue triangles). The bottom plot shows the ratio of the low sideband distribution to the nominal (red squares) and the ratio of the high sideband distribution to the nominal (blue triangles).

1750 energy scale [80]). The standard error of the mean of the 100 resulting background
1751 estimates in each relevant E_T bin is taken as the error. The error in each E_T bin is
1752 assumed to be uncorrelated. This process is repeated for both the inclusive and ≥ 1 -
1753 jet selections. For $E_T \geq 100$ GeV, the jet energy correction uncertainty is 1.5% (2.2%)
1754 of the total background for the inclusive (≥ 1 -jet) selection.

1755 The uncertainty in how to define the (di-EM p_T , N_j) bins, especially at high di-
1756 EM p_T where the statistics are low, is covered by the 1000-toys procedure as long as
1757 the bins are not too coarse. This is shown in Figure 5.21. If the bins are too coarse,
1758 the details of the shape of the di-EM p_T spectra are lost, and the reweighting has a
1759 smaller effect.

1760 The use of uncorrected instead of corrected PF E_T (see Sec. 4.1.3) makes no

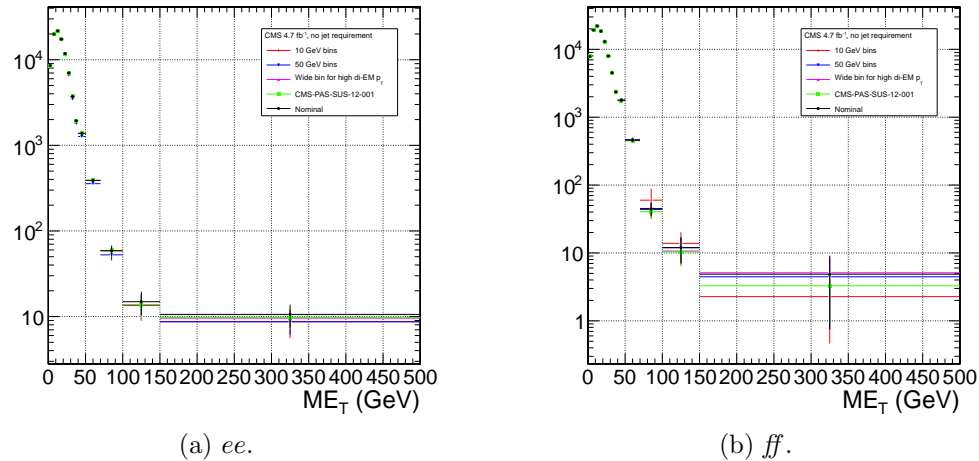


Figure 5.21: Comparison of \cancel{E}_T distributions for five different di-EM p_T bin definitions: uniform bins of width 10 GeV (red diamonds); uniform bins of width 50 GeV (blue downward-pointing triangles); bins with lower edges $\{0.0, 5.0, 10.0, 15.0, 20.0, 30.0, 40.0, 50.0, 60.0, 70.0, 80.0, 100.0, 750.0\}$ GeV for 0-jet events and $\{0.0, 5.0, 10.0, 15.0, 20.0, 30.0, 40.0, 50.0, 60.0, 70.0, 80.0, 100.0, 150.0\}$ GeV for ≥ 1 -jet events (magenta upward-pointing triangles), i.e. a single wide bin at high di-EM p_T ; bins with lower edges $\{0.0, 5.0, 10.0, 15.0, 20.0, 30.0, 40.0, 50.0, 60.0, 70.0, 80.0, 100.0, 150.0\}$ GeV for 0-jet events and $\{0.0, 5.0, 10.0, 15.0, 20.0, 30.0, 40.0, 50.0, 60.0, 70.0, 80.0, 100.0, 120.0, 150.0, 200.0\}$ GeV for ≥ 1 -jet events (green squares), i.e. the bins used in ref. [19]; and the nominal bin definitions shown in Fig. 5.14 (black circles).

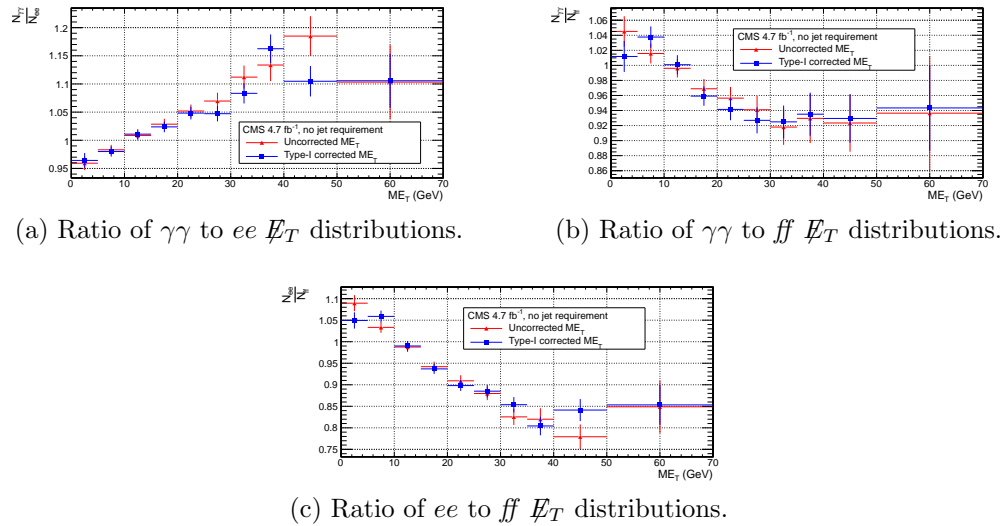


Figure 5.22: Agreement between $\gamma\gamma$, ee , and ff samples for uncorrected (red triangles) and corrected (blue squares) \not{E}_T .

difference in the agreement of the background predictions and the search sample in a control region at low \not{E}_T , as shown in Figure 5.22. Since the control samples are derived from the same data as the search sample, any biases in the \not{E}_T reconstruction due to jet energy scale are present equally in both samples.

Tables 5.4 and 5.5 list all the errors on the ee and ff QCD background predictions, respectively, for the \not{E}_T bins used in the search. Table 5.6 lists the errors on the electroweak background prediction. Finally, Table 5.7 shows the errors on the total QCD + electroweak background prediction, broken down by origin (statistical or systematic) and QCD background estimation sample (ee or ff). In the final result, only the ff QCD estimate is used.

5.4 Results

Figure 5.23(5.24) shows the \not{E}_T distribution of the inclusive(≥ 1 -jet) $\gamma\gamma$ search sample along with the predicted \not{E}_T distributions of the QCD and electroweak backgrounds. The observed number of two-photon events, background estimates and their errors,

Table 5.4: Errors on the ee QCD background prediction as a fraction of the ee prediction.

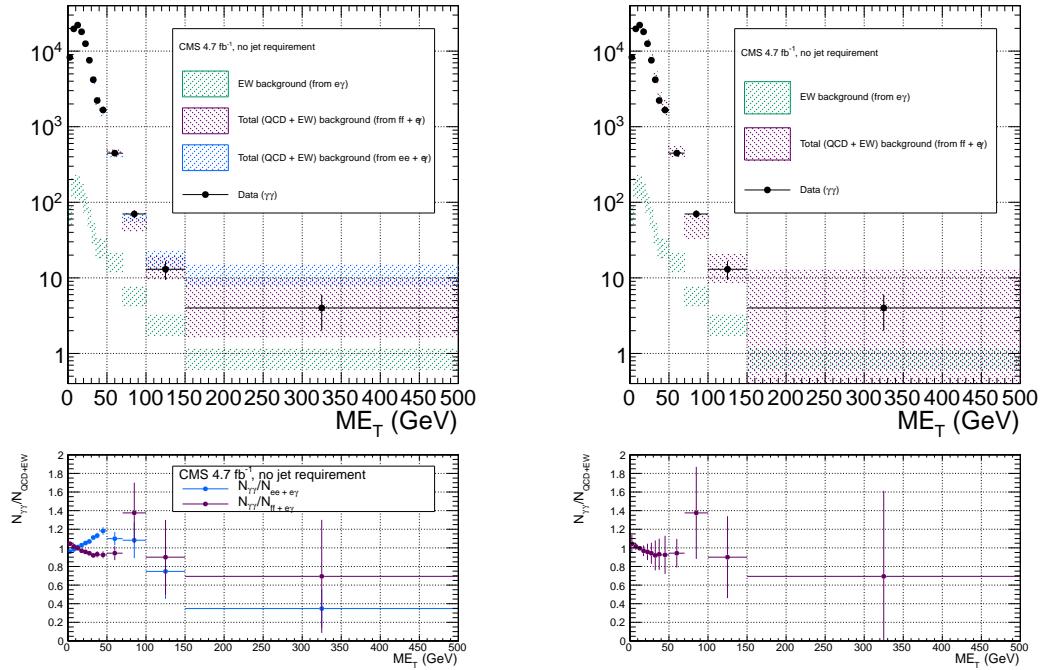
Source of error	Fractional uncertainty (%)				
	[50, 60)	[60, 70)	[70, 80)	[80, 100)	≥ 100
Total	3.9	8.1	16	25	25
Statistics	3.6	7.8	16	24	22
No. events	3.6	7.7	15	24	20
In norm. region	0.43	0.44	0.46	0.55	0.51
In this E_T bin	3.5	7.7	15	24	20
Reweighting	0.73	1.2	3.5	4.3	7.7
In norm. region	0.19	0.19	0.2	0.24	0.23
In this E_T bin	0.71	1.2	3.5	4.3	7.7
Systematics	2.6	4.4	1.2	7.5	14
$f_{e \rightarrow \gamma}$ (in norm. region)	0.0012	0.0012	0.0013	0.0015	0.0014
m_{ee} background shape	1.4	2	0.72	5.5	12
Jet energy scale	2.2	3.9	0.96	5.1	6.9

Table 5.5: Errors on the ff QCD background prediction as a fraction of the ff prediction.

Source of error	Fractional uncertainty (%)				
	[50, 60)	[60, 70)	[70, 80)	[80, 100)	≥ 100
Total	15	25	61	34	64
Statistics	7.2	14	30	33	38
No. events	7.1	14	29	33	36
In norm. region	0.64	0.64	0.64	0.64	0.64
In this E_T bin	7.1	14	29	33	36
Reweighting	0.85	2.7	5.1	6.9	13
In norm. region	0.27	0.27	0.27	0.27	0.27
In this E_T bin	0.81	2.6	5.1	6.9	13
Systematics	13	21	53	6.6	52
ee/ff difference	13	21	53	5.5	52
$f_{e \rightarrow \gamma}$ (in norm. region)	0.0012	0.0012	0.0012	0.0012	0.0012
Jet energy scale	0.099	1.7	1.8	3.5	1.8

Table 5.6: Errors on the $e\gamma$ electroweak background prediction as a fraction of the $e\gamma$ prediction.

Source of error	Fractional uncertainty (%)				
	[50, 60)	[60, 70)	[70, 80)	[80, 100)	≥ 100
Total	29	29	30	30	30
Statistics	3.6	5.2	6.7	7.2	6.5
Systematics ($f_{e \rightarrow \gamma}$)	29	29	29	29	29



(a) $ee + e\gamma$ and $ff + e\gamma$. The widths of the bands correspond to the errors given in Table 5.7, excluding the error associated with the difference between the ee and ff QCD estimates for the $ff + e\gamma$ E_T distribution.

(b) $ff + e\gamma$. The widths of the bands correspond to the errors given in Table 5.7, including the error associated with the difference between the ee and ff QCD estimates.

Figure 5.23: E_T distribution of the $\gamma\gamma$ search sample (black circles) along with the predicted E_T distributions of the QCD and electroweak backgrounds (blue band for ee QCD prediction + electroweak prediction, purple band for ff QCD prediction + electroweak prediction). The electroweak background prediction is shown in green. The bottom plots show the ratio of the $\gamma\gamma E_T$ distribution to the $ee + e\gamma$ background distribution (blue) and $ff + e\gamma$ background distribution (purple).

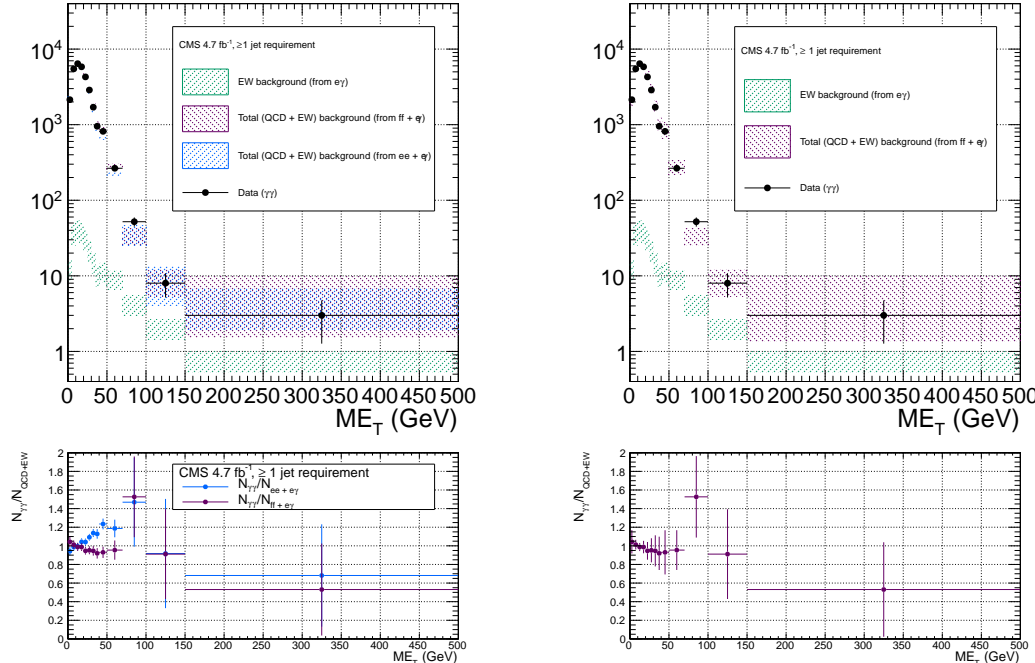
and expected number of inclusive(≥ 1 -jet) two-photon events from two representative GGM SUSY models are listed in Table 5.8(5.9). (Details of the SUSY MC production are given in Chapter 6 and App. A.) No deviation from the Standard Model prediction is observed in the $\gamma\gamma$ search sample.

Table 5.7: Errors on the total QCD + electroweak background prediction as a fraction of the total prediction.

Source of error	Fractional uncertainty (%)				
	[50, 60)	[60, 70)	[70, 80)	[80, 100)	≥ 100
Total ($ee + e\gamma$)	3.9	7.8	15	22	22
Statistics	3.4	7.3	14	21	18
QCD	3.4	7.3	14	21	18
Electroweak	0.13	0.3	0.53	0.79	0.76
Systematics	2.7	4.5	2.6	7.4	13
QCD	2.5	4.1	1.1	6.7	12
Electroweak	1	1.7	2.3	3.2	3.4
Total ($ff + e\gamma$)	14	24	54	30	54
Statistics	6.9	13	26	29	30
QCD	6.9	13	26	29	30
Electroweak	0.11	0.24	0.79	0.83	1.1
Systematics	12	20	47	6.7	43
QCD	12	20	47	5.8	43
Electroweak	0.9	1.3	3.4	3.4	4.8

Table 5.8: Observed numbers of two-photon events, background estimates and their errors, and expected numbers of two-photon events from two representative GGM SUSY models (details of MC simulation given in Chapter 6 and App. A) for the E_T bins used in the search. Errors on the background estimates are detailed in Tables 5.4, 5.5, 5.6, and 5.7. Errors on the expected numbers of GGM events are purely statistical.

Source	No. events				
	[50, 60)	[60, 70)	[70, 80)	[80, 100)	≥ 100
Observation ($\gamma\gamma$)	354	93	37	33	17
Predicted background ($ff + e\gamma$)	361 ± 51.5	113 ± 27.1	26.9 ± 14.5	23.9 ± 7.23	20.2 ± 10.9
$m_{\tilde{q}} = 720$ GeV $M_3 = 720$ GeV $M_1 = 375$ GeV	13.3 ± 2.13	17.7 ± 2.46	15.3 ± 2.33	42.9 ± 3.82	966 ± 18.3
$m_{\tilde{q}} = 1440$ GeV $M_3 = 1440$ GeV $M_1 = 375$ GeV	0.008 ± 0.003	0.009 ± 0.003	0.012 ± 0.003	0.030 ± 0.005	1.92 ± 0.04



(a) $ee + e\gamma$ and $ff + e\gamma$. The widths of the bands correspond to the errors given in Table 5.7, excluding the error associated with the difference between the ee and ff QCD estimates for the $ff + e\gamma$ E_T distribution.

(b) $ff + e\gamma$. The widths of the bands correspond to the errors given in Table 5.7, including the error associated with the difference between the ee and ff QCD estimates.

Figure 5.24: E_T distribution of the $\gamma\gamma + \geq 1$ jet search sample (black circles) along with the predicted E_T distributions of the QCD and electroweak backgrounds (blue band for ee QCD prediction + electroweak prediction, purple band for ff QCD prediction + electroweak prediction). The electroweak background prediction is shown in green. The bottom plots show the ratio of the $\gamma\gamma E_T$ distribution to the $ee + e\gamma$ background distribution (blue) and $ff + e\gamma$ background distribution (purple).

Table 5.9: Observed numbers of two-photon + ≥ 1 -jet events, background estimates and their errors, and expected numbers of two-photon + ≥ 1 -jet events from two representative GGM SUSY models (details of MC simulation given in Chapter 6 and App. A) for the \cancel{E}_T bins used in the search. Errors on the background estimates are detailed in Tables 5.4, 5.5, 5.6, and 5.7. Errors on the expected numbers of GGM events are purely statistical.

Source	No. events				
	[50, 60)	[60, 70)	[70, 80)	[80, 100)	≥ 100
Observation ($\gamma\gamma + \geq 1$ jet)	202	63	27	25	11
Predicted background ($ff + e\gamma$)	200 ± 35.4	77.7 ± 28.1	19.4 ± 8.55	14.7 ± 7.04	14.4 ± 5.59
$m_{\tilde{q}} = 720$ GeV $M_3 = 720$ GeV $M_1 = 375$ GeV	13.3 ± 2.13	17.7 ± 2.46	15.3 ± 2.33	42.9 ± 3.82	965 ± 18.3
$m_{\tilde{q}} = 1440$ GeV $M_3 = 1440$ GeV $M_1 = 375$ GeV	0.008 ± 0.003	0.009 ± 0.003	0.012 ± 0.003	0.031 ± 0.004	1.92 ± 0.04

₁₇₇₉ **Chapter 6**

₁₇₈₀ **Interpretation of Results in Terms**
₁₇₈₁ **of GMSB Models**

₁₇₈₂ As shown in Figs. 5.23 and 5.24 and Tables 5.8 and 5.9, no excess of events above
₁₇₈₃ the Standard Model expectation is found in either the ≥ 0 - or ≥ 1 -jet analyses for the
₁₇₈₄ GMSB-sensitive region $\cancel{E}_T \geq 50$ GeV. Therefore, upper limits on the production cross
₁₇₈₅ sections of various GMSB models are calculated and then translated into statements of
₁₇₈₆ exclusion. Section 6.1 describes the GMSB models that were generated with MC and
₁₇₈₇ tested for exclusion. The upper limit calculation and translation to model exclusions
₁₇₈₈ is laid out in Section 6.2. The upper limits themselves are presented in Section 6.3,
₁₇₈₉ and, finally, the exclusions are presented in Section 6.4.

₁₇₉₀ **6.1 Simplified Models**

₁₇₉₁ The exclusion reach of the two-photon search is presented for three different two-
₁₇₉₂ dimensional scans in GMSB parameter space. The first scan covers the bino NLSP
₁₇₉₃ scenario of Sec. 1.5. In this scan, M_2 , which controls the amount of wino mixing, is
₁₇₉₄ set to 3.5 TeV. M_1 , which controls the amount of bino mixing, is set to 375 GeV.
₁₇₉₅ This insures that all gauginos except the lightest neutralino are too heavy to be

1796 produced in significant numbers at the LHC. All other mass parameters except for
 1797 M_3 (\sim gluino mass) and $m_{\tilde{q}}$ (\sim first- and second-generation squark mass) are set to
 1798 3.5 TeV, which insures that squark/gluino decay to intermediate states such as third-
 1799 generation squarks or any flavor of lepton is strongly suppressed. M_3 and $m_{\tilde{q}}$ are
 1800 scanned over from $M_3 = m_{\tilde{q}} = 400$ GeV to $M_3 = m_{\tilde{q}} = 2$ TeV in 80-GeV steps.
 1801 The resulting simplified model consists only of a gluino, first- and second-generation
 1802 squarks, and the lightest neutralino and its decay products (the gravitino is forced to
 1803 be the LSP). The scan in M_3 - $m_{\tilde{q}}$ space illuminates the sensitivity of the two-photon
 1804 search to different levels of signal hadronic activity.

1805 The second scan is identical to the first except that the values of M_1 and M_2
 1806 are inverted ($M_1 = 3.5$ TeV and $M_2 = 375$ GeV). This corresponds to the wino
 1807 NLSP scenario of Sec. 1.5. Now, both the lightest neutralino and the lightest chargino
 1808 have masses of order 375 GeV, and are therefore produced with approximately equal
 1809 frequency in the gluino and squark decays. The chargino decays to $W + \tilde{G}$, so final
 1810 states in this scan often include leptons or large jet multiplicity. Since there is no
 1811 guarantee that two neutralinos will be produced and will decay to two photons, this
 1812 search is not well optimized for the wino NLSP scenario. However, a related CMS
 1813 search with one photon and ≥ 3 jets has an exclusion reach of ~ 1 TeV in M_3 and
 1814 $m_{\tilde{q}}$ for this scenario [19].

1815 The third scan is M_3 vs. M_1 for $m_{\tilde{q}}$, M_2 , and all other mass parameters equal to
 1816 2.5 TeV. M_3 is scanned from 160 GeV to 2 TeV in 80-GeV steps, while M_1 is scanned
 1817 from 150 GeV to 1050 GeV in 100-GeV steps. $M_3 < M_1$ is not allowed, as this would
 1818 imply that the gluino, not the lightest neutralino, is the NLSP. This scan highlights
 1819 the performance of the two-photon search as a function of M_1 (i.e. as a function of
 1820 decays open to the neutralino), whereas the previous two scans keep M_1 fixed.

1821 For each scan, the sparticle mass spectrum is generated with SuSpect 2.41 [111]
 1822 and the decay widths with SDECAY 1.3 [112]. The event data (including produc-

tion, unstable particle decay, parton showering, and hadronization) is generated with
 Pythia 6.422 [116], using the sparticle mass spectra and decay widths as inputs. The
 gravitino is always forced to be the LSP. The simulated data are reconstructed with
 CMSSWv4.2.2, which uses a detector simulation based on GEANT 4 [113]. Next to
 leading order cross sections are calculated with PROSPINO 2.1 [114], and shown in
 Figure 6.1 for the three signal MC scenarios.

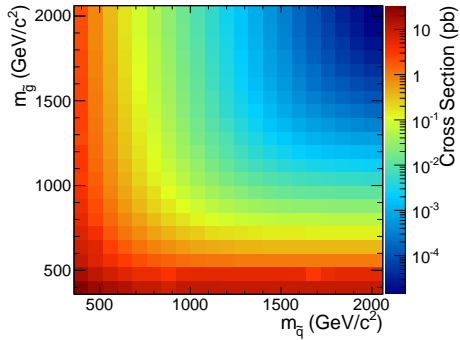
6.2 Upper Limit Calculation and Model Exclusion

The upper limits are calculated according to the prescription followed for the 2011
 ATLAS + CMS Higgs limit combination [101]. This prescription utilizes the frequen-
 tist CL_s method [102] with profile likelihood test statistic [103]. The CL_s method and
 the profile likelihood are explained in Section 6.2.2, using specific signal MC points to
 illustrate the procedure. First, however, the signal MC acceptance \times efficiency, which
 is an input to the limit setting procedure, is presented in Section 6.2.1.

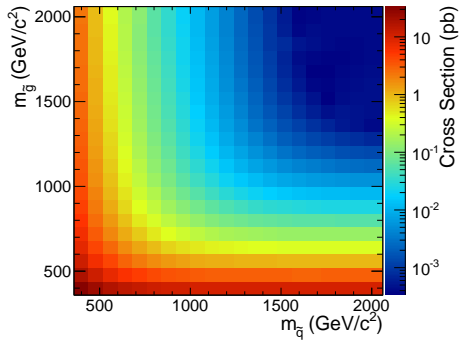
6.2.1 Signal Acceptance \times Efficiency

The signal acceptance \times efficiency (denoted $\mathcal{A} \times \epsilon$), defined for each signal point as
 the number of $\gamma\gamma$ events selected with $\cancel{E}_T \geq 50$ GeV divided by the total number of
 events generated, is shown in Figure 6.2 for the three different scenarios described in
 Sec. 6.1.

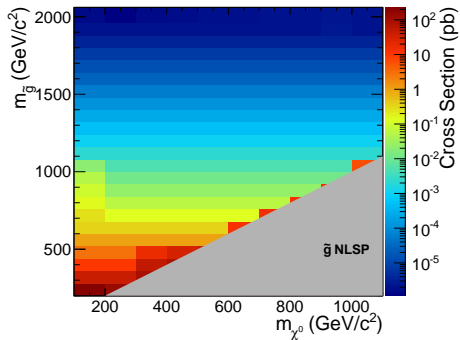
In Figs. 6.2a and 6.2b, the large drop in $\mathcal{A} \times \epsilon$ for $m_{\tilde{q}} > M_3$ is due to an increase
 in the number of jets produced per event and a consequent reduction in the number
 of photons that pass the $I_{\text{comb}} < 6$ GeV cut. For $m_{\tilde{q}} > M_3$, there is more phase space
 available to produce gluinos in the hard scatter than squarks. However, since gluinos
 must decay via squarks, and in these models all squarks are heavier than the gluino,
 only the two-jet decay $\tilde{g} \rightarrow qq\tilde{\chi}^0$ is available. Conversely, when $m_{\tilde{q}} < M_3$, there is



(a) M_2 decoupled ($M_2 = 3.5$ TeV), $M_1 = 375$ GeV, M_3 vs. $m_{\tilde{q}}$.



(b) M_1 decoupled ($M_1 = 3.5$ TeV), $M_2 = 375$ GeV, M_3 vs. $m_{\tilde{q}}$.



(c) $m_{\tilde{q}}$ decoupled ($m_{\tilde{q}} = 2.5$ TeV), M_3 vs. M_1 .

Figure 6.1: Next to leading order cross sections for the three different MC scenarios described in the text.

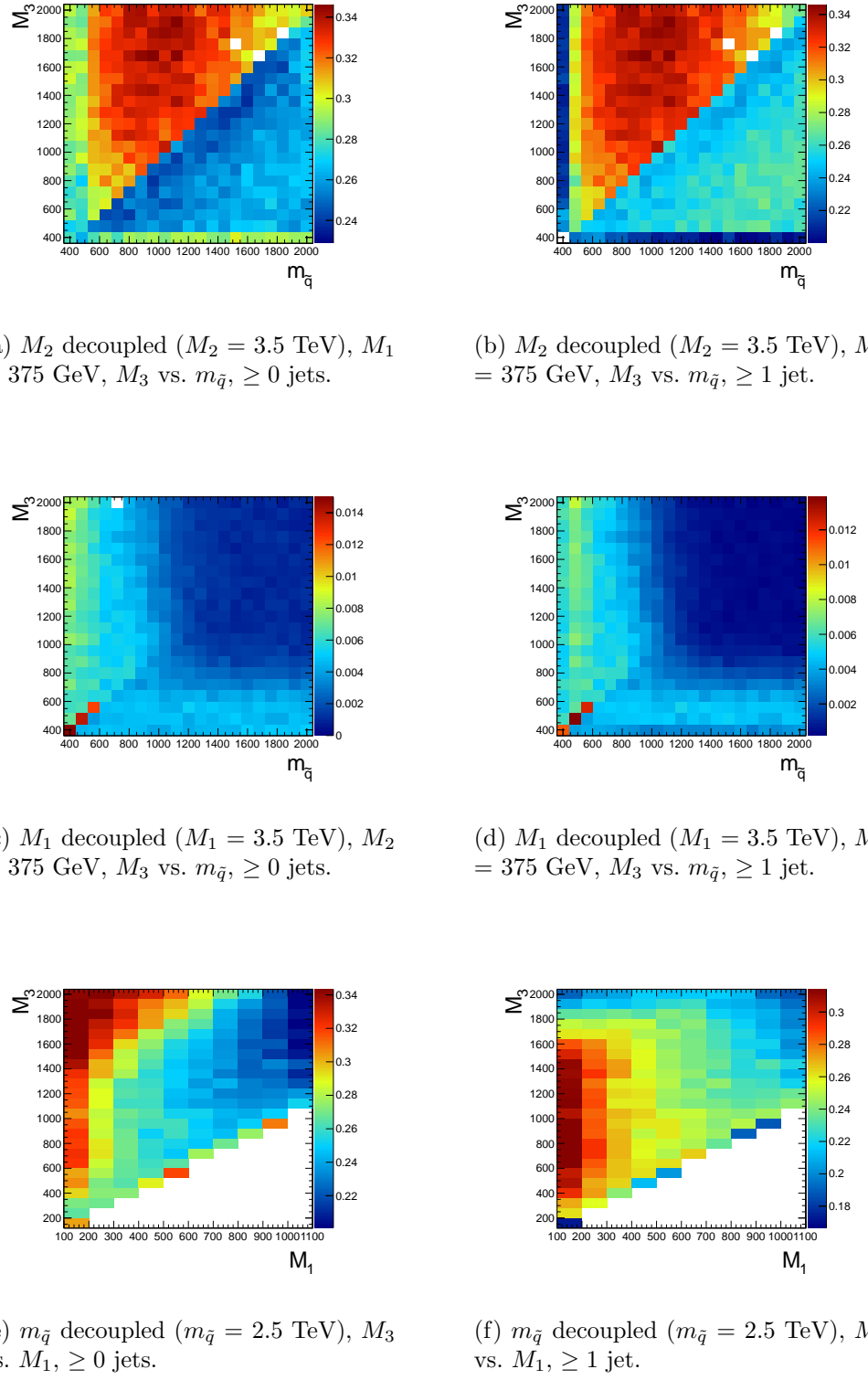


Figure 6.2: Signal acceptance \times efficiency (defined in the text) for the three different scenarios described in Sec. 6.1.

1847 more phase space available to produce squarks, which may then decay via one jet as
 1848 $\tilde{q} \rightarrow q\tilde{\chi}^0$. Jets in SUSY events may be very close to the neutralino decay photons,
 1849 and as a result the photons may fail the strict isolation requirements, leading to lower
 1850 $\mathcal{A} \times \epsilon$ for jet-rich events. The worsened acceptance along $M_3 = 400$ GeV and $m_{\tilde{q}} = 400$
 1851 GeV in Fig. 6.2b is due to efficiency of the jet cut, which decreases drastically as M_3
 1852 and $m_{\tilde{q}}$ approach M_1 because of shrinking phase space to produce hard jets in the
 1853 squark and gluino decays to neutralinos.

1854 The broad peak in $\mathcal{A} \times \epsilon$ shown in Fig. 6.2a for $m_{\tilde{q}} < M_3$ and ~ 600 GeV $< m_{\tilde{q}} <$
 1855 ~ 1600 GeV is due to the $\cancel{E}_T > 50$ GeV cut. The efficiency of the cut decreases
 1856 as $m_{\tilde{q}}$ decreases because of the fixed M_1 of 375 GeV. If the squark-neutralino mass
 1857 splitting gets too small, the likelihood of producing an energetic enough gravitino to
 1858 pass the \cancel{E}_T cut decreases.

1859 $\mathcal{A} \times \epsilon$ is generally much lower for the $M_2 = 375$ GeV grid (Figs. 6.2c and 6.2d)
 1860 due to the larger contribution from chargino decays to $W + \tilde{G}$, which do not give rise
 1861 to photons in the final state. The increased acceptance for $M_3 > m_{\tilde{q}}$ is due to the
 1862 same jet multiplicity issue affecting the $M_1 = 375$ GeV grid. As M_3 and $m_{\tilde{q}}$ increase
 1863 relative to the fixed M_2 , the jets from squark and gluino decay get more energetic,
 1864 increasing the chance that they will overlap with the neutralino decay photon and
 1865 cause it to fail the isolation cut. For $m_{\tilde{q}} \gtrsim 1$ TeV and $M_3 \gtrsim 800$ GeV, the acceptance
 1866 is so low that not enough events were simulated to see the acceptance decrease over
 1867 the statistical error.

1868 In Fig. 6.2e, the neutralino is always heavy enough to guarantee decay to a photon
 1869 that can pass the 40 GeV p_T cut. $\mathcal{A} \times \epsilon$ increases as M_3 increases because the larger
 1870 gluino-neutralino mass splitting gives the neutralino a larger kinetic energy, increasing
 1871 the chance that it will decay to a photon with 40 GeV p_T or higher. After the bino mass
 1872 increases beyond the threshold needed to produce high p_T photons, $\mathcal{A} \times \epsilon$ decreases
 1873 with increasing M_1 , independent of gluino mass, because higher M_1 means more phase

1874 space is open to decays of the form $\tilde{\chi}_1^0 \rightarrow Z\tilde{G}$ and $\tilde{\chi}_1^0 \rightarrow H\tilde{G}$. The two-photon search
 1875 is naturally not as efficient for these decays.

Added

1876 There is a small chance that some real GMSB signal events could be reconstructed signal
 1877 as ff events in the data. To correct the signal acceptance for this effect, the number contamination
 1878 of signal events reconstructed as ff events is subtracted from the number of signal $\gamma\gamma$ ination
 1879 events, effectively reducing the signal acceptance. This is generally a small correction par.
 1880 ($\sim 5\%$).

1881 **6.2.2 CL_s and the Profile Likelihood Test Statistic**

1882 The process of setting a cross section upper limit entails (1) defining a test statistic,
 1883 (2) generating a distribution for that test statistic under the signal + background
 1884 and background-only hypotheses, and (3) deciding whether or not the observed value
 1885 of the test statistic is more compatible with the signal + background (i.e. weaker
 1886 upper limit) or background-only (i.e. stronger upper limit) hypotheses by considering
 1887 where it falls within the test statistic distributions. An important requirement on the
 1888 choice of test statistic is that it be able to effectively discriminate between the signal
 1889 + background and background-only hypotheses, i.e. the shape of its distribution for
 1890 these two hypotheses should be different. The procedure for determining the exclud-
 1891 ability of a particular model given the value of the test statistic observed should not
 1892 give rise to pathological behavior in the presence of small signals, low statistics, or
 1893 weak sensitivity to models, as is commonly the case in high energy physics. These
 1894 demands on the test statistic and the limit setting procedure itself dictate the choice
 1895 of the profile likelihood test statistic and CL_s procedure.

1896 In the remainder of this section, the notation is taken from ref. [101].

1897 **Profile Likelihood**

1898 For a specific model of GMSB, the limit setting procedure concerns the question of
 1899 whether to reject the signal + background hypothesis $\mu s + b$ in favor of the background-
 1900 only (Standard Model) hypothesis of b ($\mu = 0$). μ is a dimensionless signal strength
 1901 parameter. s is the expected number of signal events, calculated from MC simulated
 1902 signal events as in Secs. 6.1 and 6.2.1. b is the expected number of background events,
 1903 estimated in Chap. 5. By the Neyman-Pearson lemma [104], the ratio of the likelihood
 1904 of $\mu s + b$ to the likelihood of b is the test statistic with the highest power to reject $\mu s + b$
 1905 at whatever confidence level is desired. In practice, this means that the likelihood ratio
 1906 is the best discriminator between the GMSB and Standard Model hypotheses.

1907 The likelihood of the signal + background hypothesis as a function of the data
 1908 (either real or generated) is defined as

$$\mathcal{L}(\text{data}|\mu, \theta) = \prod_{i=1}^N \frac{(\mu s_i(\theta) + b_i(\theta))^{n_i}}{n_i!} e^{-\mu s_i(\theta) - b_i(\theta)} p(\tilde{\theta}|\theta) \quad (6.1)$$

1909 where $N = 5$ is the number of E_T bins used in the analysis ([50, 60) GeV, [60,
 1910 70) GeV, [70, 80) GeV, [80, 100) GeV, and [100, ∞) GeV); $s_i(\theta)$ and $b_i(\theta)$ are the
 1911 expected number of signal and background events in E_T bin i , respectively; n_i is the
 1912 number of events observed in E_T bin i ; and θ represents all the nuisance parameters
 1913 (uncertainties). $p(\tilde{\theta}|\theta)$ represents the product of probability distribution functions
 1914 (PDFs) for the nuisance parameters, where $\tilde{\theta}$ is the default value of the nuisance
 1915 parameter. In this analysis, there are eight experimental nuisance parameters per E_T
 1916 bin, given here as relative errors on the expected number of signal events:

- 1917 • Uncertainty on the measured integrated luminosity (4.5% in all bins) [105]
- 1918 • Uncertainty on the signal acceptance due to $\epsilon_e^{\text{data}}/\epsilon_e^{\text{MC}}$ and the pixel veto effi-
 1919 ciency error (cf. Sec. 4.4.2) (8% in all bins)

- 1920 ● Uncertainty on the signal acceptance due to imperfect pileup simulation (2.6%
1921 in all bins)
 - 1922 ● Systematic uncertainty on QCD background prediction due to difference be-
1923 tween ff and ee estimates (5.5%-53% of the QCD background depending on
1924 bin)
 - 1925 ● Systematic uncertainty on electroweak background prediction due to p_T depen-
1926 dence of $f_{e \rightarrow \gamma}$ (29%-30% of the electroweak background depending on bin)
 - 1927 ● Statistical uncertainty on the signal acceptance (1.8%-100% depending on model
1928 and bin)
 - 1929 ● Statistical uncertainty on the QCD background prediction (7.2%-38% of the
1930 QCD background depending on bin)
 - 1931 ● Statistical uncertainty on the electroweak background prediction (3.6%-7.2% of
1932 the electroweak background depending on bin)
- 1933 and one very small theoretical nuisance parameter: the uncertainty on the signal
1934 acceptance due to underlying parton distribution function (PDF) uncertainties. In
1935 the limit-setting code, the uncertainties on signal acceptance due to photon efficiency
1936 and PDF errors are added in quadrature and treated as one. The uncertainty on the
1937 signal acceptance due to jet energy correction uncertainties is negligible, due to the
1938 presence of many hard jets in GMSB signal events. The uncertainties on integrated
1939 luminosity and pileup are 100% correlated between \cancel{E}_T bins, and the uncertainty on
1940 signal acceptance can usually be treated similarly because the error on $\epsilon_e^{\text{data}}/\epsilon_e^{\text{MC}}$ often
1941 dominates the PDF error on acceptance (although these three uncertainties are 0%
1942 correlated with each other).

1943 To estimate the uncertainty due to imperfect simulation of LHC pileup, the square
1944 of the average data efficiency for photons over the range 1-15 reconstructed primary

1945 vertices (see Fig. 4.17a), weighted by the number of $\gamma\gamma$ events per primary vertex bin,
 1946 is calculated. The efficiency per primary vertex bin is estimated from a linear fit to
 1947 Fig. 4.17a. The process is repeated for MC using the entire range of primary vertices
 1948 in Fig. 4.17a (all MC signal points have the same pileup simulation). The error is
 1949 taken as $2 \times |\text{avg. data efficiency squared} - \text{avg. MC efficiency squared}| / (\text{avg. data}$
 1950 efficiency squared + avg. MC efficiency squared).

1951 Each nuisance parameter PDF is modeled by a log-normal distribution:

$$p(\tilde{\theta}|\theta) = \frac{1}{\sqrt{2\pi} \ln \kappa} \exp\left(-\frac{(\ln \tilde{\theta}/\theta)^2}{2(\ln \kappa)^2}\right) \frac{1}{\tilde{\theta}} \quad (6.2)$$

1952 where $\tilde{\theta} = 1$ and $\kappa = 1 +$ the one-standard-deviation relative error on the nuisance
 1953 parameter (e.g. for the 4.5% error due to integrated luminosity, $\kappa = 1.045$).

1954 Similarly, the likelihood of the background-only hypothesis as a function of the
 1955 data (either real or generated) is defined as

$$\mathcal{L}(\text{data}|\mu, \theta) = \prod_{i=1}^N \frac{b_i(\theta)^{n_i}}{n_i!} e^{-b_i(\theta)} p(\tilde{\theta}|\theta) \quad (6.3)$$

1956 The profile likelihood test statistic is defined as

$$\tilde{q}_\mu = -2 \ln \frac{\mathcal{L}(\text{data}|\mu, \hat{\theta}_\mu)}{\mathcal{L}(\text{data}|\hat{\mu}, \hat{\theta})}, 0 \leq \hat{\mu} \leq \mu \quad (6.4)$$

1957 where the $\hat{\theta}_\mu$ maximize $\mathcal{L}(\text{data}|\mu, \hat{\theta}_\mu)$ when it is evaluated at a particular μ , and
 1958 $\hat{\mu}$ and $\hat{\theta}$ are the global maximum likelihood estimators of μ and θ . The condition
 1959 $\hat{\mu} \leq \mu$ insures that the obtained cross section upper limit is one-sided, i.e. there is
 1960 no possibility to find a lower limit on the cross section. The profile likelihood test

1961 statistic has the nice property that in the asymptotic (large statistics) limit its PDF
 1962 can be approximated by analytic formulae, eliminating the need to generate multiple
 1963 toy experiments to get the PDF. However, the approximation breaks down for small
 1964 numbers of observed events, so in practice the asymptotic limit is only used as a first
 1965 guess at the location of the true limit.

1966 The PDFs $f(\tilde{q}_\mu | \mu, \hat{\theta}_\mu^{\text{obs}})$ and $f(\tilde{q}_\mu | 0, \hat{\theta}_0^{\text{obs}})$ for the profile likelihood test statistic
 1967 under the signal + background and background-only hypotheses, respectively, are
 1968 obtained by generating toy MC pseudo-experiments. $\hat{\theta}_\mu^{\text{obs}}$ and $\hat{\theta}_0^{\text{obs}}$ maximize Eqs. 6.1
 1969 and 6.3, respectively, when they are evaluated for the observed data. For each μ (and
 1970 the background-only hypothesis $\mu = 0$), the pseudo-experiments are generated by
 1971 picking random values of s and b from a Poisson distribution with the θ fixed as just
 1972 described.

1973 **CL_s**

1974 In the classical frequentist approach, a signal model may be excluded at the 95%
 1975 confidence level (CL) if the probability of any measurement of the test statistic to be
 1976 greater than or equal to the observed value given the signal + background hypothesis
 1977 is 5%. This means that the observed value of the test statistic is so incompatible
 1978 with what one would expect to observe if the signal model were true that, under the
 1979 assumption that the signal model *is* true, the chance of observing a test statistic even
 1980 further afield from the signal expectation is only 5%. Mathematically,

$$\begin{aligned} p_\mu &\equiv P(\tilde{q}_\mu \geq \tilde{q}_\mu^{\text{obs}} | \mu s + b) = \int_{\tilde{q}_\mu^{\text{obs}}}^{\infty} f(\tilde{q}_\mu | \mu, \hat{\theta}_\mu^{\text{obs}}) d\tilde{q}_\mu \\ p_\mu &\leq 0.05 \Rightarrow \text{exclude } \mu \end{aligned} \quad (6.5)$$

1981 where $\tilde{q}_\mu^{\text{obs}}$ is the observed value of the test statistic and p_μ is the p-value. As indicated
 1982 in Eq. 6.5, the p-value is simply the integral of the PDF of \tilde{q}_μ from $\tilde{q}_\mu^{\text{obs}}$ to infinity.

1983 By construction, the classical 95% CL frequentist approach described above will
 1984 reject a true signal + background hypothesis 5% of the time. This can happen if the
 1985 experiment gets “unlucky” and the observation fluctuates low, causing $\tilde{q}_\mu^{\text{obs}}$ to fall in
 1986 the tail of the \tilde{q}_μ distribution. This poses a problem for the case of very weak signals
 1987 ($\mu \sim 0$), because it will lead to spurious exclusions of models to which the experiment
 1988 has little sensitivity. To avoid this pitfall, the CL_s limit setting method is used.

1989 In the CL_s method, the classical frequentist p-value of Eq. 6.5 is simply divided by
 1990 one minus the p-value of the background-only hypothesis, and it is this ratio, rather
 1991 than the p-value of the signal + background hypothesis alone, that is required to be
 1992 ≤ 0.05 . Mathematically,

$$1 - p_0 \equiv P(\tilde{q}_\mu \geq \tilde{q}_\mu^{\text{obs}} | b) = \int_{\tilde{q}_\mu^{\text{obs}}}^{\infty} f(\tilde{q}_\mu | 0, \hat{\theta}_0^{\text{obs}}) d\tilde{q}_\mu \quad (6.6)$$

$$\text{CL}_s(\mu) \equiv \frac{p_\mu}{1 - p_0} \quad (6.7)$$

$$\text{CL}_s(\mu) \leq 0.05 \Rightarrow \text{exclude } \mu$$

1993 where p_0 is the p-value for the background-only hypothesis ($\mu = 0$). In the case of
 1994 low sensitivity to μ , $p_\mu \lesssim 1 - p_0$, so $\text{CL}_s(\mu) \lesssim 1$ and μ will not be excluded. On the
 1995 contrary, for high sensitivity to μ ($\mu s \gg \sigma_b$), $p_\mu \ll 1 - p_0$, so models that can be
 1996 excluded by the criterion $p_\mu \leq 0.05$ will also be excluded by the criterion $\text{CL}_s \leq 0.05$.
 1997 Compared to the classical frequentist method, CL_s limits can be a little stronger in
 1998 the case of low signal sensitivity [101].

1999 To determine the upper limit on the cross section of a particular model, the lowest
 2000 value of μ for which $\text{CL}_s(\mu) \leq 0.05$, denoted $\mu^{95\% \text{CL}}$, is found. The cross section upper
 2001 limit of that model is then simply $\mu^{95\% \text{CL}}$ multiplied by the expected cross section of

2002 the model (cf. Fig. 6.1).

2003 In contrast to the observed upper limit, the expected upper limit is calculated from
 2004 an ensemble of background-only MC pseudo-experiments. The distribution $f(\mu_{\text{pseudo}}^{\text{95%CL}})$
 2005 is plotted (one entry per pseudo-experiment). The median expected upper limits and
 2006 $\pm 1\sigma$ and $\pm 2\sigma$ bands are defined as

$$0.5 = \int_0^{\mu_{\text{exp}}^{\text{95%CL}}} f(\mu_{\text{pseudo}}^{\text{95%CL}}) d\mu_{\text{pseudo}}^{\text{95%CL}} \quad (6.8)$$

$$0.16 = \int_0^{\mu_{-1\sigma,\text{exp}}^{\text{95%CL}}} f(\mu_{\text{pseudo}}^{\text{95%CL}}) d\mu_{\text{pseudo}}^{\text{95%CL}} \quad (6.9)$$

$$0.84 = \int_0^{\mu_{+1\sigma,\text{exp}}^{\text{95%CL}}} f(\mu_{\text{pseudo}}^{\text{95%CL}}) d\mu_{\text{pseudo}}^{\text{95%CL}} \quad (6.10)$$

$$0.025 = \int_0^{\mu_{-2\sigma,\text{exp}}^{\text{95%CL}}} f(\mu_{\text{pseudo}}^{\text{95%CL}}) d\mu_{\text{pseudo}}^{\text{95%CL}} \quad (6.11)$$

$$0.975 = \int_0^{\mu_{+2\sigma,\text{exp}}^{\text{95%CL}}} f(\mu_{\text{pseudo}}^{\text{95%CL}}) d\mu_{\text{pseudo}}^{\text{95%CL}} \quad (6.12)$$

2007 The technical procedure followed to calculate the 95% CL cross section upper
 2008 limits for each GMSB model tested is given below.

2009 1. Calculate a guess for the median expected limit and $\pm 2\sigma$ error bands ($\mu_{\pm 2\sigma,\text{guess}}^{\text{95%CL}}$)
 2010 using the asymptotic formulae for $f(\tilde{q}_\mu | 0, \hat{\theta}_0^{\text{obs}})$.

2011 2. Calculate observed ($\mu_{\text{obs,asym}}^{\text{95%CL}}$), median expected ($\mu_{\text{exp,asym}}^{\text{95%CL}}$), and $\pm 1\sigma$ ($\mu_{\pm 1\sigma,\text{asym}}^{\text{95%CL}}$)
 2012 and $\pm 2\sigma$ ($\mu_{\pm 2\sigma,\text{asym}}^{\text{95%CL}}$) expected CL_s limits using the asymptotic formulae for
 2013 $f(\tilde{q}_\mu | \mu, \hat{\theta}_\mu^{\text{obs}})$ and $f(\tilde{q}_\mu | 0, \hat{\theta}_0^{\text{obs}})$. Restrict the range of $\mu_{\text{obs,asym}}^{\text{95%CL}}$ and $\mu_{\text{exp,asym}}^{\text{95%CL}}$ to
 2014 $[0, 5 \times \mu_{\pm 2\sigma,\text{guess}}^{\text{95%CL}}]$ (this avoids pathological behavior of the limit-setting code
 2015 when the expected number of signal events is much greater than the observed
 2016 number of events and only introduces a $\sim 5\%$ upward bias in the observed limit,
 2017 well within the $\pm 1\sigma$ error bands).

2018 3. Calculate median expected ($\mu_{\text{exp}}^{\text{95%CL}}$) and $\pm 1\sigma$ ($\mu_{\pm 1\sigma}^{\text{95%CL}}$) and $\pm 2\sigma$ ($\mu_{\pm 2\sigma}^{\text{95%CL}}$) ex-

2019 pected CL_s limits using 100 toy MC pseudo-experiments to generate $f(\tilde{q}_\mu|\mu, \hat{\theta}_\mu^{\text{obs}})$
 2020 and $f(\tilde{q}_\mu|0, \hat{\theta}_0^{\text{obs}})$. Restrict the range of $\mu_{\text{exp}}^{95\%CL}$ to $[0, 5 \times \mu_{\pm 2\sigma, \text{guess}}^{95\%CL}]$.

 2021 4. If $\mu_{\pm 2\sigma}^{95\%CL}$ could not be calculated, set $\mu_{\pm 2\sigma}^{95\%CL} = \mu_{\pm 2\sigma, \text{asym}}^{95\%CL}$ instead.

 2022 5. If $\mu_{+2\sigma}^{95\%CL} \neq \mu_{-2\sigma}^{95\%CL}$ and $\mu_{\text{obs}, \text{asym}}^{95\%CL} > 0.0001$:

 2023 • If $\mu_{\text{obs}, \text{asym}}^{95\%CL} > \mu_{+2\sigma}^{95\%CL}$, set $\mu_{+2\sigma}^{95\%CL} = 1.3 \times \mu_{\text{obs}, \text{asym}}^{95\%CL}$.

 2024 • If $\mu_{\text{obs}, \text{asym}}^{95\%CL} < \mu_{-2\sigma}^{95\%CL}$, set $\mu_{-2\sigma}^{95\%CL} = 0.7 \times \mu_{\text{obs}, \text{asym}}^{95\%CL}$.

 2025 6. If $\mu_{+2\sigma}^{95\%CL} = \mu_{-2\sigma}^{95\%CL}$, set $\mu_{\pm 2\sigma}^{95\%CL} = \mu_{\pm 2\sigma, \text{asym}}^{95\%CL}$ instead.

 2026 7. Scan over 100 equally spaced test values of μ between $\mu_{-2\sigma}^{95\%CL}$ and $\mu_{+2\sigma}^{95\%CL}$ and,
 2027 if $\mu > 0.0001$, calculate the CL_s p-value (p_μ) for this test value of μ to 10^{-6}
 2028 precision using a minimum of 500 toy experiments to generate $f(\tilde{q}_\mu|\mu, \hat{\theta}_\mu^{\text{obs}})$ and
 2029 $f(\tilde{q}_\mu|0, \hat{\theta}_0^{\text{obs}})$.

 2030 8. Determine the observed ($\mu_{\text{obs}, \text{scan}}^{95\%CL}$), median expected ($\mu_{\text{exp}, \text{scan}}^{95\%CL}$), and $\pm 1\sigma$ ($\mu_{\pm 1\sigma, \text{scan}}^{95\%CL}$)
 2031 and $\pm 2\sigma$ ($\mu_{\pm 2\sigma, \text{scan}}^{95\%CL}$) expected CL_s limits from the scan p-values for the signal
 2032 + background and background-only pseudo-experiments.

 2033 Finally, a particular GMSB model is excluded if the upper limit on the cross
 2034 section for that model is less than the expected theoretical cross section.

2035 6.3 Cross Section Upper Limits

2036 Figure 6.3 shows the observed upper limits on the cross sections for the models de-
 2037 scribed in Sec. 6.1. In some ($\mathcal{O}(10^{-3})$) cases, the upper limit is zero due to a com-
 2038 putational failure. The upper limit for these points is estimated from the average of the
 2039 upper limits of the four neighboring points, as shown in Figure 6.4. If any of the four
 2040 points is also missing a valid upper limit, it is dropped from the average. The errors

2041 on the individual upper limits used in the estimate are propagated to the error on
 2042 the average.

2043 6.4 Exclusion Contours

2044 Exclusion contours for the GMSB models discussed above are shown in Figure 6.5. The
 2045 contours are derived from plots of predicted cross section minus cross section upper
 2046 limit ($\sigma \times (1 - \mu^{95\%CL})$), where σ is the nominal value of the predicted cross section
 2047 for a given GMSB model) vs. the two model parameters of interest, so the values are
 2048 either negative (not excluded) or positive (excluded). Sometimes, a particular point
 2049 may have a different sign than its four same-sign neighbors (cf. Fig. 6.4) due to a
 2050 fluctuation. In these cases, $\sigma \times (1 - \mu^{95\%CL})$ for the anomalous point is estimated
 2051 as the average $\sigma \times (1 - \mu^{95\%CL})$ of the four neighboring points. The errors on the
 2052 individual values of $\sigma \times (1 - \mu^{95\%CL})$ used in the estimate are propagated to the error
 2053 on the average.

2054 In the plots in Fig. 6.5, the expected limit (i.e. the contour derived from $\sigma \times (1 -$
 2055 $\mu_{\text{exp,scan}}^{95\%CL})$) is drawn in dark orange and the 1σ experimental band around the expected
 2056 limit (i.e. the shaded region between the contours derived from $\sigma \times (1 - \mu_{\pm 1\sigma, \text{scan}}^{95\%CL})$) is
 2057 drawn in light orange. The values of $\mu_{\text{exp,scan}}^{95\%CL}$ and $\mu_{\pm 1\sigma, \text{scan}}^{95\%CL}$ only reflect the experimental
 2058 uncertainties given in Sec. 6.2.2.

2059 The observed limits (derived from $\sigma \times (1 - \mu_{\text{obs,scan}}^{95\%CL})$) and 1σ theoretical error
 2060 bands around the observed limits in Fig. 6.5 are drawn in blue. The contours that
 2061 define this band are derived from $\pm(\sigma_{\pm 1\sigma} - \sigma \mu_{\text{obs,scan}}^{95\%CL})$, where $\sigma_{\pm 1\sigma}$ is the nominal
 2062 value of the predicted cross section \pm the one-standard-deviation theoretical error on
 2063 the predicted cross section. In this way, the experimental and theoretical errors, the
 2064 latter due to imperfect knowledge of the predicted cross section, are shown separately.
 2065 Comparing with Fig. 6.1, one can easily see that the shapes of the exclusion curves

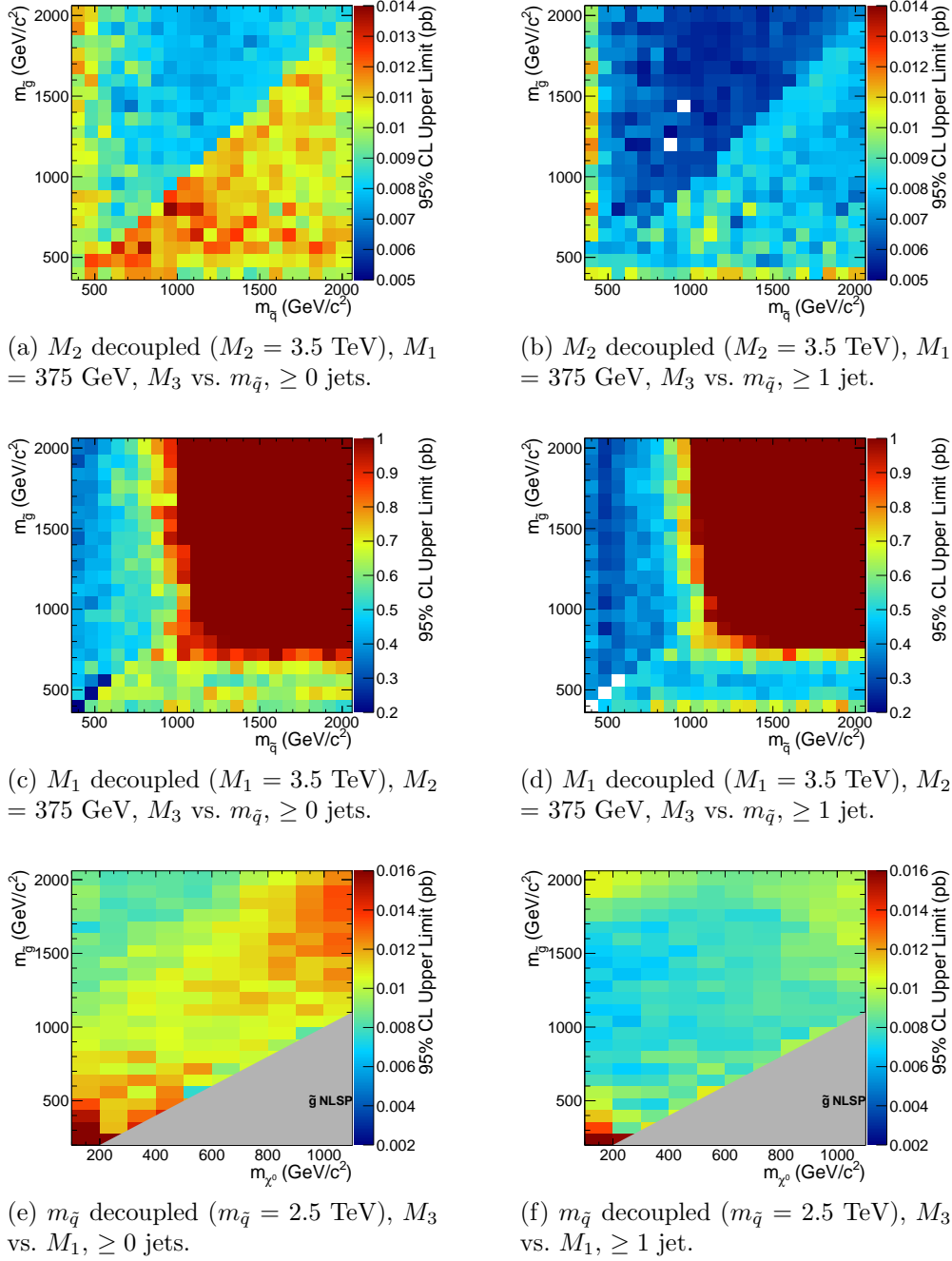


Figure 6.3: Cross section upper limits for the three different scenarios described in Sec. 6.1.

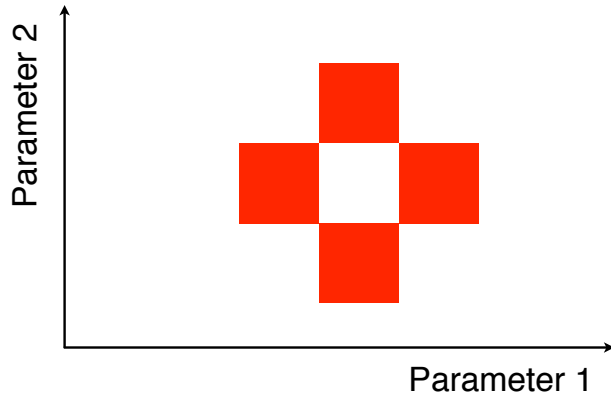


Figure 6.4: Diagram of the points (red squares) used in the estimation of an upper limit when a computational failure occurs (middle white square).

2066 are driven by the contours in the expected cross section plane.

2067 The dominant theoretical uncertainties on the GMSB cross sections are due to:

- 2068 • PDF uncertainty (4%-100% depending on model)
- 2069 • Renormalization scale uncertainty (0.036%-25% depending on model)

2070 The PDF4LHC [106] recommendations are used to calculate the effect of these un-
2071 certainties on the GMSB cross sections. The recommendations state that PDF sets
2072 from MSTW08 [107], CTEQ6.6 [108], and NNPDF2.0 [109] should be considered in
2073 the determination of the PDF uncertainties, because these three PDF sets include
2074 constraints from the Tevatron and from fixed target experiments, as well as from
2075 HERA [?], and are thus the most complete.

2076 Each collaboration's PDF prediction comes from a global fit to experimental data
2077 with a certain number of free parameters. The best fit parameters come from mini-
2078 mizing the χ^2 ; increasing the χ^2 by one from its minimum can be written in terms of
2079 the N -dimensional Hessian error matrix [?] where N is the number of free parameters.

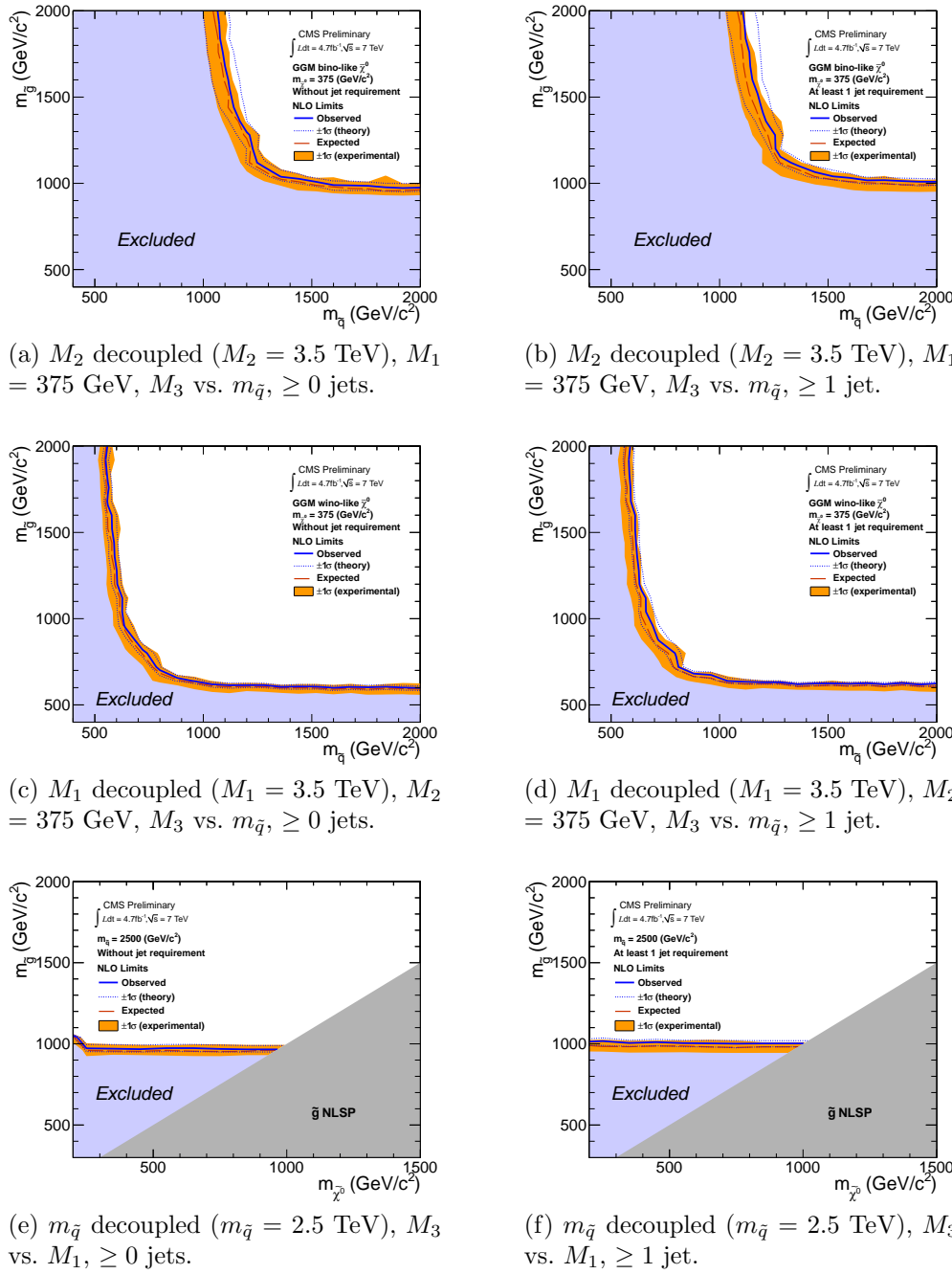


Figure 6.5: Exclusion contours for the three different scenarios described in Sec. 6.1.

2080 To form the i^{th} pair of members of the PDF set, the PDF is evaluated once at the
 2081 parameter values given by the i^{th} eigenvector of the Hessian matrix, and then again
 2082 at the parameter values given by the negative of the i^{th} eigenvector. Each PDF set
 2083 therefore contains $2N$ members, corresponding to the positive and negative values of
 2084 the N eigenvectors [110].

2085 To calculate the PDF uncertainties for a given GMSB model, the leading order
 2086 Pythia cross section is reweighted by a factor of the error PDF divided by the leading
 2087 order PDF with which the model was generated. This is repeated for each error PDF
 2088 in a given PDF set. The $\pm 1\sigma$ deviations are proportional to the maximum difference
 2089 between cross sections obtained this way. The actual equation for the $\pm 1\sigma$ errors is
 2090 Eq. (43) of ref. [110]. In the same way, the $\pm 1\sigma$ errors are calculated for the CTEQ6.6,
 2091 MSTW08, and NNPDF2.0 PDF sets. The total error is given by the half the difference
 2092 between the largest $+1\sigma$ deviation and the smallest -1σ deviation [106].

2093 The uncertainties on the signal cross sections due to the choice of renormaliza-
 2094 tion/factorization scale ($\alpha_S(M_Z)$) are evaluated by calculating the PROSPINO next
 2095 to leading order cross section once with $\alpha_S(M_Z)$ halved, then once with $\alpha_S(M_Z)$ dou-
 2096 bled. The lower error on the cross section is taken as the absolute difference between
 2097 the nominal and halved-scale values of the cross section, while the upper error is taken
 2098 as the absolute difference between the nominal and doubled-scale values. The PDF
 2099 and α_S uncertainties are added in quadrature to give the total PDF uncertainty.

2100 Note that the quoted GMSB cross sections are evaluated at next to leading order
 2101 using PROSPINO, but it is the leading order Pythia cross sections that are reweighted
 2102 to the next to leading order MSTW08, CTEQ6.6, and NNPDF2.0 PDFs to get the
 2103 error bands. In addition, since to a good approximation the GMSB production cross
 2104 sections for the M_3 - $m_{\tilde{q}}$ scans only depend on M_3 and $m_{\tilde{q}}$, the same PDF errors per
 2105 point are used for the \tilde{B} -like and \tilde{W} -like grids.

2106 **Appendix A**

2107 **Monte Carlo Samples**

2108 A number of MC samples are utilized in this analysis and referred to throughout the
2109 text. Below is a list of the MC samples used and an explanation of what the sample
2110 names mean.

2111 **A.0.1 List of Samples**

2112 1. Drell-Yan:

2113 `/DYJetsToLL_TuneZ2_M-50_7TeV-madgraph-tauola/`
2114 `Fall11-PU_S6_START42_V14B-v1/AODSIM`

2115 2. QCD enriched with B and D meson decays to electrons:

2116 `/QCD_Pt-20to30_BCToE_TuneZ2_7TeV-pythia6/`
2117 `Fall11-PU_S6_START42_V14B-v1/AODSIM,`
2118 `/QCD_Pt-30to80_BCToE_TuneZ2_7TeV-pythia6/`
2119 `Fall11-PU_S6_START42_V14B-v1/AODSIM,`
2120 `/QCD_Pt-80to170_BCToE_TuneZ2_7TeV-pythia6/`
2121 `Fall11-PU_S6_START42_V14B-v1/AODSIM`

2122 3. Photon + jet doubly enriched with jets passing an EM filter:

2123 /GJet_Pt-20_doubleEMEnriched_TuneZ2_7TeV-pythia6/
 2124 Fall11-PU_S6_START42_V14B-v1/AODSIM

2125 4. W leptonic decays:

2126 /WJetsToLNu_TuneZ2_7TeV-madgraph-tauola/
 2127 Fall11-PU_S6_START42_V14B-v1/AODSIM

2128 5. $t\bar{t}$:

2129 /TTJets_TuneZ2_7TeV-madgraph-tauola/
 2130 Fall11-PU_S6_START42_V14B-v2/AODSIM

2131 A.0.2 Explanation of Naming Conventions

2132 • L: charged lepton

2133 • B: B hadron

2134 • C: D , or charmed, hadron

2135 • E: electron or positron

2136 • G: photon

2137 • W: W boson

2138 • Nu: neutrino

2139 • T: top quark

2140 • TuneZ2: Pythia tune incorporating 2010 LHC data with CTEQ6L1 [108] PDFs
 2141 [115]

2142 • M-50: Generated l^+l^- invariant mass threshold of 50 GeV

2143 • 7TeV: Generated center-of-mass energy 7 TeV

- 2144 ● **pythia6**: Parton showering and hadronization simulated with Pythia v6.424
- 2145 [116]
- 2146 ● **madgraph**: Hard interaction generated with MadGraph [117]
- 2147 ● **tauola**: τ decays generated with Tauola [118]
- 2148 ● **PU_S6**: Generated with S6 pileup scenario
- 2149 ● **START42_V14B**: Reconstructed with best alignment and calibration constants
- 2150 and magnetic field conditions as of August 3, 2011
- 2151 ● **Pt_XtoY**: $X \leq$ generated $\hat{p}_T < Y$
- 2152 ● **BCToE**: Enriched in B and D meson decays to electrons
- 2153 ● **doubleEMEnriched**: Enriched in electromagnetic jets

2154

Bibliography

- 2155 [1] S.L. Glashow, J. Iliopoulos, and L. Maiani, *Phys. Rev. D* **2** (1970) 1285; S.L.
2156 Glashow, *Nucl. Phys.* **22(4)** (1961) 579; J. Goldstone, A. Salam, and S. Weinberg,
2157 *Phys. Rev.* **127** (1962) 965; S. Weinberg, *Phys. Rev. Lett.* **19** (1967) 1264; A.
2158 Salam and J.C. Ward, *Phys. Lett.* **13(2)** (1964) 168.
- 2159 [2] M. Gell-Mann, *Phys. Lett.* **8** (1964) 214; G. Zweig, *CERN 8419/TH. 412* (1964)
2160 (unpublished).
- 2161 [3] J. Drees, *Int. J. Mod. Phys.* **A17** (2002) 3259.
- 2162 [4] P.W. Higgs, *Phys. Lett.* **12(2)** (1964) 132; P.W. Higgs, *Phys. Rev. Lett.* **13** (1964)
2163 508; P.W. Higgs, *Phys. Rev.* **145** (1966) 1156.
- 2164 [5] I. Aitchison, *Supersymmetry in Particle Physics: An Elementary Introduction*
2165 (Cambridge University Press, Cambridge 2007), p. 4.
- 2166 [6] S. P. Martin, *A Supersymmetry Primer* **v4** (2006) 86. [arXiv:hep-ph/9709356](https://arxiv.org/abs/hep-ph/9709356).
- 2167 [7] M. Dine and W. Fischler, *Phys. Lett.* **B110** (1982) 227; C.R. Nappi and B.A.
2168 Ovrut, *Phys. Lett.* **B113** (1982) 175; L. Alvarez-Gaumé, M. Claudson, and M.B.
2169 Wise, *Nucl. Phys.* **B207** (1982) 96; M. Dine and A.E. Nelson, *Phys. Rev.* **D48**
2170 (1993) 1277; M. Dine, A.E. Nelson, and Y. Shirman, *Phys. Rev.* **D51** (1995)
2171 1362; M. Dine, A.E. Nelson, Y. Nir, and Y. Shirman, *Phys. Rev.* **D53** (1996)
2172 2658.

- 2173 [8] A.H. Chamseddine, R. Arnowitt, and P. Nath, *Phys. Rev. Lett.* **49** (1982) 970; R.
 2174 Barbieri, S. Ferrara, and C.A. Savoy, *Phys. Lett.* **B119** (1982) 343; L.E. Ibáñez,
 2175 *Phys. Lett.* **B118** (1982) 73; L.J. Hall, J.D. Lykken, and S. Weinberg, *Phys. Rev.*
 2176 **D27** (1983) 2359; N. Ohta, *Prog. Theor. Phys.* **70** (1983) 542; J. Ellis, D.V.
 2177 Nanopoulos, and K. Tamvakis, *Phys. Lett.* **B121** (1983) 123; L. Alvarez-Gaumé,
 2178 J. Polchinski, and M. Wise, *Nucl. Phys.* **B221** (1983) 495.
- 2179 [9] P. Meade, N. Seiberg, and D. Shih, *Progr. Theor. Phys. Suppl.* **177** (2009) 143.
- 2180 [10] G. Aad et al., *CERN-PH-EP-2011-160* (2011).
- 2181 [11] T. Aaltonen et al., *Phys. Rev. Lett.* **104** (2010) 011801.
- 2182 [12] CMS Collaboration, *CMS-PAS-SUS-11-009* (2011).
- 2183 [13] <http://en.wikipedia.org/wiki/Tevatron>.
- 2184 [14] E. Fernandez et al., *Phys. Rev. Lett.* **54** (1985) 1118; E. Fernandez et al., *Phys.*
 2185 *Rev.* **D35** (1987) 374; D. Decamp et al., *Phys. Lett.* **B237(2)** (1990) 291; F.
 2186 Abe et al., *Phys. Rev. Lett.* **75** (1995) 613; S. Abachi et al., *Phys. Rev. Lett.* **75**
 2187 (1995) 618; G. Alexander et al., *Phys. Lett.* **B377(4)** (1996) 273; S. Aid et al.,
 2188 *Z. Phys.* **C71(2)** (1996) 211; S. Aid et al., *Phys. Lett.* **B380(3-4)** (1996) 461; B.
 2189 Aubert et al., *Phys. Rev. Lett.* **95** (2005) 041802.
- 2190 [15] O. Buchmueller et al., *CERN-PH-TH/2011-220* (2011).
- 2191 [16] <https://twiki.cern.ch/twiki/bin/view/CMSPublic/PhysicsResultsSUS>.
- 2192 [17] G. Aad et al., *JINST* **3** (2008) S08003.
- 2193 [18] B.C. Allanach et al., *Eur. Phys. J.* **C25** (2002) 113.
- 2194 [19] CMS Collaboration, *CMS-PAS-SUS-12-001* (2012).

- 2195 [20] A. Boyarsky, J. Lesgourges, O. Ruchayskiy, and M. Viel, *CERN-PH-TH/2008-*
 2196 *234* (2009).
- 2197 [21] E. Komatsu et al., *Astrophys. J. Suppl. Ser.* **180** (2009) 330.
- 2198 [22] C.-H. Chen and J.F. Gunion, *Physical Review* **D58** (1998) 075005.
- 2199 [23] F. Staub, W. Porod, J. Niemeyer, *JHEP* **1001** (2010) 058.
- 2200 [24] L. Evans and P. Bryant (eds.), *JINST* **3** (2008) S08001.
- 2201 [25] <http://cms.web.cern.ch/news/summary-2011-p-p-running> (2011).
- 2202 [26] <http://public.web.cern.ch/public/en/lhc/Facts-en.html> (2008).
- 2203 [27] CERN, <http://cdsweb.cern.ch/record/833187> (2005).
- 2204 [28] RGBStock.com, <http://www.rgbstock.com/photo/n7EsabW/Airplane> (2011).
- 2205 [29] R. Flükiger, S. Y. Hariharan, R. Küntzler, H. L. Luo, F. Weiss, T. Wolf, and J.
 2206 Q. Xu, in *Landolt-Börnstein: Numerical Data and Functional Relationships in*
 2207 *Science and Technology*, edited by R. Flükiger and W. Klose (Springer, 2012).
- 2208 [30] Y.-P. Sun, F. Zimmermann, and R. Tomás, in Proceedings of the 23rd Particle Ac-
 2209 celerator Conference, Vancouver, 2009, <http://accnet.web.cern.ch/accnet/>
 2210 Literature/2009/TH5PFP016-Sunpdf.pdf (unpublished).
- 2211 [31] O.S. Brüning et al. (eds.), *CERN-2004-003-V-1*, <http://lhcb.web.cern.ch/lhc/LHC-DesignReport.html> (2004).
- 2212 [32] CERN, <http://cdsweb.cern.ch/record/841568/files/> (1993).
- 2213 [33] P. Komorowski and D. Tommasini, in *Proceedings of the 1998 International*
 2214 *Computational Accelerator Physics Conference, Monterey, 1998*, edited by K.
 2215 Ko and R. Ryne (SLAC, Stanford, 1998), p. 192, http://www.slac.stanford.edu/econf/C980914/papers/ICAP98_eConf.pdf.
- 2216
- 2217

- 2218 [34] <http://lhcb-machine-outreach.web.cern.ch/lhc-machine-outreach/components/magnets.htm> (2008).
- 2219 [35] S. Chatrchyan et al. (CMS Collaboration), *JINST* **3** (2008) S08004.
- 2220 [36] G.L. Bayatian et al. (CMS Collaboration), *CERN/LHCC 2006-001*, edited by
2221 D. Acosta (2006).
- 2222 [37] M. Ivova, talk given at the Swiss Ph.D. School on Particle and Astroparticle
2223 Physics (CHIPP), Monte Verita' (2010).
- 2224 [38] G. Bolla et al., *Nucl. Instr. Meth. Res. A* **461** (2001) 182.
- 2225 [39] https://twiki.cern.ch/twiki/pub/CMSPublic/DPGResultsTRK/_imgf9e0ee48ebca770d7774454532b4b4ee.png (2011).
- 2226 [40] https://twiki.cern.ch/twiki/pub/CMSPublic/DPGResultsTRK/_img7569b7652b3f7c15030a11a4223e631c.png (2011).
- 2227 [41] https://twiki.cern.ch/twiki/pub//CMSPublic/DPGResultsTRK/hv11_d1.png (2011).
- 2228 [42] https://twiki.cern.ch/twiki/pub/CMSPublic/DPGResultsTRK/_imga571742cb3a14a9e2581ae95efa54c.gif (2011).
- 2229 [43] <https://twiki.cern.ch/twiki/pub//CMSPublic/DPGResultsTRK/StripHitRes2.gif> (2011).
- 2230 [44] https://twiki.cern.ch/twiki/pub//CMSPublic/EcalDPGResults/histories2_laser.png (2012).
- 2231 [45] https://twiki.cern.ch/twiki/pub//CMSPublic/EcalDPGResults/electronres_eb_inclusive.png (2012).

- 2240 [46] https://twiki.cern.ch/twiki/pub//CMSPublic/EcalDPGResults/electronres_ee_inclusive.png (2012).
- 2241 [47] <https://twiki.cern.ch/twiki/pub//CMSPublic/EcalDPGResults/seed-time.EEEE.png> (2012).
- 2242 [48] N. Akchurin and R. Wigmans, *Rev. Sci. Instrum.* **74** (2003) 2955.
- 2243 [49] CMS Collaboration, *CMS-DP 2010-025* (2010).
- 2244 [50] https://twiki.cern.ch/twiki/pub/CMSPublic/PhysicsResultsMU0/dimuMass_2011Run_1fb_20July2011.pdf (2011).
- 2245 [51] S. Chatrchyan et al. (CMS Collaboration), *JHEP* **4** (2012) 33.
- 2246 [52] W.H. Smith, P. Chumney, S. Dasu, F. Di Lodovico, M. Jaworski, J.R. Lackey, and P. Robl in *Proceedings of the 7th Workshop on Electronics for LHC Experiments, Stockholm, 2001*, edited by C. Isabella (CERN, Geneva, 2001), p. 238.
- 2247 [53] R. Brun and F. Rademakers, *Nucl. Inst. Meth. Res.* **A389** (1997) 81. See also <http://root.cern.ch/>.
- 2248 [54] J. Guteleber and L. Orsini, *Cluster Comput.* **5** (2002) 55.
- 2249 [55] D. Box, D. Ehnebuske, G. Kakivaya, A. Layman, N. Mendelsohn, H.F. Nielsen, S. Thatte, and D. Winer, *W3C Note 08*, <http://www.w3.org/TR/2000/NOTE-SOAP-20000508/> (2000).
- 2250 [56] R. Arcidiacono et al., talk given at the 10th ICAL-EPCS International Conference on Accelerator and Large Experiment Physics Control Systems, Geneva (2005).
- 2251 [57] J. Knobloch et al., *CERN-LHCC-2005-024* (2005).
- 2252 [58] R. Brunelière, *Nucl. Inst. Meth. Res.* **A572** (2007) 33.

- 2262 [59] S. Chatrchyan et al. (CMS Collaboration), *JINST* **5** (2010) T03011.
- 2263 [60] CMS Collaboration, *CMS PAS EGM-10-002* (2010).
- 2264 [61] P. Meridiani and C. Seez, *CMS IN-2011/002* (2011).
- 2265 [62] P. Adzic et al. (CMS Electromagnetic Calorimeter Group), *Eur. Phys. J.* **C44S2**
2266 (2006) 1.
- 2267 [63] P. Adzic et al. (CMS Electromagnetic Calorimeter Group), *JINST* **3** (2008)
2268 P10007.
- 2269 [64] M. Malberti, *Nuc. Sci. Symposium Conference Record NSS/MIC IEEE* (2009)
2270 2264.
- 2271 [65] S. Chatrchyan et al. (CMS Collaboration), *JINST* **5** (2010) T03010.
- 2272 [66] R. Paramatti, *J. Phys. Conf. Ser.* **293** (2011) 012045.
- 2273 [67] Y. Yang, [http://www.hep.caltech.edu/cms/posters/Pi0Poster_](http://www.hep.caltech.edu/cms/posters/Pi0Poster_CMSWeekDec2011.pdf)
2274 CMSWeekDec2011.pdf (2011).
- 2275 [68] M. Anderson, A. Askew, A.F. Barfuss, D. Evans, F. Ferri, K. Kaadze, Y. Maravin,
2276 P. Meridiani, and C. Seez, *CMS IN-2010/008* (2010).
- 2277 [69] <https://twiki.cern.ch/twiki/bin/view/CMS/ECALEnergyScaleCorrections>.
- 2278 [70] The H $\rightarrow\gamma\gamma$ working group, *CMS AN-2011/426* (2011).
- 2279 [71] M. Cacciari, *LPTHE-P06-04* (2006).
- 2280 [72] M. Cacciari, G.P. Salam, and G. Soyez, *CERN-PH-TH-2011-297* (2011).
- 2281 [73] S. Chatrchyan et al. (CMS Collaboration), *Phys. Rev. Lett.* **106** (2011) 082001.

- 2282 [74] A. Askew, B. Cox, D. Elvira, Y. Gershtein, M. Hildreth, D. Jang, Y.-F. Liu, D.
 2283 Mason, D. Morse, U. Nauenberg, M. Paulini, R. Stringer, R. Yohay, and S.L.
 2284 Zang, *CMS AN-2011/515* (2011).
- 2285 [75] F. Beaudette, D. Benedetti, P. Janot, and M. Pioppi, *CMS AN-2010/034* (2010).
- 2286 [76] M. Konecki, in Proceedings of the European Physical Society Europhysics Con-
 2287 ference on High Energy Physics, Krakow, 2009, Eur. Phys.Soc. Mulhouse (ed.)
 2288 (unpublished).
- 2289 [77] W. Adam, R. Fr  wirth, A. Strandlie, and T. Todorov, *J. Phys.* **G31** No. 9 (2005).
- 2290 [78] CMS Collaboration, *CMS PAS PFT-09-001* (2009).
- 2291 [79] CMS Collaboration, *CMS PAS PFT-10-002* (2010).
- 2292 [80] S. Chatrchyan et al., *JINST* **6** (2011) P11002.
- 2293 [81] CMS Collaboration, *CERN-PH-EP* **2011-102** (2011).
- 2294 [82] M. Cacciari, G.P. Salam, and G. Soyez, *JHEP* **0804** (2008) 063.
- 2295 [83] G. Salam, talk given at CERN Theory Institute: SM and BSM Physics at the
 2296 LHC (2009).
- 2297 [84] C.W. Fabjan and R. Wigmans, *Rep. Prog. Phys.* **52** (1989) 1519.
- 2298 [85] <http://www-cdf.fnal.gov/physics/new/top/2004/jets/cdfpublic.html>
 2299 (visited on 16 January 2011).
- 2300 [86] S. Chatrchyan et al. (CMS Collaboration), *JINST* **6** (2011) P09001.
- 2301 [87] CMS Collaboration, *CMS PAS JME-09-002* (2009).
- 2302 [88] T. Sj  strand, S. Mrenna, and P. Z. Skands, *Comput. Phys. Commun.* **178** (2008)
 2303 852.

- 2304 [89] S. Chatrchyan et al. (CMS Collaboration), *JINST* **5** (2010) T03014.
- 2305 [90] J. P. Chou, S. Eno, S. Kunori, S. Sharma, and J. Wang, *CMS IN-2010/006*
2306 (2010).
- 2307 [91] Y. Chen, talk given at a meeting of the CMS JetMET group (2011).
- 2308 [92] R. Korzekwa et al., *iEEE Trans. Elec. Dev.* **38** (1991) 745.
- 2309 [93] W. Adam, Th. Speer, B. Mangano, and T.Todorov, *CMS NOTE* **2006/041**
2310 (2006).
- 2311 [94] G. Daskalakis, D. Evans, C.S. Hill, J. Jackson, P. Vanlaer, J. Berryhill, J. Haupt,
2312 D. Futyan, C. Seez, C. Timlin, and D. Wardrope, *CMS AN-2007/019* (2007).
- 2313 [95] F. James and M. Roos, *Comput. Phys. Commun.* **10** (1975) 343.
- 2314 [96] W. Verkerke and D.P. Kirkby, *CHEP-2003-MOLT007* (2003).
- 2315 [97] J.E. Gaiser, Ph.D. thesis, Stanford University (1982).
- 2316 [98] A. Askew, S. Arora, Y. Gershtein, S. Thomas, G. Hanson, R. Stringer, W. Flana-
2317 gan, B. Heyburn, U. Nauenberg, S.L. Zang, R. Nandi, D. Elvira, D. Mason, M.
2318 Balazs, B. Cox, B. Francis, A. Ledovskoy, and R. Yohay, *CMS AN* **2010/271**
2319 (2010).
- 2320 [99] Information about all CMS datasets is available from the CMS Data Aggregation
2321 System (DAS), located at the URL <https://cmsweb.cern.ch/das/>.
- 2322 [100] S. Chatrchyan et al., *Phys. Rev. Lett.* **106** (2011) 211802.
- 2323 [101] G. Aad et al. (ATLAS Collaboration), S. Chatrchyan et al. (CMS Collabora-
2324 tion), and LHC Higgs Combination Group, *CMS-NOTE-2011/005* (2011).

- 2325 [102] A.L. Read, in *Proceedings of the First Workshop on Confidence Limits, Geneva,*
 2326 2000, edited by L. Lyons, Y. Perrin, and F.E. James (CERN, Geneva, 2000), p.
 2327 81.
- 2328 [103] G. Cowan, K. Cranmer, E. Gross, and O. Vitells, *Eur. Phys. J.* **C71** (2011)
 2329 1554.
- 2330 [104] J. Neyman and E.S. Pearson, *Phil. Trans. R. Soc. Lond.* **A231** (1933) 289.
- 2331 [105] CMS Collaboration, *CMS PAS EWK-11-001* (2011).
- 2332 [106] S. Alekhin et al. (The PDF4LHC Working Group), [arXiv:1101.0536\[hep-ph\]](https://arxiv.org/abs/1101.0536);
 2333 M. Botje et al. (The PDF4LHC Working Group), [arXiv:1101.0538\[hep-ph\]](https://arxiv.org/abs/1101.0538);
 2334 <http://www.hep.ucl.ac.uk/pdf4lhc/index.html>.
- 2335 [107] A.D. Martin, W.J. Stirling, R.S. Thorne, and G. Watt, *Eur. Phys. J.* **C63**
 2336 (2009) 189.
- 2337 [108] P. M. Nadolsky, H.-L. Lai, Q.-H. Cao, J. Huston, J. Pumplin, D. Stump, W.-K.
 2338 Tung, and C.-P. Yuan, *Phys. Rev.* **D78** (2008) 013004.
- 2339 [109] R.D. Ball, L. Del Debbio, S. Forte, A. Guffanti, J.I. Latorre, J. Rojo, and M.
 2340 Ubiali, *Nucl. Phys.* **B838** (2010) 136.
- 2341 [110] J.M. Campbell, J.W. Huston, and W.J. Stirling, *Rep. Prog. Phys.* **70** (2007) 89.
- 2342 [111] A. Djouadi, J.-L. Kneur, G. Moultaka, [arXiv:hep-ph/0211331](https://arxiv.org/abs/hep-ph/0211331) (2005).
- 2343 [112] M. Muhlleitner, A. Djouadi, Y. Mambrini, *Comput. Phys. Commun.* **168** (2005)
 2344 46.
- 2345 [113] J. Allison et al., *IEEE Trans. Nucl. Sci.* **53(1)** (2006) 270.
- 2346 [114] W. Beenakker, R. Hoepker, M. Spira, [arXiv:hep-ph/9611232](https://arxiv.org/abs/hep-ph/9611232) (1996).

²³⁴⁷ [115] R. Field, talk given at LHC Physics Centre at CERN Minimum Bias and Underlying Event Working Group Meeting (2011).

²³⁴⁹ [116] T. Sjöstrand, S. Mrenna, and P. Z. Skands, *JHEP* **0605** (2006) 026.

²³⁵⁰ [117] dummy

²³⁵¹ [118] dummy